

**Development of a Layerless Additive Manufacturing  
Stereolithography Machine to Improve Surface Quality and  
Dimensional Accuracy**

by

Ian Wood

A Thesis Submitted in Partial Fulfillment  
of the Requirements for the Degree of

Master of Applied Science

in

The Faculty of Engineering and Applied Science

Mechanical Engineering

University of Ontario Institute of Technology

June, 2016

© Ian Wood, 2016

## **Abstract**

Stereolithography (SLA) is an Additive Manufacturing (AM) process that has recently gained significant popularity in manufacturing research. The material used in SLA is a photocurable resin. SLA fabrication has conventionally been executed in a layered build process, which results in the staircase effect: a common problem in layered manufacturing giving a lower quality part surface due to created cusps on the surface. Manufacturing the part using a continuous build should theoretically eliminate this issue. A methodology for the design, development and calibration of a new layerless additive manufacturing system is introduced in this thesis. The methodology involves synchronizing the display of cross-sectional images with the platform elevation on an SLA machine and finding the optimal parameters in order to obtain a more dimensionally accurate and higher surface quality part. A variety of geometric features are constructed through experiments and their properties are examined to extract the most adequate fabrication parameters. The layerless process was found to reduce the staircase effect and the surface roughness on fabricated parts, as well as improve the ability of the machine to build complex features.

**Keywords:** Stereolithography, Additive Manufacturing, Surface Quality, Dimensional Accuracy

## **Dedication**

I would like to dedicate this thesis to my parents Paul and Christine Wood, whose virtues I attempt to exemplify every day of my life. Without their support and encouragement, I wouldn't be who or where I am today.

## **Acknowledgements**

A sincere thanks goes out to my supervisor, Dr. Ahmad Barari, for his guidance, understanding and support during my graduate studies and research. Thanks to Cody Berry for his assistance with the setup and maintenance of the electronics, to Amir Lalehpour for his time taken to measure some of the results and to the senior capstone team for assisting me with the machine's design and development at the beginning of my research.

Special thanks to the evaluation committee Dr. Hossam Kishawy and Dr. Martin Agelin-Chaab for taking their valuable time to review my thesis and for providing their input.

Finally I would like to thank my hard-working parents who inspire, motivate and encourage me to improve myself each and every day of my life.

# Table of Contents

Abstract.....	I
Dedication.....	II
Acknowledgements.....	III
Table of Contents.....	IV
List of Figures.....	VII
List of Tables.....	X
Nomenclature.....	XI
List of Parameters.....	XII
<b>1 Introduction.....</b>	<b>1</b>
<b>2 Literature Review.....</b>	<b>4</b>
2.1 INTRODUCTION.....	4
2.2 LITERATURE ON THE SURFACE QUALITY OF AM PARTS.....	5
2.3 LITERATURE ON MECHANICAL PROPERTIES OF COMMON AM APPLICATIONS.....	13
2.4 LITERATURE ON BIOMATERIAL AM APPLICATIONS.....	25
2.5 LITERATURE ON STEREO LITHOGRAPHY AM APPLICATIONS.....	32
<b>3 Methodology.....</b>	<b>43</b>
3.1 INTRODUCTION.....	43

3.2	CURING MECHANISM.....	44
3.3	MACHINE DESIGN .....	47
3.4	MACHINE CALIBRATION .....	51
3.4.1	Controlling Software.....	52
3.4.2	Manual Calibration .....	56
3.4.3	Expansion of Enclosed and External Dimensions .....	57
3.4.4	Optimal Exposure Parameter Selection .....	61
3.4.5	Complex 3D Parts (Rook and Anglecube).....	65
3.5	LAYERLESS FABRICATION PROCESS.....	68
3.5.1	STL Video Generation.....	69
3.5.2	Determination of Minimum Machine Feed Rate .....	73
3.5.3	Determination of Optimal Machine Feed Rate.....	73
3.5.4	Determination of Adjusted Video Frame Rate .....	74
3.5.5	Synchronizing of Video and Curing Processes.....	75
<b>4</b>	<b>Implementation .....</b>	<b>76</b>
4.1	INTRODUCTION .....	76
4.2	IMPLEMENTATION OF THE STL READER AND SLICER .....	77
4.3	IMPLEMENTATION OF MACHINE SYNCHRONIZATION .....	78
<b>5</b>	<b>Implementation Case Studies and Discussion .....</b>	<b>79</b>
5.1	INTRODUCTION .....	79
5.2	MANUFACTURED ROOK.....	80

5.3	MANUFACTURED SLANTEDCUBE .....	83
5.3.1	Layer-Manufactured Angled Surfaces .....	88
5.3.2	Layerless-Manufactured Angled Surfaces .....	94
5.3.3	Comparison of SLA Layered and Layerless Manufactured Angled Surfaces .....	99
<b>6</b>	<b>Conclusions and Future Work</b> .....	<b>102</b>
6.1	CONCLUSIONS .....	102
6.2	FUTURE WORK .....	105
	References.....	106
	Appendices.....	115
	APPENDIX A: PRELIMINARY MACHINE ENGINEERING ASSEMBLY DRAWINGS.....	115
	APPENDIX B: MAKERJUICE G+ RESIN TECHNICAL DATA SHEET .....	117
	APPENDIX C: CODE.....	118

## List of Figures

Figure 2.1: Staircase Effect on AM Produced Parts. ....	6
Figure 2.2: Schematic for Modeling the Surface Profile of the FDM-processed Part.....	8
Figure 2.3: Effect of the Chemical Treatment on the Surface Roughness.....	9
Figure 2.4: Estimation of the 3D Surface Roughness Using 90% of Initial Points. ....	10
Figure 2.5: Adaptive Slicing Technique Impact on the Staircase Effect. ....	11
Figure 2.6: Cusp Side View of a 65-degree Slope on a RP Part.....	12
Figure 2.7: Schematic of the Surface Roughness Measurement Using a Piece-wise Polynomial	13
Figure 2.8: Stress-Strain Curves of Normal Sintering and Pressure-Assisted Sintering. ....	16
Figure 2.9: Effect of Layer Thickness on Average Pore Width and Proportion of Pores. ....	29
Figure 2.10: Dynamic Viscosity vs Exposure Time for 3 Different Light Intensities (from left to right: 70, 37, 20 (mW/cm <sup>2</sup> )). ....	32
Figure 2.11: Dynamic Viscosity vs. Exposure Energy for Several Sample Thicknesses.....	33
Figure 2.12: Rate of Polymerization and Temperature as a Function of UV Curing Time.....	35
Figure 2.13: Rate of Polymerization as a Function of Irradiation Time for Several Structures of Diepoxyalkane Monomers. ....	36
Figure 2.14: Cure Depth as a function of Energy Dosage and Photoinitiator Concentration.....	37
Figure 2.15: Normalized Photoinitiator Concentration vs Layer Thickness of the Resin at 17s (left) and 24 s (right) Exposure Time. ....	39
Figure 2.16: Curing Time vs. Temperature for 5% Resin Concentration and a 200 Micrometer Layer Thickness. ....	42
Figure 3.1: Chemical Structure of 3 Types of Monomers Used in Commercial Resins. ....	44
Figure 3.2: Curing Schematic. ....	45

Figure 3.3: Schematic of SLA Machine Design. ....	47
Figure 3.4: Full-scale View of SLA Machine.....	48
Figure 3.5: G+ Absorbance Ratio as a Function of Exposed Light Wavelength.....	49
Figure 3.6: Software View of Mask.....	54
Figure 3.7: Ring Experiments (Internal and External Variation). ....	58
Figure 3.8: External Ring Dimensional Error vs. Nominal Size. ....	60
Figure 3.9: Internal Ring Dimensional Error vs. Nominal Size. ....	61
Figure 3.10: Comprehensive Part. ....	63
Figure 3.11: Comprehensive Part Experimental Samples. ....	63
Figure 3.12: Comprehensive Sample, Scaled 3:1. ....	65
Figure 3.13: (a) Rook STL file, and (b) Rook SLA print. ....	66
Figure 3.14: Rook Build Attempts with Feed Rates: (a) Too High, and (b) Too Low.....	67
Figure 3.15: AngleCube: (a) STL file, and (b) SLA print. ....	68
Figure 3.16: STL Representation of AngleCube CAD file.....	72
Figure 5.1: Initial Attempt for Rook Layerless Fabrication: (a) View 1, and (b) View 2. ....	81
Figure 5.2: Profile View of Three Different-Sized Rook Parts Using Layered Manufacturing... ..	82
Figure 5.3: Top View of Three Different-Sized Rook Parts Using Layered Manufacturing. ....	83
Figure 5.4: SlantedCube STL File. ....	83
Figure 5.5: (a) SlantedCube Layerless Part, and (b) Part Edge without the Staircase Effect. ....	84
Figure 5.6: SLA 3D Roughness Shape of Layered Angled Surface ( $S_a = 0.653 \mu\text{m}$ ).....	86
Figure 5.7: SLA 3D Roughness Shape of Layerless Angled Surface ( $S_a = 0.126 \mu\text{m}$ ). ....	87

Figure 5.8: CAD models of SlantedCubes with surfaces angled at: (a) 5 degrees (b) 10 degrees (c) 15 degrees (d) 20 degrees (e) 25 degrees (f) 30 degrees (g) 35 degrees (h) 40 degrees and (i) 45 degrees. ....	89
Figure 5.9: SLA Roughness of Layered 5-Degree Surface ( $S_a = 0.854 \mu\text{m}$ ). ....	90
Figure 5.10: SLA Roughness of Layered 10-Degree Surface ( $S_a = 0.876 \mu\text{m}$ ). ....	90
Figure 5.11: SLA Roughness of Layered 15-Degree Surface ( $S_a = 0.669 \mu\text{m}$ ). ....	91
Figure 5.12: SLA Roughness of Layered 20-Degree Surface ( $S_a = 0.752 \mu\text{m}$ ). ....	91
Figure 5.13: SLA Roughness of Layered 25-Degree Surface ( $S_a = 0.601 \mu\text{m}$ ). ....	92
Figure 5.14: SLA Roughness of Layered 30-Degree Surface ( $S_a = 0.702 \mu\text{m}$ ). ....	92
Figure 5.15: SLA Roughness of Layered 35-Degree Surface ( $S_a = 0.752 \mu\text{m}$ ). ....	93
Figure 5.16: SLA Roughness of Layered 40-Degree Surface ( $S_a = 0.595 \mu\text{m}$ ). ....	93
Figure 5.17: SLA Roughness of Layered 45-Degree Surface ( $S_a = 0.454 \mu\text{m}$ ). ....	94
Figure 5.18: SLA Roughness of Layerless 5-Degree Surface ( $S_a = 0.0934 \mu\text{m}$ ). ....	95
Figure 5.19: SLA Roughness of Layerless 10-Degree Surface ( $S_a = 0.0714 \mu\text{m}$ ). ....	95
Figure 5.20: SLA Roughness of Layerless 15-Degree Surface ( $S_a = 0.187 \mu\text{m}$ ). ....	96
Figure 5.21: SLA Roughness of Layerless 20-Degree Surface ( $S_a = 0.129 \mu\text{m}$ ). ....	96
Figure 5.22: SLA Roughness of Layerless 25-Degree Surface ( $S_a = 0.179 \mu\text{m}$ ). ....	97
Figure 5.23: SLA Roughness of Layerless 30-Degree Surface ( $S_a = 0.117 \mu\text{m}$ ). ....	97
Figure 5.24: SLA Roughness of Layerless 35-Degree Surface ( $S_a = 0.107 \mu\text{m}$ ). ....	98
Figure 5.25: SLA Roughness of Layerless 40-Degree Surface ( $S_a = 0.137 \mu\text{m}$ ). ....	98
Figure 5.26: SLA Roughness of Layerless 45-Degree Surface ( $S_a = 0.114 \mu\text{m}$ ). ....	99
Figure 5.27: Roughness of Angled Surfaces for Layered and Layerless Processes. ....	100

## List of Tables

Table 2.1: Material Property Comparison of Conventional Steel and ProMetal.....	15
Table 2.2: Material Properties of Recycled Glass. ....	18
Table 2.3: Mechanical Properties of HDPE.....	20
Table 2.4: Material Properties of PMMA (Poly Methyl Methacrylate). ....	21
Table 2.5: Material Properties of Alumina-based Powder.....	22
Table 2.6: Material Properties for PCL and PLA Hybrids. ....	23
Table 2.7: Mechanical Properties of ABS and PLA. ....	24
Table 2.8: Conversion and Molecular Weight of PMMA Obtained by UV Curing. ....	40
Table 3.1: External Ring Experiment Measurements. ....	59
Table 3.2: Internal Ring Experiment Measurements. ....	59
Table 3.3: Measurements of Comprehensive Samples. ....	64
Table 5.1: Comparison of Layered and Layerless Angled Surface Roughness.....	100

## **Nomenclature**

RP = Rapid Prototyping

3DP = Three-Dimensional Printing

AM = Additive Manufacturing

MP = Mask Projection

DLP = Digital Light Processing

SLA = Stereolithography Apparatus (3DP process)

STL = Geometric Data Exchange Format for Additive Manufacturing Systems

LCD = Liquid Crystal Display

LED = Light-Emitting Diode

PCB = Printed Circuit Board

UV = Ultraviolet

FDM = Fused Deposition Modeling

SLS = Selective Laser Sintering

BP = Bioprinting

SGM = Spiral Growth Manufacturing

PLLA/PLA = Poly-Lactic Acid

ABS = Acrylonitrile Butadiene Styrene

HDPE = High-Density Polyethylene

HA = Hydroxyapatite

CMM = Coordinate-Measuring Machine

CAD = Computer-Aided Design

## List of Parameters

$f_{min}$  = minimum feed rate the machine can allow due to the motors

$f_{opt}$  = optimum feed rate to set based on experimental exposure parameters

$h_{lift}$  = distance the machine moves up during the lift sequence

$h_L$  = layer thickness of the part

$t_{exp}$  = exposure time of the light to the resin

$t_{print}$  = total time required to build the part using the machine

$t_{video}$  = total time required to run the video from the STL reader code

$v_{Fcurr}$  = video frame rate from the current code

$v_{Fadj}$  = video frame rate desired to synchronize with the machine

$n_F$  = number of frames required in the video

$n_i n_j n_k$  = normal vector directions of triangles in an STL file

$vm_x vm_y vm_z$  = coordinates of triangle vertices in an STL file ( $m = 1,2,3$ )

$S_a$  = 3D arithmetic mean height of a surface

$SR_{LL}$  = experimental surface roughness obtained from the layerless part

$SR_O$  = original surface roughness obtained from the conventional layer manufactured part

# 1 Introduction

Additive Manufacturing (AM) is a popular field of research in engineering, in which three-dimensional shapes are constructed by adding material layer by layer (layered manufacturing). It is also commonly known as Three-Dimensional Printing (3DP), which has been an attractive research topic in manufacturing in recent years. There are several applications of 3DP, including but not limited to Fused Deposition Modeling (FDM), Selective Laser Sintering (SLS), Inkjet Printing (IP), Bioprinting (BP), and Stereolithography (SLA) [Gibson et al. 2010]. Demand for improving the surface quality and dimensional accuracy of fabricated three-dimensional parts is consistently increasing. This research pertains to the design and development of a specific SLA AM application, in which near-Ultraviolet (UV) light is used as a radiation source to project images of the cross-sections of a 3D model onto a build plate submerged in photocurable resin [Karsten et al. 2009]. The original setup constructs each layer of an object in sequence and builds parts in a bottom-up process. Layered manufacturing presents a well-known problem in 3DP known as the

staircase effect, which results in lower surface quality and can jeopardize the accuracy of manufactured parts. The motivation behind this research is to develop a solution to avoid the staircase effect resulting from the typical layered manufacturing processes.

Surface quality involves the study of surface roughness and must not be improperly associated with surface integrity as having the same definition. Surface quality can include all of surface finish/roughness, waviness and lay of any fabricated surface, whereas surface integrity is the condition of a workpiece after being used in a manufacturing process. Some of the parameters affecting surface integrity are tool wear, cutting speed, tool material, coatings, cutting angle and contact area.

The challenges to achieve this objective are due to four major limitations in the design and development of the layerless manufacturing process: the material used for part construction, the radiation source used, the graphical device used and the complexity of the part desired, which all affect the capabilities of the machine and are dependent on one another. The material used in this research is MakerJuice Substance G+ photocurable resin, a liquid that hardens when exposed to specific types of light. This hardening is a chemical process also known as curing or photopolymerization. MakerJuice G+ is commercially available and reacts quickly to the light. The radiation source used is several near-UV Light-Emitting Diode (LED) units, rated at 405 nanometres and 3 Watts of power each, since the resin will only cure at wavelengths of 440 nanometres or less. The graphical device used is a monochrome Liquid Crystal Display (LCD) screen, which transfers a fraction of the power of the lights through a displayed shape and penetrates into the resin-filled container onto the build plate. A poor quality screen will transmit much less power, but the monochrome screen transmits five times as much power as multicolor.

The build process will take less time to complete and the quality of the part should be better. The optimal amount of time the light is exposed to the part, the exposure time, needs to be determined.

In order to avoid the drawbacks of layered manufacturing including the stair-case effect, a layerless SLA system is designed and developed. This requires two tasks:

*Slicing Process* - implementing a program to produce information from the cross-sections of a 3D model from a Stereolithography file (STL), and

*Dynamic Curing Process* - synchronizing the transfer of slicing data with the elevation of the machine platform considering the optimum curing parameters.

The input of the slicing process is either a text or binary STL file and the desired output is a video of the desired geometric model, showing its cross-sections for a length specified in the code as a frame rate. The frame rate of the video must then be synchronized with the constant feed rate of the machine by equating the time of the video to the time required for the curing process. The frame rate is computed based on the curing parameters of the machine, which are achieved using experimental studies. The elevator of the system is instructed by the G-code program to control the exact computed curing time required for layerless fabrication.

The structure of the thesis is as follows: After this introduction, Chapter 2 presents a comprehensive literature review of 3DP processes and materials. Chapter 3 explains the methodologies used in this research, which has 4 major Sections: Curing Mechanism, Machine Design, Machine Calibration, and Layerless Fabrication Process. Chapter 4 discusses the implementation process for layerless AM. Chapter 5 presents and discusses each of the results obtained, and Chapter 6 contains the conclusion of the thesis and the research ideas to be investigated in future work.

## **2 Literature Review**

### **2.1 INTRODUCTION**

There have been many studies on AM processes and materials over the past three decades. Each AM process has its own set of specific applications and material usage. Materials used in AM processes cover a range of metals, plastics, glass, ceramics and biomaterials. Also, each material used has its own unique set of mechanical properties once fabricated. Among the typical AM processes, the masked projection Stereolithography application is receiving significant attention in industry. This is particularly because of its build efficiency, speed and independence of the size of the part's cross-section as opposed to other AM processes. The research can be categorized based on the method of construction of the parts and the terminologies are vastly different for each separate application. There are still many topics of research to be investigated for these processes, and the interesting aspect is that there will always be a way to improve them based on rapidly developing technology. Increasing the surface quality of AM parts is one example of quality improvement, which is the first topic of the literature review. The next literature topic

involves the review of mechanical properties of common AM applications, followed by literature on biomaterial AM applications and finally literature on stereolithography AM applications.

## **2.2 LITERATURE ON THE SURFACE QUALITY OF AM PARTS**

In 2003, Pandey, Rheddy and Dhande investigated a semi-empirical study on how to improve the surface finish of parts constructed using a Fused Deposition Modeling (FDM) AM process [Rheddy and Dhande 2003]. The accessibility of certain locations on the prototyped part was addressed using a simple material removal method called Hot Cutter Machining (HCM). A fractional factorial design of experiments was adopted, involving two levels (low and high) with four factors (cutting speed, build orientation, rake angle and angle between cutting edge and layers). ANOVA was used to determine the significance of each variable investigated as well as the confidence level of the statistical model developed for the surface quality of the HCM surface. Results showed that the proposed machining method is able to produce a surface finish of the order of  $0.3 \mu\text{m}$  with 87% confidence. Figure 2.1 shows a depiction of the staircase effect and the important parameters involved with it. The underlying problem with the staircase effect is with constructing layers during the build process. The larger the layer/slice thickness, the more inaccurate the approximation to the nominal profile on the prototyped surface and the greater the surface roughness. The build orientation can substantially affect the roughness as well.

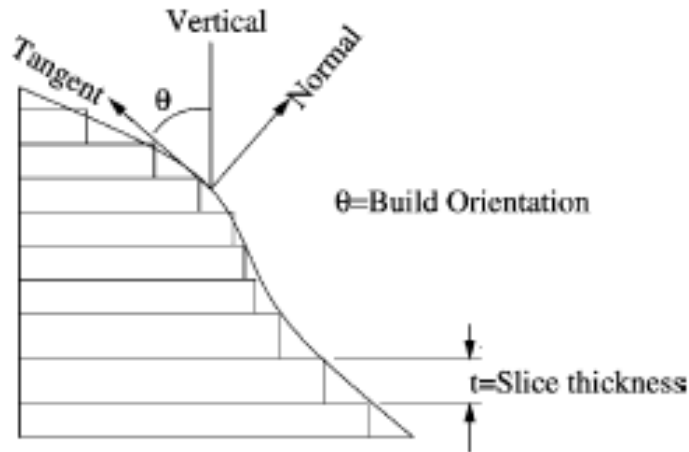


Figure 2.1: Staircase Effect on AM Produced Parts.  
[Rheddy and Dhande 2003]

Also in 2003, Thrimurthulu, Pandey and Reddy investigated the surface finish and part deposition time as a compromise between the two aspects pertaining to part construction in Rapid Prototyping (RP) [Thrimurthulu et al. 2003]. A new solution was proposed for solving the poor surface finish problem called adaptive slicing. In addition to this solution, an optimal part build orientation was proposed to improve on the quality even further. Models used to evaluate the part's average surface roughness and build time were developed and optimized using a real coded genetic algorithm. Results showed that by minimizing the weighted sum of the two objectives, namely build time and average part surface roughness, an optimal part deposition orientation could be selected.

In 2007, Barari, ElMaraghy and Knopf conducted research to reduce the uncertainty of a part's minimum deviation zone estimation [Barari et al. 2007]. An iterative search procedure was used in an integrated inspection system to estimate the minimum deviation zone. The search procedure used Parzen Windows to estimate the probability density function of the geometric

deviations between the substitute and nominal surfaces. The density function was used to narrow down the iterative measurements required until a desired level of convergence is reached. Both actual and virtual inspection data were presented through experiments to reduce the uncertainty in the minimum deviation zone estimation. The method was found to reduce inspection cost as well as the cost for rejecting or accepting parts based on quality. It was observed that as the number of points in the search increases, the function tends towards a normal distribution.

In 2009, Ahn, Kweon, Kwon, Song and Lee did a study on the representation of an additive manufactured part's surface roughness using an FDM process [Ahn et al. 2009]. A new approach to model the surface roughness was presented in this work, using a theoretical model based on actual surface roughness distributions of FDM parts. The model expressed surface roughness distribution according to changes in surface angle by considering the main factors that significantly affect surface quality, namely surface angle, layer thickness, cross-sectional shape of the filament and the overlap interval. The model shaped the surface profile as an elliptical curve rather than a rectangular shape as it has been most commonly interpreted. Figure 2.2 demonstrates the model of the surface profile used in the research, showing the current layer, the layer before and the layer after. The important variables used in relevant equations are shown in this depiction.

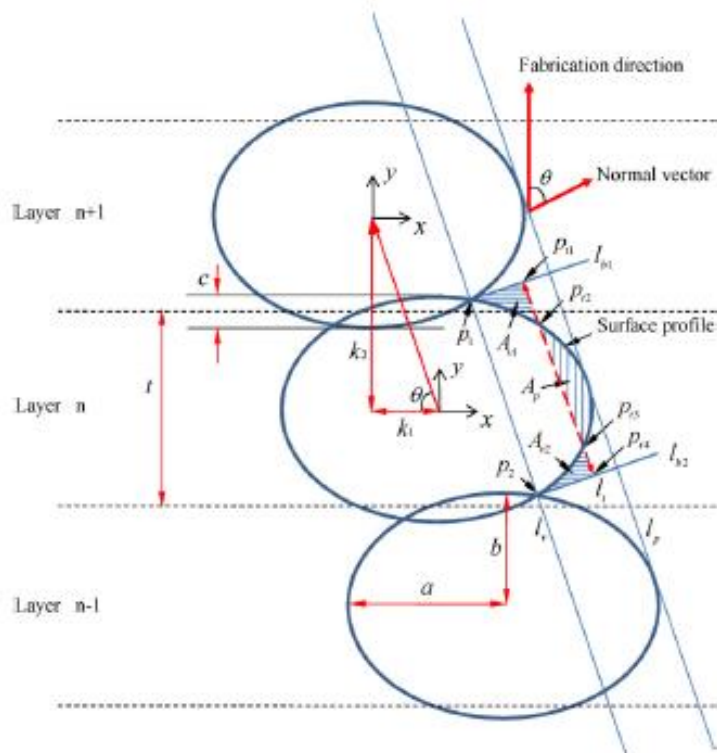


Figure 2.2: Schematic for Modeling the Surface Profile of the FDM-processed Part. [Ahn et al. 2009]

Also in 2009, Galantucci, Lavecchia and Percoco performed an experimental study on enhancing the surface finish of FDM parts by implementing a chemical method [Galantucci et al. 2009]. The experiments were carried out in the first phase by selecting the optimal tip size, raster width and slice height based on past experiments. In the second phase, test specimens were chemically finished using dimethylketone (acetone) after mixing with water in a bath. Results of the experiments showed that the surface roughness of all samples was substantially decreased as can be shown in Figure 2.3. The bright bars in the graph show the surface roughness of each sample before the chemical treatment and the dark bars show the surface roughness of each sample after the chemical treatment.

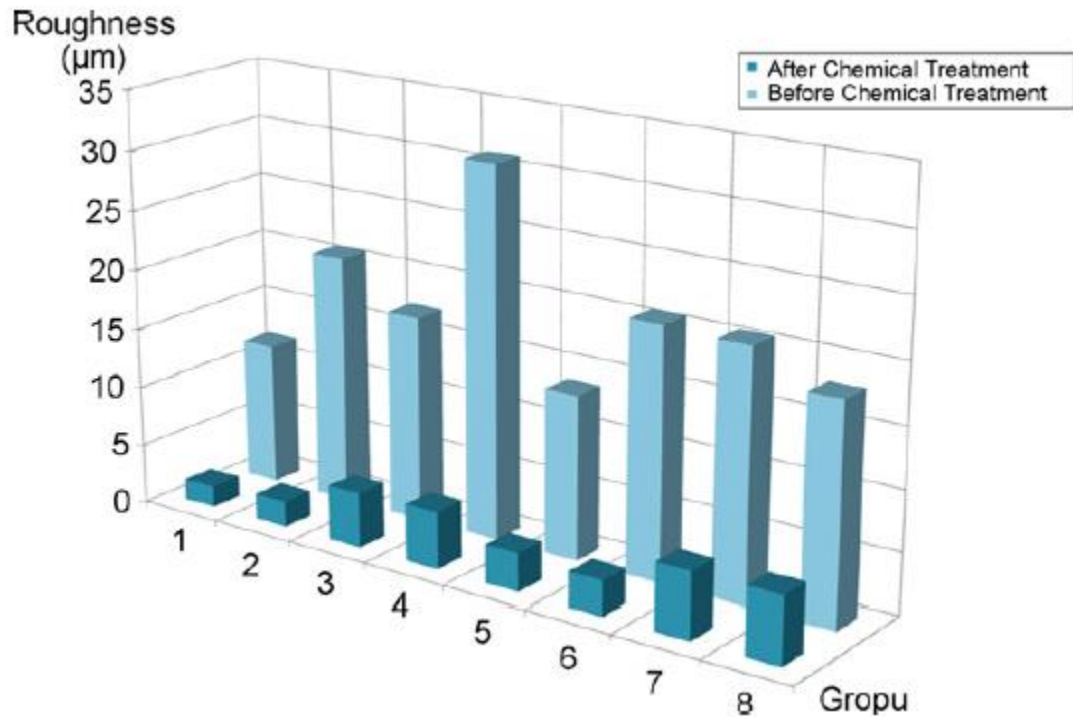


Figure 2.3: Effect of the Chemical Treatment on the Surface Roughness. [Galantucci et al. 2009]

In 2014, Jamiolahmadi and Barari worked on a finite difference approach to analyze the surface topography of AM parts [Jamiolahmadi and Barari 2014]. The goal of the research was to provide a detailed reconstruction of the surface, something which had not been done previously, as the existing work only provided information regarding discrete points measured from the surface. Sample measured data points were taken to achieve this goal. The methodology used was a mapping method using a harmonic function with Dirichlet boundary conditions. The methodology developed could be used for the surface texture modeling, surface quality analysis, surface quality inspection, and in planning for post-processing of the suitable surface finish processes. Figure 2.4 shows the reconstructed shape of the 3D surface using 90% of the initial points in the finite difference algorithm. The results showed that the estimation of the surface roughness using the proposed method proved to be very accurate to the actual shape.

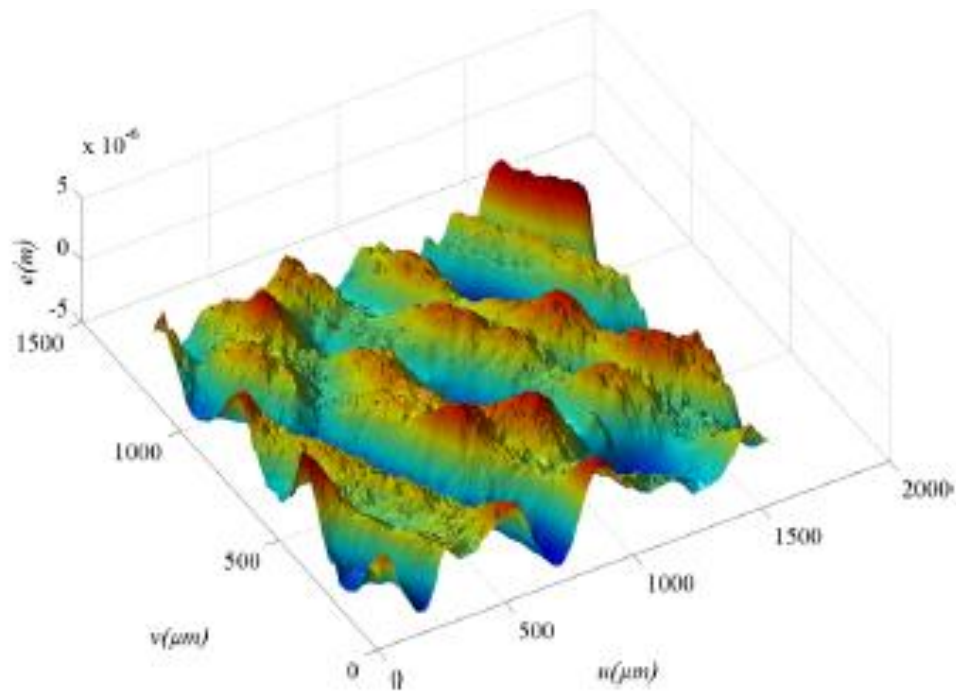


Figure 2.4: Estimation of the 3D Surface Roughness Using 90% of Initial Points.  
[Jamiolahmadi and Barari 2014]

In 2015, Sikder, Barari and Kishawy proposed a new global adaptive slicing technique of Non-Uniform Rational B-Spline (NURBS)-based sculptured surfaces to produce minimum texture error in rapid prototyping [Sikder et al. 2015]. The NURBS representation was extracted from the Computer-Aided Design (CAD) model. The major objective of the research was to optimize the texture error function produced by the staircase effect based on the available range of layer thicknesses using the RP machine. The proposed algorithm dynamically calculated the optimized slice thicknesses based on the RP machine's specifications to minimize the texture error function. The results obtained are compared to results obtained in previous work. The global adaptive slicing technique proved to have greater slicing efficiency, with a 20-50 percent reduction in the number of required layers when compared to other slicing techniques. The proposed methodology also

proved to improve the accuracy of the final manufactured surfaces. Figure 2.5 shows how implementing the adaptive slicing technique can reduce the surface approximation error in RP parts. The image shows a local method, which only applies to the currently constructed region. The proposed global adaptive method applies this method to all features of the part and looks ahead to dynamically calculate the optimum layer thickness for all regions of the rapid prototyped part.

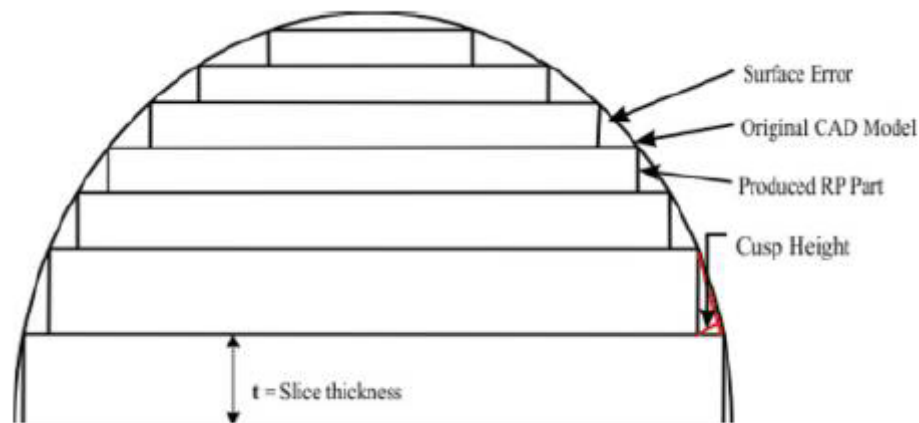


Figure 2.5: Adaptive Slicing Technique Impact on the Staircase Effect.  
[Sikder et al. 2015]

Also in 2015, Boschetto and Bottini proposed a method for surface improvement of FDM parts by Barrel Finishing (BF), which is a post-processing technique [Boschetto and Bottini 2015]. This was done through theoretical and experimental investigation. A geometrical model of the profile under machining was proposed, using a profilometer methodology, based on the alignment of Firestone-Abbot (F-A) curves. This model was compared to an experimental RP model with respect to accuracy and surface roughness. It was found that the deposition angle greatly affected the BF removal speed and altered the nominal dimensions of the part.

Also in 2015, Jamiolahmadi and Barari studied a genetic programming approach to model the detailed surface integrity of AM parts [Jamiolahmadi and Barari 2015]. The goal of the research

was to assess the relationship between the position of the measured points and their corresponding roughness. After estimation of the points, the surface roughness was computed using the arithmetic average of the individual deviations. The resulting function obtained from the genetic algorithm reconstructed the three dimensional surface topography. An accurate representation of the surface roughness was obtained by only using 10% of the initial points, which saved computation time.

Also in 2015, Kaji and Barari evaluated the surface roughness of AM parts based on the modelling of cusp geometry [Kaji and Barari 2015]. An empirical model was presented by obtaining an optical 3D microscopic view of the AM part's profile itself, which was used to conduct the required measurements. The image was then processed to be monochromatic by introducing threshold values. An algorithm was presented to approximate the points on the profile using a piece-wise polynomial. The objective function minimized the total fitting error of the three pieces to the actual measured data points. Figure 2.6 shows the image of the precise surface profile obtained by using an optical 3D microscope and Figure 2.7 shows the piece-wise polynomial used to approximate the shape of the profile.

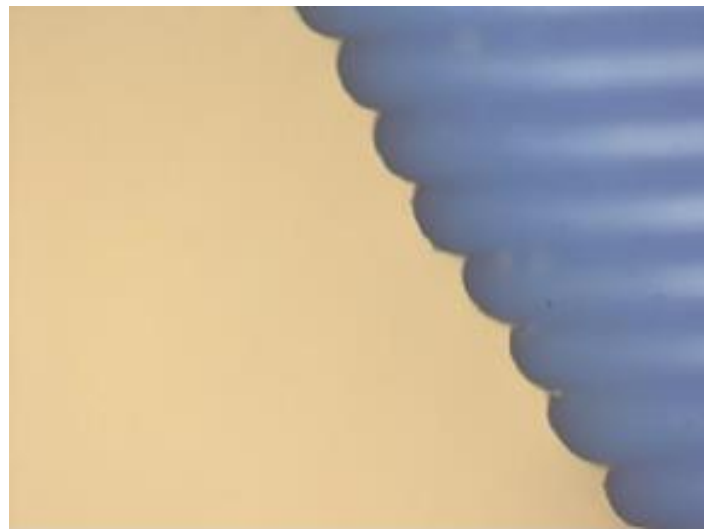


Figure 2.6: Cusp Side View of a 65-degree Slope on a RP Part. [Kaji and Barari 2015]

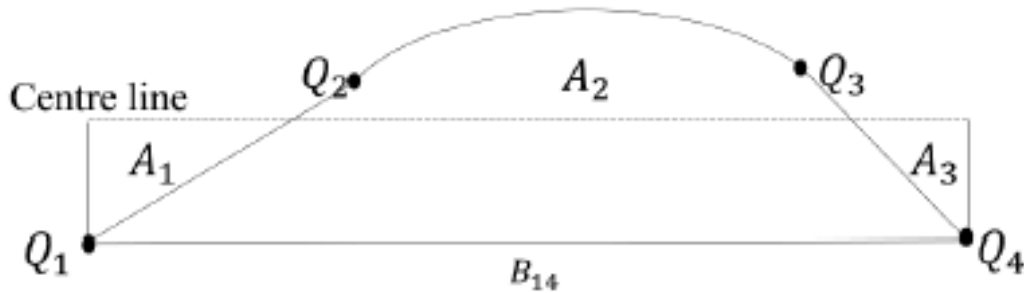


Figure 2.7: Schematic of the Surface Roughness Measurement Using a Piece-wise Polynomial. [Kaji and Barari 2015]

There have been many proposed solutions to the staircase effect and surface quality in general since 2003. The various approaches involved theoretical CAD and image models obtained from software and microscopic equipment, post-processing including chemical finishing and coating, mathematical optimization algorithms used in estimation, proposals of altering the build methods and build parameters, and finally comparison of known model data to a newly proposed model. The research showed extensive findings in working towards better surface quality and reducing the staircase effect, and also showed major improvement in estimation cost and analysis. There will always be a demand to improve the efficiency and quality of AM parts.

### 2.3 LITERATURE ON MECHANICAL PROPERTIES OF COMMON AM APPLICATIONS

In 1996, Giordano, Wu, Borland, L. Cima, Sachs and M. Cima demonstrated the ability of Three Dimensional Printing (3DP) to produce dense polymer parts from a powder bed [Giordano et al. 1996]. Tests were performed to analyze the tensile strength, elastic modulus and strain of

low and high-molecular weight PLA, both isopressed (treated with high temperature and gas pressure in a containment vessel) and not isopressed. A chloroform solvent was used for the binding agent during the build. The mechanical properties were compared to the volume of solvent delivered (per unit area of the part, fabricated from the powder bed, referred to as the binder per unit line length of the powder divided by line spacing (BPULL/LS)). It was found that the strength values of the high molecular weight samples are not at the level of those achieved by conventional melt processing, but the specimens were of sufficient strength to create complex shapes. Also, isopressing significantly increased the tensile strength of low molecular weight PLLA at a BPULL/LS of 480 ( $\text{cc}/\text{cm}^2 \times 10^{-4}$ ), and increased the tensile strength of high molecular weight PLLA at a BPULL/LS of 850 ( $\text{cc}/\text{cm}^2 \times 10^{-4}$ ).

In 2005, Pfister, Walz, Laib and Mulhaupt used a powder blend of Polyacrylic Acid (PAA) with zinc oxide or a mix of zinc oxide and magnesium oxide to produce zinc polycarboxylate during 3D dispensing of an aqueous ink from AM processes [Pfister et al. 2005]. No post-processing treatments were required and a high dimensional accuracy of the models was achieved. The mechanical properties improved with increasing PAA content, ink amount, and decreasing particle size of the sintered zinc oxide ceramic. At a high weight percent of PAA, post-treatment with a zinc acetate solution improved the mechanical properties.

Also in 2005, Shivpuri, Cheng, Agarwal and Babu investigated the 3DP technique for its application to dies for low volume hot forging of 7075 aluminum helicopter parts [Shivpuri et al. 2005]. Parameters studied for the AM tools were thermo-mechanical and tribological behavior. Finite element simulations were used to evaluate and validate the behavior of the fabricated dies during forging. It was found that the AM fabricated materials (ProMetal, a mix of 420 stainless steel (60 percent) and bronze (40 percent)) showed relatively low thermal conductivity and high

friction. Cavities were printed, machined, and evaluated in hot forging trials. Dies showed substantial settling during the 3DP process. Some dies collapsed under high forging pressures.

Table 2.1 shows a comparison of material properties between conventional steel and ProMetal.

Table 2.1: Material Property Comparison of Conventional Steel and ProMetal.  
[Shivpuri et al. 2005]

<b>Material</b>	<b>420 Stainless Steel + Bronze (ProMetal)</b>	<b>Conventional Tool Steel</b>
<b>Hardness (HRC)</b>	26-30	51-55
<b>Ultimate Strength (MPa)</b>	683	1034
<b>Yield Strength (MPa)</b>	455	793
<b>Young's Modulus (GPa)</b>	148	206
<b>Elongation (%)</b>	2.3	9
<b>Thermal Conductivity (W/mK)</b>	8.22	24.4
<b>Density (g/mm<sup>3</sup>)</b>	8.0	7.8
<b>Roughness (μm)</b>	0.57	0.38

In 2008, I. Kim, Song, Jung, Joung, Ryu and J. Kim studied the characterization of inkjet-printed Ag films using sintering to analyze the mechanical and electrical properties of the produced parts [Kim et al. 2008]. It was found that the mechanical properties of the film were strongly dependent on the microstructural development and densification. The specific properties affected were the hardness, modulus of elasticity, tensile strength, and elongation. However, the films were brittle. By the use of pressure-assisted sintering, all mechanical properties were improved. Figure 2.8 shows a stress-strain curve for inkjet-printed Ag films. The gray line represents the sample sintered under atmospheric pressure (normal sintering) and the black line represents the sample sintered under 5 MPa (pressure-assisted sintering).

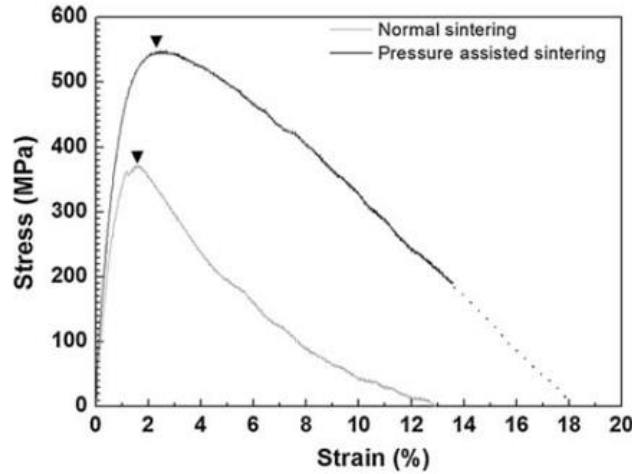


Figure 2.8: Stress-Strain Curves of Normal Sintering and Pressure-Assisted Sintering. [Kim et al. 2008]

In 2009, Kou and Tan implemented heterogeneous objects in 3D printing, which required a large amount of information to be processed simultaneously [Kou and Tan 2009]. Robustness and efficiency became a problem, which were not as critical in homogeneous materials. The goal was to come up with a suitable algorithm for heterogeneous objects implemented in 3D printing. The robustness was improved from using the non-manifold heterogeneous cellular model, which guarantees gap-free material depositions around material interfaces. Efficiency was enhanced by eliminating boundary intersections and using a heuristic material interrogation approach. It was found that a 30 percent efficiency improvement is obtained using the aforementioned approach.

Also in 2009, Sood, Ohdar and Mahapatra printed Acrylonitrile Butadiene Styrene (ABS) using a Fused Deposition Modelling (FDM) machine [Sood et al. 2009]. Five important factors were considered in experiments: layer thickness, build orientation, raster angle, raster width and air gap. Each parameter was studied in terms of its effect on tensile strength, flexural strength and impact strength. The study used empirical methods of relating response to the process parameters, such as analysis of variance (ANOVA). An optimal parameter setting for each response was found.

It was found that small raster angles are not desirable since it increased stress along the deposition and resulted in weak bonding. Tensile strength increased at lower raster angle values and higher air gap values, decreased then increased as a function of layer thickness, and decreased with increasing build orientation.

In 2010, Zanartu-Apara and Ramos-Grez analyzed the parameters layer thickness, binder volume per layer, type of binder and temperature with their effects on mechanical properties of parts made with a Spiral Growth Manufacturing (SGM) printing process [Zanartu-Apara and Ramos-Grez 2010]. Plaster powder by the name of ZP 131 was used as the material for experimentation and the two types of binder fluid used were ZB 60 (comprised almost entirely of water, with traces of soluble polymer and two humectants) and demineralized water. It was found that the layer thickness had the highest effect on apparent density, hardness and flexural strength of the parts.

In 2011, Chimento, Highsmith and Crane analyzed which materials could be used for 3D printing in low volume thermoforming processes for manufacturing medical devices such as orthotics and custom prosthetics [Chimento et al. 2011]. The materials studied were fused powders with post-treatments. They were produced by using the Z-Corp commercial powders and they were post processed using existing and alternate methods (infiltrated with acetone or vapor treated). The desired properties in the analysis were pneumatic permeability, flexural strength and wear rate. These properties were compared to existing plaster compositions which are commonly used in industry. By using modified post process techniques it was possible to replicate the properties of the plaster materials, and even after processed, standard methods could still be applied to modify as necessary. It was found after conducting the experiments that the fused powders had the

necessary strength and permeability to replicate the performance of the current plaster materials used in industry. They also demonstrated superior adhesion to plaster buildup material.

Also in 2011, Renuka, Storti and Ganter investigated an approach to adapting virgin glass and recycled glass to 3DP [Renuka et al. 2011]. Data was presented on shrinkage, porosity and density as functions of peak firing temperature and provided an introduction to the complex topics in finding an adequate method for 3D printed glass. It was found that the shrinkage of the printed recycled glass showed significant anisotropy especially after the peak firing temperature. The average shrinkage ratios for the slow and fast axes to the z-axis were extremely varying, attributed to the layer-by-layer production method and binder burn-off. At 760 C, the porosity reached a minimum, indicative of behavior that resembles a fully dense 3DP glass product. At low firing temperatures, the bulk density was similar to water, but increased to a maximum. This indicated that 3DP recycled glass could behave similarly to virgin glass with acceptable bulk densities. Table 2.2 shows the result of the experiment, the material properties of glass at low and high firing temperatures.

Table 2.2: Material Properties of Recycled Glass. [Renuka et al. 2011]

Peak Firing Temperature		Low	High
Shrinkage	Fast/Z-axis	1:2.74	
	Slow/Z-axis	1:1.37	
Porosity		48.75%	0.36%
Bulk Density		1.25 g/cm <sup>3</sup>	2.41 g/cm <sup>3</sup>

In 2012, Li, Zhang and Yin used three techniques to make three different porous Si<sub>3</sub>N<sub>4</sub> ceramics [Li et al. 2012]. Only one of these methods consisted of a 3D printing technique, which was 3D printing combined with pressureless-sintering (3DP-PS). Mechanical properties for these ceramics depended on the microstructure type, phase composition, linear shrinkage, pore size

distribution and porosity. It was found that the 3D printing technique used had lower flexural strength, fracture toughness, Young's modulus and hardness than the other two techniques used. It also had the highest linear shrinkage, which didn't seem to make the process a very viable alternative compared to others.

Also in 2012, Zeng, Guo, Jiang, Yu, Liu, Shen, Deng and Wang studied the mechanical properties of Wood-Plastic Composite (WPC) parts fabricated by Selective Laser Sintering (SLS) [Zeng et al. 2012]. The intensity of the laser was analyzed in determining this effect. The mechanical properties of the parts were improved by infiltrating the produced part with wax as a post-processing technique. It was found that the interfacial adhesion and densification are improved by increasing the laser intensity. This caused the impact strength to be gradually increased with or without post-processing infiltration. However, the tensile strength and bending (flexural) strength of the parts increased gradually only when infiltrated with wax. At best performance, the tensile strength increased by 191% and the flexural strength improved 17%. The impact strength improved to a maximum of 543% and the impact strength improved to a maximum of 147%. When increasing the laser intensity past the maximum performance values, the mechanical properties decreased in strength, since the higher temperature caused the melt viscosity to drop.

In 2013, Baechler, Devuono and Pearce studied the use of High Density Polyethylene (HDPE) as a 3D printing material [Baechler et al. 2013]. The material was obtained by shredding waste products, such as bottles. HDPE was chosen because it is relatively stiff and has a higher tensile strength than other polyethylenes, and it is also more prevalent in the waste stream than ABS or PLA. Using waste material has a lower cost and reduces the environmental impact of rapid prototyping. This could serve as a sustainable development tool, by recycling HDPE into alternate

materials and encouraging in-house recycling of plastic waste. The parameters studied in this work were the resultant filament consistency, energy per use of filament and process times. Filaments were measured at the section midpoint using a micrometer. Energy consumption was measured as a function of shredding the material, the auger drive and heating at each stage of filament production. The process time included the time required to shred the material, and to heat and extrude the filament. It was found that 87 percent of filament diameters were acceptable and that there was less energy usage (40 percent more economical) by using recycled HDPE than purchasing the filament commercially. Table 2.3 shows the mechanical properties of HDPE.

Table 2.3: Mechanical Properties of HDPE. [Baechler et al. 2013]

<b>Property</b>	<b>Value</b>
Density (kg/m <sup>3</sup> )	950
Thermal Expansion Factor (10 <sup>6</sup> /K)	100-200
Poisson's Ratio	0.46
Friction Factor	0.29
Rockwell Hardness (shore)	D 60-73
Elastic Modulus (GPa)	0.5-1.2
Impact Resistance, IZOD (J/m)	20-210

Also in 2013, Ivanova, Williams and Campbell studied existing literature in which nanostructures were incorporated into AM processes to improve the final part's performance [Ivanova et al. 2013]. Materials studied in this work were metal, ceramic, and carbon nanomaterials, which have been implemented in stereolithography, laser sintering, fused filament fabrication and three-dimensional printing. It was found that the addition of nanostructured materials into printing media greatly affected the properties of the final produced parts. Some of the improvements that nanostructures brought to a final product was distortion resistance and decreased shrinkage. They also increased thermal and electric conductivity, lower sintering

temperatures and improved dimensional accuracy. However, many challenges still existed, such as nozzle clogging, aggregation within printing media, rough surface finish on printed parts and more.

Also in 2013, Polzin, Spath and Seitz analyzed a new 3DP process based on Polymethyl Methacrylate (PMMA) material [Polzin et al. 2013]. Some standard parts were designed and created using the machine. It was found that the mechanical properties of PMMA were sufficient, as shown in Table 2.4, for the intended applications of parts as functional prototypes or for investment casting. The mechanical properties could be improved by being infiltrated with epoxy and the surface quality of the parts could be improved by being infiltrated with wax. This was the first paper that studied the usage of PMMA material in a 3DP process. The process parameters of the machine itself had to be further optimized, such as increasing printing resolution and reduction of satellite drops by adjusting printhead drive parameters. Reducing the particle size of the PMMA granulates allowed thinner layers, which improved build resolution as well as improved surface roughness.

Table 2.4: Material Properties of PMMA (Poly Methyl Methacrylate). [Polzin et al. 2013]

<b>Treatment</b>	Untreated	Infiltrated with epoxy
<b>Tensile Strength</b>	2.91 MPa	26.6 MPa
<b>Modulus of Elasticity</b>	223 MPa	1,190 MPa
<b>Minimum Feature Size</b>	0.3 mm	

In 2014, Zhu, Li, Tian, Wang and Liu analyzed the use of laser additive manufacturing to provide an attractive potential for manufacturing titanium alloy components [Zhu et al. 2014]. Hardness and tensile strength mechanical properties were investigated. When the sample was built, three different areas on the part were named. The zones were the laser additive manufactured zone (LAMZ), the wrought substrate zone (WSZ), and the heat affected zone (HAZ) due to the rapid

cooling rate. It was found that, once the part was fabricated, there was good bonding between the LAMZ and WSZ. The tensile properties were found to be the greatest between these zones (in the HAZ). The hardness was found to increase noticeably in the transition zone of the HAZ (from the WSZ to the HAZ).

Also in 2014, Olivier, Borros and Reyes derived a customer-driven and integrative methodology to develop materials [Olivier et al. 2014]. It was desired to prioritize the several variables involved in a new material application developed for 3D printing. The material developed was an alumina-starch-based powder. The powder was designed and developed for 3D printing of refractory supports for metal casting moulds. The Quality Function Deployment (QFD) method was applied. Six process and material variables were considered to drive a prioritization analysis using a design of experiment array. Compressive resistance of the material was measured and assessed. The mechanical properties of the powder are shown in Table 2.5. It was found that the QFD analysis delivered irrelevant factors and target values for intermediate step parameters. Sintering parameters were found as the most influential for compressive resistance.

Table 2.5: Material Properties of Alumina-based Powder. [Olivier et al. 2014]

<b>Viscosity</b>	0.22 Pa.s
<b>Compressive Strength</b>	2.60 MPa
<b>Density</b>	1 g/cm <sup>3</sup>
<b>Mechanical strength after sintering</b>	2.40 MPa

Also in 2014, Patricio, Domingos, Gloria, D'Amora, Coelho and Bartolo studied the effect of poly lactic acid (PLA) addition into poly (ε-caprolactone) (PCL) matrices, as well as how the morphological, thermal, chemical, mechanical and biological performance of the 3D final parts were influenced by the mixing process [Patricio et al. 2014]. Melt blending and solvent casting were the processes used to prepare the PCL/PLA blends. Scanning electron microscopy (SEM),

simultaneous thermal analyzer (STA), nuclear magnetic resonance (NMR), static compression analysis and Alamar Blue™ techniques were all used to evaluate the scaffold's properties. It was found that the addition of PLA to PCL scaffolds greatly improved the biomechanical performance of the final printed parts. Also, blends obtained by solvent casting gave better mechanical and biological properties compared to those created by melt blending, as shown in Table 2.6.

Table 2.6: Material Properties for PCL and PLA Hybrids. [Patricio et al. 2014]

<b>Material</b>	<b>Compressive Modulus E (MPa)</b>	<b>Maximum Stress <math>\sigma</math> (MPa)</b>
PCL	18.7 +/- 3.0	4.4 +/- 0.4
PCL/PLA (blends prepared by melt blending)	146.5 +/- 14.0	18.5 +/- 1.3
PCL/PLA (blends prepared by solvent casting)	112.3 +/- 13.7	28.0 +/- 5.0

Also in 2014, Pires, Gouveia, Rodrigues and Fonte conducted an analysis based on sintered Hydroxyapatite (HA) samples produced by 3DP is presented [Pires et al. 2014]. This work was a part of another, which considered the fabrication of calcium phosphates implants by 3DP. A thorough knowledge of the impact of sintering temperature on physical and mechanical properties of porous HA was critical before considering any complex structures, such as scaffolds or implants. HA samples were analyzed by using x-ray diffraction, Scanning Electron Microscope (SEM) and uniaxial compression tests. The 3DP parameters used to create the HA samples led to higher accuracy and stability. It was found that sintering temperature and powder morphology influenced densification behavior, porosity, phase stability, mechanical strength and the tangent modulus of the HA samples the most. The optimal post-processing sintering temperature led to the best porosity, microstructure, phase stability and mechanical properties of HA.

Also in 2014, Tymrak, Kreiger and Pearce investigated the use of an at the time recent development in 3D printing, the RepRap machine, which is open-source and self-replicating

[Tymrak et al. 2014]. It is a low-cost alternative to other expensive machines available commercially. The materials studied in this work were acrylonitrile butadiene styrene (ABS) and polylactic acid (PLA). Tensile strength, strain, and modulus of elasticity of each material was measured as a function of layer height and orientation after printing on several RepRap machines, as shown in Table 2.7. It was found that the parts were comparable in strength to those that are printed on more expensive, commercially available machines. ABS was found to have a tensile strength of 28.5 MPa and PLA was found as 56.6 MPa. The elastic modulus was found to be 1807 MPa for ABS and 3368 MPa for PLA. Clearly PLA is the stronger material.

Table 2.7: Mechanical Properties of ABS and PLA. [Tymrak et al. 2014]

	Specimens Tested	Specimens Considered	Average Tensile Strength (MPa)	Average Strain at Tensile Strength (mm/mm)	Average Elastic Modulus (MPa)
<b>ABS</b>					
0.4 mm layer height	30	24	28.2	0.0197	1875
0.3 mm layer height	40	39	27.6	0.0231	1736
0.2 mm layer height	40	35	29.7	0.0201	1839
0/90 Orientation	60	52	27.7	0.0192	1867
+45/-45 Orientation	50	46	29.5	0.0233	1739
Total	110	98	28.5	0.0212	1807
<b>PLA</b>					
0.4 mm layer height	30	17	54.9	0.0194	3286
0.3 mm layer height	40	31	48.5	0.0171	3340
0.2 mm layer height	20	18	60.4	0.0196	3480
0/90 Orientation	50	27	54.9	0.0188	3336
+45/-45 Orientation	40	39	52.3	0.0181	3384
Total	90	66	56.6	0.0193	3368

Since 1996, extensive research has been done based on the mechanical properties of materials used in a variety of AM applications. Different materials have different properties, and also different applications that work with them. By studying the mechanical strength of these materials in a variety of ways, it becomes clearer to understand what kind of material needs to be used in the AM process. Stronger materials are not always the best alternative, as there is usually a trade-off between high strength and cost. It is the responsibility of the engineer to select the material based on the extent of the finished part's use, as well as assess the risks of part failure.

## **2.4 LITERATURE ON BIOMATERIAL AM APPLICATIONS**

In 1999, Wheeler, Corey, Brewer and Branch provided an introduction of integrating cell growth with 3D printing technology [Wheeler et al. 1999]. Microcontact printing created precise patterns of proteins, which controlled growth of hippocampal neurons in culture. This additive, multi-mask technique permitted several different molecules to be patterned on the same substrate. The covalent linker technology permitted relatively long-term (two-week) compliance of neurons to the stamped pattern against a polyethylene glycol background. When polylysine was stamped adjacent to a laminin/polylysine mixture, neural somata and dendrites preferred the polylysine while axons prefer the mixture or the border between the two. There are no actual results on a 3D printing process in this paper, just fundamental theory.

In 2003, Yan, Wu, Zhang, Xiong and Lin discussed an important subject called bio-manufacturing [Yan et al. 2003]. The hierarchy of bio-manufacturing (low grade: undegradable material used to perform permanent organ replacement, and high grade: biodegradable material

used to repair organ damage) was investigated by using an FDM AM process. The resulting bone and cartilage samples were tested on dogs and rabbits. The material used was a low grade biomaterial is HDPE (high density polyethylene), due to its ease of extruding, high melt index and high cohesiveness. It was found that the artificial cartilage planted in the rabbits for 3 months had developed well. The material used as a high grade biomaterial was a composite of Polylactic Acid (PLLA) and Tricalcium Phosphate (TCP). A composite was used to increase the mechanical strength and improve the regeneration properties of the material. It was found that the material had high porosity and similar properties to human bones.

In 2004, Roth, Xu, Das, Gregory, Hickman and Boland introduced a method of applying high-throughput inkjet printing to control cellular attachment and proliferation by precise, automated deposition of collagen [Roth et al. 2004]. Glass microscope cover slips were used as substrates and collagen (most common protein in the body) was used as the printing material. After running several iterations of tests, it was found that a pH value of 5.5 and above raised the viscosity substantially, so it is important to print with a solution of low pH, as shown in Figure 11. Failure to do so would most likely result in nozzle blockage, cutting production. Results showed that viable cellular patterns with a resolution of 350 microns can be created through the bioprinter, which used a fused deposition process of biologically active proteins.

In 2005, Fang, Starly and Sun investigated a computer-aided design (CAD) approach to characterize the mechanical properties of porous tissue scaffold [Fang et al. 2005]. The interface between the CAD characterization and the design model, as well as the development of a computational algorithm for finite element implementation and numerical solution of asymptotic homogenization theory were all investigated. The research used Hydroxyapatite (HA), Polycaprolactone (PCL) and a copolymer of polylactic acid and polyglycolic acid for biomaterials

as the scaffold in testing. The machine used a Precision Extruding Deposition (PED) process, since there was no filament preparation required unlike a Fused Deposition Modeling (FDM) process. It was found that the mechanical properties of the scaffold were functions of layout pattern, the porosity and the scaffolding materials used. The effective mechanical properties decreased with increasing fill gap.

In 2007, Boland, Cui, Chaubey, T. Burg, Groff and K. Burg developed a fabrication technique that allowed precise placement of cells inside biomaterial constructs [Boland et al. 2007]. The experimental method used an inkjet machine to print cells onto a polymer scaffold in order to study cell-surface interactions. The cells were printed on Polylactide (PLLA) fiber and once printed were analyzed using fluorescent light. It was found that after 16 days of culture, the cells completely covered the PLLA surface and cell death was minimized.

In 2008, Yasar, Dinh, Lan and Starly investigated a maskless photopolymerization approach to create micropatterned hydrogels with feature sizes in the range of 50 microns [Yasar et al. 2008]. This was done through direct exposure of the polymer to ultraviolet radiation. The hydrogels can be used for applications in bone and cartilage tissue engineering. After printing the hydrogels in varying concentrations ranging between 20 and 80 percent, strands as small as 80 microns with a minimum layer thickness of 30 microns were possible. It was also found that 3D objects could be created by continuous addition of the photopolymer resin to the vat.

In 2009, Xu, Moon, Emre, Lien, Turali and Demirci investigated the feasibility of bioprinting cell-laden hydrogel to fabricate CBBs at high throughput [Xu et al. 2009]. Cell response was tracked using lenseless Charge-Coupled Device (CCD) technology. It was found that a cell-laden collagen printing platform was capable of immobilizing cells in collagen drops with spatial control and pattern the cells onto the surface. Cell viability was achieved and the cells

proliferated over 5 days. The immobilized cells maintained their biological and physiological sensitivity through environmental temperature change and adding of de-ionized water. The CCD technology was able to detect the morphology change of the cells under environmental change, which was essential for the biosensor's portability.

In 2010, Pepper, Cass, Mattimore, T. Burg, Booth, K. Burg and Groff evaluated four research methods for processing samples after bioprinting but prior to adding factors for incubation [Pepper et al. 2010]. An inkjet cartridge based bioprinter was used to print several different-treated samples. In the first treatment, after 60 minutes the sample was sprayed with a nebulizer. In the second treatment, collagen was pipetted onto the sample after 60 minutes. In the third treatment, after 30 minutes the sample was sprayed with a nebulizer, then at 60 minutes collagen was pipetted on top of the sample. In the last treatment, a specific salt solution was applied using the machine itself immediately after the sample was printed. Then, after 60 minutes, collagen was pipetted onto the surface. Results show that the last method (method 4), using the salt solution immediately after printing, proved to be the best alternative in terms of cell viability and pattern fidelity.

In 2012, Savalani, Hao, Dickens, Zhang, Tanner and Harris identified the most influential parameters on the micro and macro pore morphologies of sintered Hydroxyapatite (HA)-polymer composites [Savalani et al. 2012]. The effects of various processing parameters on physical properties such as open porosity, average pore width and percentage of pores enabling bone regeneration and ingrowth of sintered parts were investigated using a two-level full factorial experiment. Optical microscopy combined with the interception method was used to determine the average pore size and proportion of pores suitable to allow bone regeneration. Seen in Figure 2.9, the results show that the layer thickness is the most influential parameter. The energy density

equation with the layer thickness parameter provided a better estimation of part porosity of composite samples than without the layer thickness parameter included in the equation.

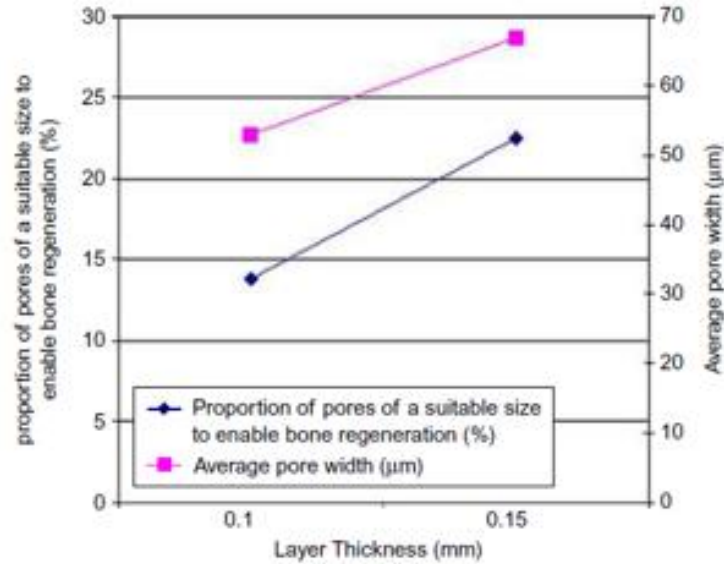


Figure 2.9: Effect of Layer Thickness on Average Pore Width and Proportion of Pores. [Savalani et al. 2012]

In 2013, Wang, Qinghua, Pan, Mingming and Shengmin investigated the use of a Hydroxyapatite/Poly a-n-Butyl Cyanoacrylate (HA/NBCA) composite system in 3D printing processes for the application of bone scaffolds [Wang et al. 2013]. NBCA was considered to be the binder and HA was considered as the printing surface. The only mechanical property analyzed in this experiment was Young's modulus (modulus of elasticity). Simulations were done using the software Material Studio. It was found that when attaching 60 monomers to the NBCA material, Young's modulus was maximized. Any less or more than this amount decreased the modulus of elasticity significantly. The HA/NBCA composite was found to be much, much stronger than just the pure HA system.

Also in 2013, Ozbolat and Yu published a literature review on the status of organ printing [Ozbolat and Yu 2013]. The purpose of the paper was to identify the current shortcomings in

current research on the subject, and where the industry will likely go. It was discussed that the major challenges in realizing a true organ fabrication process is the mechanical integrity of the printed organs, as well as the integration of a proper vascular network with the rest of the organ. The authors state that, in order for 3D printing of organs to become a reality, some of the upcoming research would involve blueprint modeling of the organ's architecture, generation of a process plan for bioprinting, isolation of stem cells, differentiation of stem cells into organ-specific cells, preparation and loading of organ-specific cells and blood vessel cells, as well as support medium, and finally a bioprinting process followed by organogenesis in a bioreactor for transplantation.

Also in 2013, Zhang, Yu and Ozbolat provided a better idea of cell culture used in engineering in an AM process [Zhang et al. 2013]. Despite the progress at the time in tissue engineering, there were several challenges that had to be addressed in order for organ printing to become a realization. One of the challenges was an implication of a vascular network. The most likely solution to this problem was the implementation of microfluidic channels. However, this was difficult to integrate in 3DP technology. The microfluidic channels were printed in the form of hollow tubes. Alginate and chitosan hydrogels were used to fabricate the channels and show the versatility of the process. The channels were printed and embedded within hydrogel to test functionality through perfusion of cell type oxygenized media. It was found that the microfluidic channels showed promise towards the implementation of vascular networks.

In 2014, Lei, Frank, Anderson and Brown presented a new method for representing heterogeneous materials using nested STL shells, based on the density distributions of human bones [Lei et al. 2014]. The nested STL shells were called the Matryoshka models, which are stacked inside one another to represent different material regions. The model addressed the challenge of representing different densities and different types of bone when reverse engineering

from medical images. It was generated from iterative process of thresholding the Hounsfield Unit (HU) data by using Computed Tomography (CT). This delineated regions of gradually increasing bone density. The shells themselves were representative of the bone marrow up through and including the bone surface. It was found that this approach could be used to properly represent accurate models of heterogeneous materials in an automated way, eliminating the need to manually create an assembly model for additive or subtractive manufacturing.

Also in 2014, Patricio, Domingos, Gloria, D'Amora, Coelho and Bartolo studied the effect of Poly Lactic Acid (PLA) addition into Poly (ε-Caprolactone) (PCL) matrices, as well as how the morphological, thermal, chemical, mechanical and biological performance of the 3D final parts were influenced by the mixing process [Patricio et al. 2014]. Melt blending and solvent casting were the processes used to prepare the PCL/PLA blends. Scanning Electron Microscopy (SEM), simultaneous thermal analyzer (STA), Nuclear Magnetic Resonance (NMR), static compression analysis and Alamar Blue™ techniques were all used to evaluate the scaffold's properties. It was found that the addition of PLA to PCL scaffolds greatly improved the biomechanical performance of the final printed parts. Also, blends obtained by solvent casting gave better mechanical and biological properties compared to those created by melt blending.

Biomaterial AM research has come a long way since 1999. Researchers are getting closer in achieving integrated organ tissue production by means of AM. Such a milestone would save countless lives all over the world through the ability to fabricate organs for transplants on demand. The materials for this area of research are costly however, and there are hundreds of organs with different tissue structures and with different cellular networks. It may be a while until the goal can be fully realized, research priority should be given to the essential organs first and the minor organs, which are not required to live, should be analyzed in the future.

## 2.5 LITERATURE ON STEREOLITHOGRAPHY AM APPLICATIONS

In 1984, Otsubo, Amari and Watanabe performed a study of the curing of photoresin and the effect from varying light intensities, dynamic viscosity of the resin, sample/layer thickness and exposure energy on the sample area [Otsubo et al. 1984]. The ultraviolet light source used had a wavelength of 365 nm. Experiments were conducted with an oscillating plate rheometer. Results showed that the minimum exposure energy, required to initiate photopolymerization, increased with increasing sample thickness. Also, a sample thickness greater than 100  $\mu\text{m}$  shows a substantial increase in the minimum exposure energy. Figure 2.10 shows a graph of dynamic viscosity of the photoresin as a function of exposure time, with three different line plots shown by varying light intensity. The dynamic viscosity increased rapidly due to polymerization (fast rate of curing) until the slope became linear. Curing the parts past this point still increased the viscosity of the photoresin.

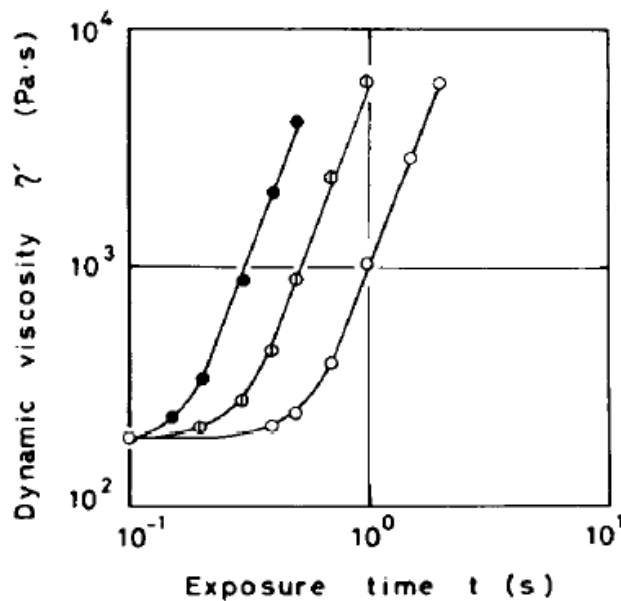


Figure 2.10: Dynamic Viscosity vs Exposure Time for 3 Different Light Intensities (from left to right: 70, 37, 20 (mW/cm<sup>2</sup>)). [Otsubo et al. 1984]

In 1986, Otsubo, Amari, and Watanabe did another study on the UV curing of epoxy acrylate photoresin [Otsubo et al. 1986]. This time, using thin films, the sample thickness dynamic viscosity as a function of monochromatic light exposure energy was investigated. The same process was used to conduct experiments as the previous work. As can be seen in Figure 2.11, the minimum exposure energy increased with increasing sample thickness, which resulted in the inconsistency of curing in the direction perpendicular to the shearing surface.

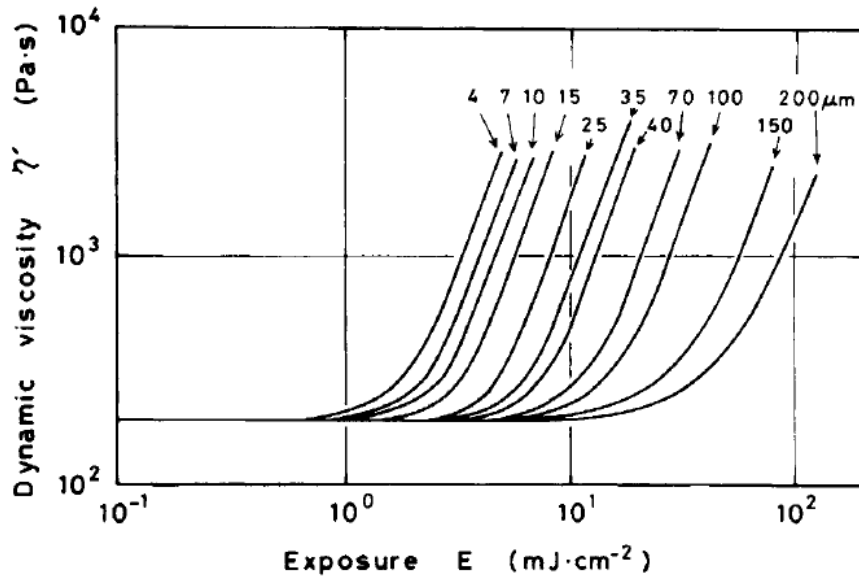


Figure 2.11: Dynamic Viscosity vs. Exposure Energy for Several Sample Thicknesses. [Otsubo et al. 1986]

It was found that the ability to cure a film is dependent on the light intensity at a given depth of the film. Theoretical results were compared to actual results, which were accurate. Equation 2.1 shows the minimum exposure energy required for a given sample thickness:

$$E_m = \left(4.2 \frac{mJ}{cm^2}\right) \exp\left(\frac{h}{120 \mu m}\right) \quad (2.1)$$

Where  $h$  is the given sample thickness. This equation can be used for any sample thickness.

In 1996, Cunningham and Wells performed a study on the UV curing of acrylate resins versus cationic epoxies by using a simple screening process [Cunningham and Wells 1996]. Each type of resin was examined with respect to the parameters clarity, color, cure speed, time to develop adhesion and adhesion to various substrates. The screening tests were done by taking 0.2 gram resin bead and 1/16-inch – 1/8-inch thick resin on polycarbonate substrate. The samples were then cured according to the conditions. Adhesion was measured by picking with a dental probe placed at about 45 degrees between the bead and substrate. Results showed that a 30-second exposure time was sufficient to cure all of the products being tested, with the acrylate resins curing much quicker than the epoxy resins. Epoxies can be substantially affected by common workplace variables such as humidity, have reasonable adhesion to a variety of substrates and maintain their properties to high temperatures. Acrylates generally have superior adhesion, cure speed and impact resistance. Adhesions were measured with an Instron and pulled at 0.1 inch/minute on a 0.25 sq-in area and rated on a basis of 1-5, with 1 being the strongest bond and 5 being the weakest bond. Adhesion strength was recorded once for the product at 15 minutes after the cure and then again after one full day.

In 1997, Decker did a study on the use of UV irradiation in polymerization [Decker 1997]. The effect of both the light intensity and temperature on the rate of polymerization and curing time was studied, by using a real-time infrared spectroscope. The resin studied consisted of mainly acrylate monomers, mainly because of their high reactivity. Figure 2.12 shows the results of the parameters monomer conversion rate and temperature on the curing time. The dotted lines show the effect of light intensity on polymerization and the solid lines show the temperature profiles.

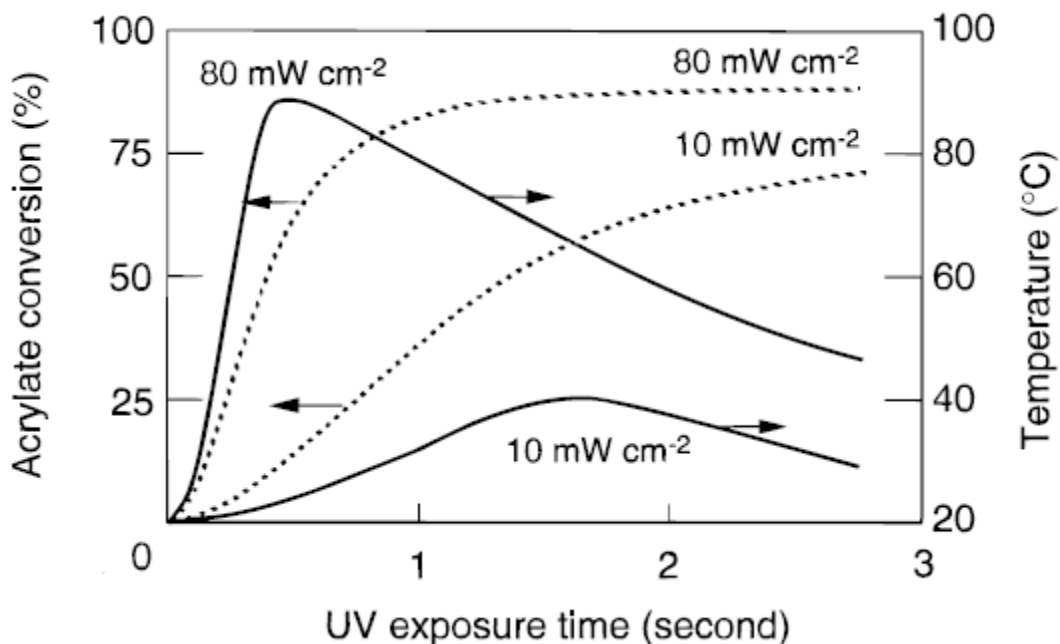


Figure 2.12: Rate of Polymerization and Temperature as a Function of UV Curing Time. [Decker 1997]

Two levels of light intensities were investigated,  $10 \text{ mW cm}^{-2}$  (lower) and  $80 \text{ mW cm}^{-2}$  (higher). The higher intensity reached a maximum temperature of  $90^\circ\text{C}$  and the lower intensity reached a lower maximum temperature of  $40^\circ\text{C}$ . The higher the light intensity, the better the rate of monomer conversion and thus the better the rate of polymerization.

In 1999, Crivello did a study on UV and electron beam-induced cationic polymerization, as it had not been investigated thoroughly previous to that time [Crivello 1999]. Through experimentation, an optimal photoinitiator as well as its optimal concentration for curing were found using both methods. The optimal photoinitiator would reduce the cure time required to cure fully as well as increase the shelf life. Cationic polymerization was the most versatile type of polymerization known, as it can be used for several applications, including but not limited to

coatings, adhesives, printing inks, stereolithography resins, microelectronic photoresists, electronic encapsulants and composites. Experiments for UV polymerization were conducted using a real-time infrared spectroscope and experiments for e-beam polymerization were conducted using a low energy (165 keV) Energy Sciences, Electro-curtain Electron Beam Apparatus. The photoinitiators that gave the best results consisted of onium salts. By synthesis with several strong acids, the photoinitiator's structure was modified and the results were analyzed. Figure 2.13 shows one example studied, the conversion rate of monomer (rate of polymerization) as a function of irradiation time for several structures of diepoxyalkane monomers.

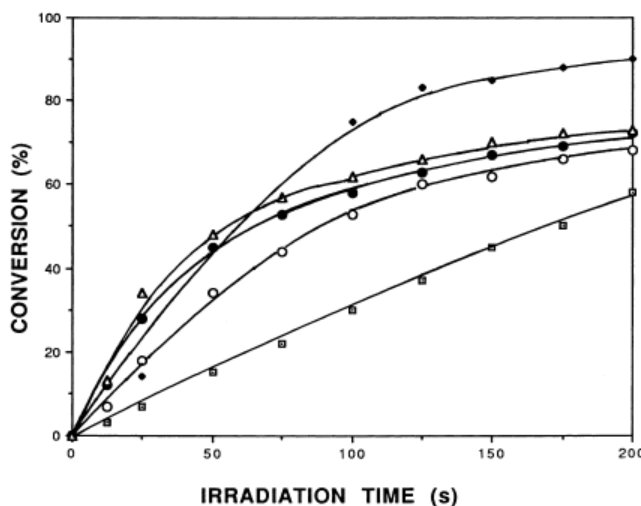


Figure 2.13: Rate of Polymerization as a Function of Irradiation Time for Several Structures of Diepoxyalkane Monomers. [Crivello 1999]

In 2001, Lee, Prud'homme and Aksay did a study on the depth of curing on a model resin as a function of photoinitiator concentration [Lee et al. 2001]. Direct measurements of sample thickness were made on cured methacrylate monomer, which was polymerized in a solution of trichloroethylene with a UV light source at 325 nm. These solutions were cured using varying levels of photonic energy and photoinitiator concentration. The photoinitiator concentration that

maximized the sample cure depth was discovered. The study showed that the photoinitiator concentration has a significant impact on the quality and performance of the finished sample, especially when considering the layer thickness. Figure 2.14 shows the results of several experiments, plotting the cure depth as a function of both the photoinitiator concentration and given energy dosage.

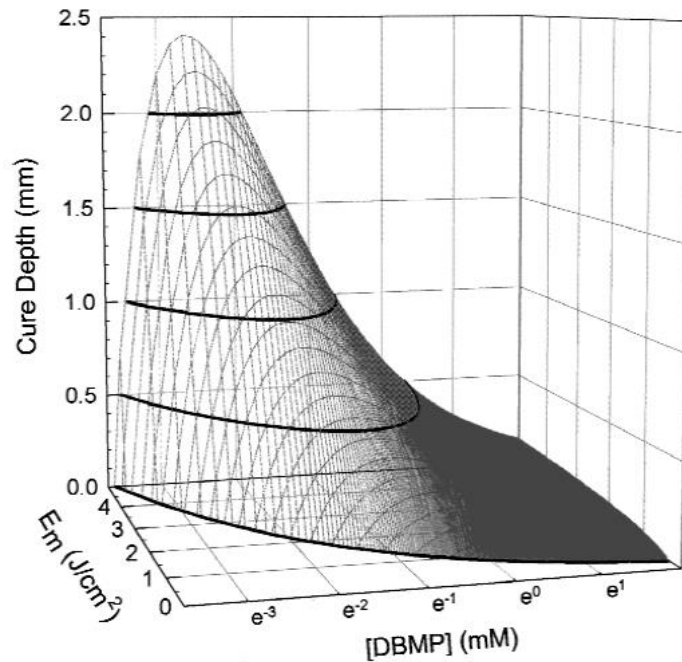


Figure 2.14: Cure Depth as a function of Energy Dosage and Photoinitiator Concentration. [Lee et al. 2001]

The cure depth increased exponentially as energy dosage increased, while cure depth increased initially with increasing photoinitiator concentration, obtained a maximum and then converged.

Also in 2001, Stowe studied UV curing in terms of its advantages, applications and comparisons to other curing processes [Stowe 2001]. UV curing can be used on coatings, for inks and for adhesives. This involves several industries, including automotive components, medical

products, electronics, CDs/DVDs, two-piece and three-piece can printing, pipe and tube coating, furniture, fiber optics, flooring, packaging and containers. Stowe stated that UV curing has lots of economic benefits compared to other curing processes, as well as higher yield, reduced setup time, reduced waste and scrap, more efficient use of space, reduction of work-in-process, increased productivity, energy savings and improved quality and performance. Figure 27 shows a map of the UV curing process, covering formulation, products and lamp types.

In 2007, Umezaki and Abe studied the effect of stress and temperature in the curing process of UV curable resin at varying wavelengths [Umezaki and Abe 2007]. Measurements were made using a photoelastic apparatus, a thermographic apparatus and a beam splitter, able to reflect infrared light and transmit visible light. Liquid resin was poured into a cavity (3 mm thick, 2 mm high and 76 mm wide) and specimens were illuminated for two different wavelength ranges, one from 220-325 nm and the other from 325-385 nm using a specific light intensity for 300 seconds. This indicated that the curing process started occurring from the upper part of the resin and over time continued downwards. Temperature of the first range of wavelength of light was lower and had a slower variation than the second range of wavelength of light used to cure the specimens. Through this research, it was discovered that stress and temperature during the curing of the UV resin were affected by the UV wavelengths of the light rays.

In 2014, Lin, Liu and Cheng worked on investigating the kinetics of photopolymerization under a collimated and reflecting focused ultraviolet laser [Lin et al. 2014]. A thick polymer was used to achieve improved polymerization efficiency and uniformity. The UV light was focused with the use of a concave mirror to compensate for the exponential decay in the resin. The initiator concentration was solved for numerically using the polymerization kinetic equation. The crossover time was determined with several UV beam setups (single, two collimated, collimated plus

reflecting focused-beam). Figure 2.15 shows results of the normalized photoinitiator concentration as a function of polymer thickness for the 3 different cases. The solid curve is represented by the collimated beam without the reflecting beam, the dashed curve is represented by the collimated beam and the collimated reflecting beam, and the dotted curve is represented by the collimated beam with a focused reflecting beam. The graph on the left shows the results at 17 seconds of exposure time and the graph on the right shows the results at 24 seconds of exposure time.

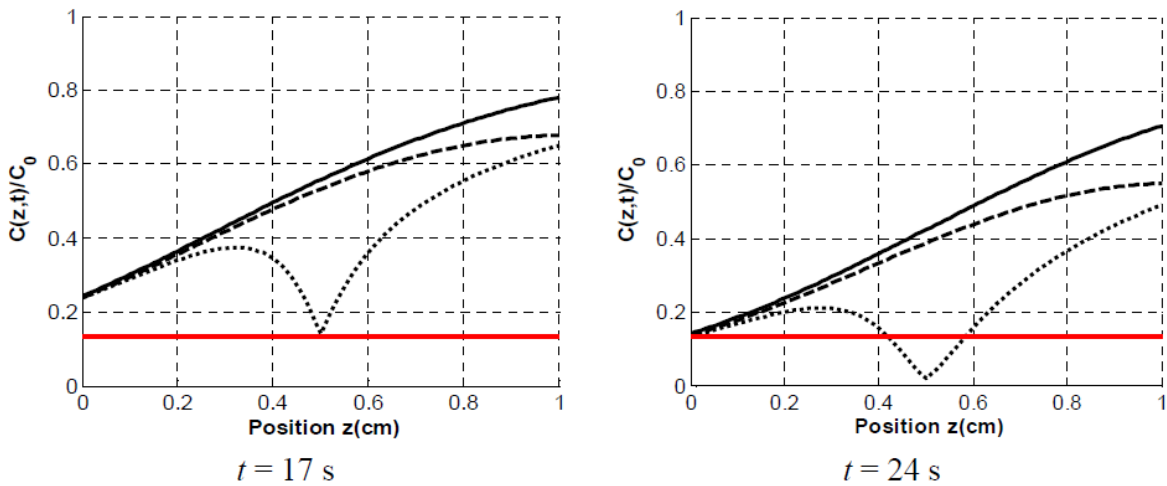


Figure 2.15: Normalized Photoinitiator Concentration vs Layer Thickness of the Resin at 17s (left) and 24 s (right) Exposure Time. [Lin et al. 2014]

Generally, the concentration is lower if the resin is cured for a longer period of time.

Also in 2014, Nam, Shimatsu, Matsushima, Kimura and Kishida did a study on the UV photopolymerization of PMMA inside decellularized dermis [Nam et al. 2014]. Methacrylate and a photoinitiator (Irgacure 184) were applied to the decellularized dermis tissue, which was polymerized using UV light. The process took around 40 minutes to complete, however the

researchers found that the rate and depth of polymerization could be adjusted by mixing Irgacure 184 and Irgacure 819, another photoinitiator. This also increased mechanical strength of the final product. Table 2.8 shows the results of three different mole ratios of Irgacure 184 and the combination of Irgacure 184 and Irgacure 819.

Table 2.8: Conversion and Molecular Weight of PMMA Obtained by UV Curing.  
[Nam et al. 2014]

<b>Initiator</b>	<b>Nomenclature</b>	<b>T<sub>max</sub> (°C)</b>	<b>t<sub>max</sub> (min)</b>	<b>Conversion (%)</b>	<b>M<sub>n</sub> (g/mol)</b>	<b>M<sub>w</sub> (g/mol)</b>	<b>M<sub>w</sub>/M<sub>n</sub></b>
Irgacure 184	sMMA200	78.2 ± 12.5	35	64.4 ± 2.4	70,000	150,000	2.18
	sMMA40	73.9 ± 2.6	35	84.9 ± 6.8	50,000	130,000	2.66
	sMMA20	59.6 ± 2.3	45	87.7 ± 2.2	51,000	120,000	2.42
Irgacure 184 + Irgacure 819	dMMA200	67.3 ± 12.3	20	74.8 ± 5.8	80,000	220,000	2.73
	dMMA40	51.9 ± 2.9	25	60.3 ± 8.1	60,000	340,000	2.70
	dMMA20	57.1 ± 2.3	30	56.0 ± 6.8	370,000	370,000	2.84

The mole ratios used are 200:1, 40:1 and 20:1 (hence the 200, 40, 20 in the nomenclature). *T* is the temperature, *t* is the exposure time, *Conversion* is the rate of polymerization, *M<sub>n</sub>* is the molecular weight of the photoinitiator in the mix and *M<sub>w</sub>* is the molecular weight of the entire mix. The

Irgacure 184 + Irgacure 819 photoinitiator with mole ratio of 200:1 had the lowest cure time required, whereas the Irgacure 184 photoinitiator with mole ratio of 20:1 had the highest cure time required. However, this photoinitiator had the highest conversion rate.

Also in 2014, Ebrahimi and Bastani studied the effect of formulation on the mechanical and physical properties of UV curable urethane acrylate resins [Ebrahimi and Bastani 2014]. The authors aimed to derive a mathematical formula for the prediction of these parameters. The properties evaluated in the experiments were microhardness, adhesion strength and scratch resistance. Microhardness was measured using a Leica VMHT MOT instrument on a microscopic scale, adhesion strength was done using the Defelsko pull-off test according to ASTM D4541 and scratch resistance was determined by using a pencil hardness tester with a tip radius of 0.5 mm. Results showed that the stock resin and Trimethylolpropanetriacrylate (TMPTA) concentrations had the most significant impact on the microhardness. Also, adhesion strength and scratch resistance of the films had a linear relationship with respect to all parameters, and mathematical models were successfully developed for every property studied.

Also in 2014, Maurya and Amin did a detailed study on the curing effects on modified urea formaldehyde resins [Maurya and Amin 2014]. Three main parameters were analyzed: temperature, concentration of the curing agent and layer thickness. Samples were cured in a closed-system thermal chamber. Five experiments were conducted in each test, changing the concentration of the curing agent to 5%, 10% and 15%, and modifying the layer thickness by 100 micrometers and 200 micrometers. The mole ratio of the resin was also modified. The temperature of the resin changed from 40°C to 80°C. Results showed that increasing the concentration of the curing agent and minimizing the layer thickness of the resin increased the rate of curing. Figure 2.16 shows a graph from one of the experiments, involving 5% concentration of the curing agent

and 200 micrometer layer thickness. For each of the five experiments, the mole ratio of the resin was modified in increasing sequence. The graph shown represents the curing time as a function of temperature of the resin.

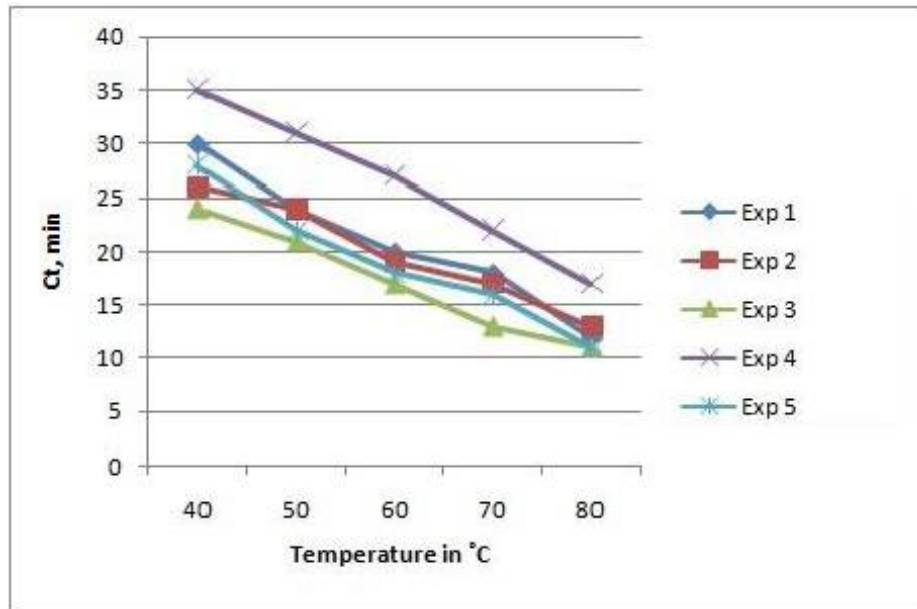


Figure 2.16: Curing Time vs. Temperature for 5% Resin Concentration and a 200 Micrometer Layer Thickness. [Maurya and Amin 2014]

Stereolithography research dates back to 1984, and only recently had become implemented in AM processes. Most of the research analyzes photopolymerization of a liquid resin substance and how it is affected by exposure energy, curing time, resin concentration, layer thickness, temperature, photoinitiator concentration, molecular weight and dynamic viscosity. Analyzing these studies gives an understanding towards the behavior and variable properties of photocurable materials. There is an absence of research in the specific area of AM processes, especially in the quality and dimensional accuracy of fabricated products.

## **3 Methodology**

### **3.1 INTRODUCTION**

A successful AM process must minimize all errors with the machine and its calibration and minimize them as much as possible. The design must be robust and reliable, the methods applied need to be consistent and practical, and the fabricated part as a result needs to be dimensionally accurate and have optimal surface quality. In order to modify the application of an AM process from layered to layerless (also known as continuous build), in which the machine does not cease its operation, the lift and retract sequence must be eliminated entirely. The layerless AM process should improve the quality of the part and also be faster in part production. There is limited knowledge and usage in industry for this process, and to better understand its behavior a new synchronization process is introduced. The concepts behind the SLA AM process are discussed, including the curing mechanism, machine design, machine calibration and the layerless fabrication process.

### 3.2 CURING MECHANISM

Before covering the machine design, it is important to understand the mechanism behind the curing functionality of the resin. The exact chemical structure of the G+ resin used is withheld from the public as a trade secret, however the Material Safety Data Sheet (MSDS) states that its composition contains greater than 60% of acrylate monomers. A monomer is a molecule and a chemical that is the primary ingredient in resin. Most commercial resins consist of up to three known kinds of monomers: acrylates, epoxies and vinyl ethers [Gibson et al. 2010]. All of the monomers contain oxygen, hydrogen and carbon atoms, however the chemical structure differs between each one, including the bonding between atoms. Figure 3.1 shows the chemical structure of the three different types of monomers used in commercial resins:

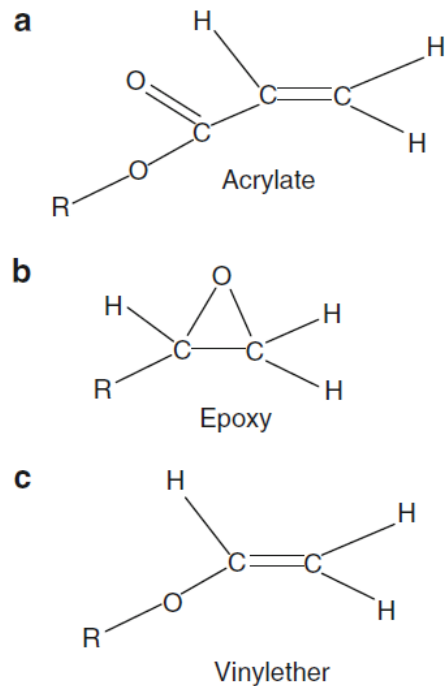


Figure 3.1: Chemical Structure of 3 Types of Monomers Used in Commercial Resins. [Gibson et al. 2010]

The other component present in all three of the structures is commonly known by the name “R-structure”. It contains a series of carbon-carbon double bonds. Generally, a resin has thousands of the same monomer in its composition. The process of linking several monomers to one another in generating a polymer chain is called “polymerization”. The process can be taken a step further by introducing a specific light source to trigger the same reaction in forming and linking a series of polymer chains. By introducing a light source of the required specification (depending on the resin), the R-structure carbon-carbon double bonds react, branch out from the polymer and attach to other R-structures belonging to different polymer chains. This process is called “cross-linking”.

The longer the chain of polymers becomes and the more cross-linking there is between polymer chains, the stronger the bonding strength of the polymers. The bonding eventually becomes so strong that the resin changes from a liquid state to a solid state. The technical term used to describe the process of changing the state of the resin from a liquid to a solid state is known as “photopolymerization”, however it is referred to as “curing” throughout the thesis to simplify the terminology. Figure 3.2 shows a step-by-step depiction of each phase during the polymer linking process.

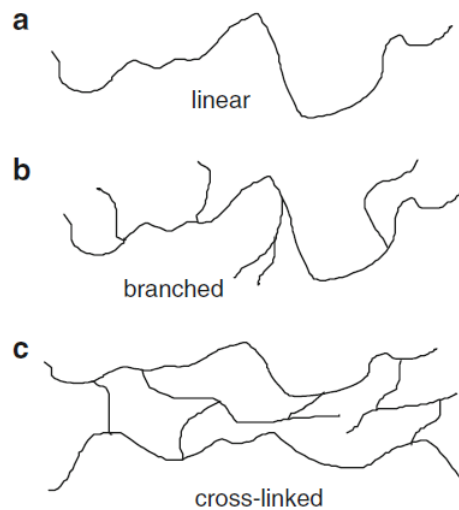


Figure 3.2: Curing Schematic. [Gibson et al. 2010]

Initially, the polymer chains are linear upon forming as a result of linking the monomers together (polymerization). Next, the light source causes the R-structures on the polymer chain to react and branch out. Finally, the branches from the R-structures of separate polymer chains attach to each other and become cross-linked. The cross-linking continues until the resin changes state from liquid to solid (curing).

The monomers used in the resin also have a significant role in curing. Each type of monomer has its advantages and disadvantages. Acrylates exhibit high photospeed, which means they react quickly to the light source and cure quicker. The drawback for acrylates is that there is a tendency to shrink, warp and curl. Epoxies are the opposite, generally taking a longer time to cure and are less likely to shrink, warp and curl. Usually a balance between acrylate and epoxy monomers is contained in commercial resins. Vinylether monomers exhibit very similar characteristics to epoxy monomers, however they are less effective and are not commonly found in commercial resins.

The only issue that is unanswered at this point is what causes the reaction to occur with the R-structures when subject to the light source. This is achieved through a specific type of catalyst used in the resin, called a “photoinitiator”. The role of the photoinitiator is to convert physical energy of the light into chemical energy in the form of reactive intermediates, which permit the reaction to occur. The chemicals used as photoinitiators, the chemical structures and chemical reactions are very complicated and are out of the scope of the thesis.

### 3.3 MACHINE DESIGN

A schematic drawing of the machine is shown below in Figure 3.3, identifying all major components and their position in the system. The preliminary engineering design is provided in Appendix A. Some of the dimensions were modified later to accommodate a larger screen.

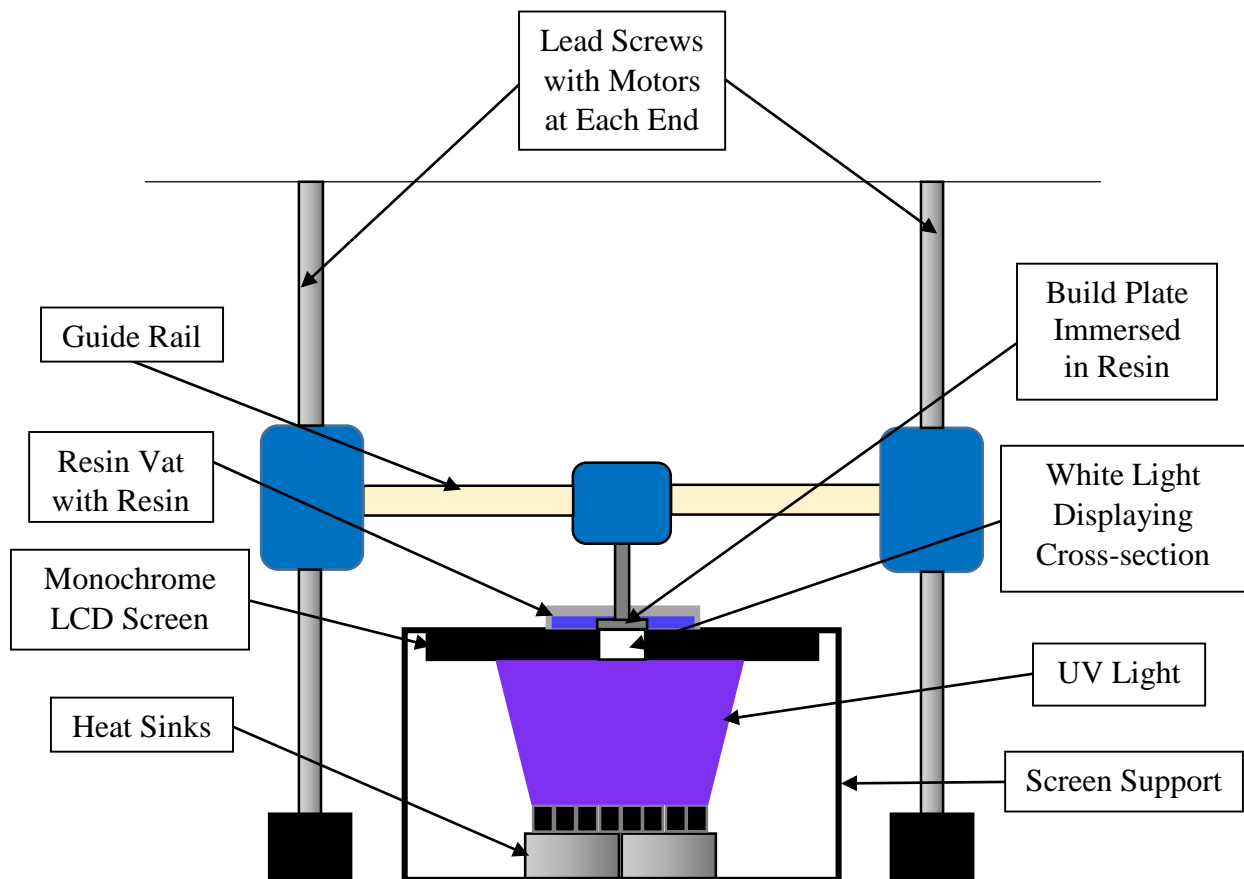


Figure 3.3: Schematic of SLA Machine Design.

The size of the SLA system, once constructed, is approximately a 500 mm cubic design and is shown in Figure 3.4. The 75 mm square build plate is superglued to a bolt fitted through a slot in the center piece, located on the horizontal double rail that is free to move along the rails. The bolt has two washers and two nuts in order to fasten the bolt to the center piece from both sides. Using the threaded lead screws, which are each attached to either side of the machine and to a stepper motor, the whole rail is permitted to travel in the vertical direction. A limit switch prevents any further movement which could cause damage to the components. Sitting on top of the LCD screen (black rectangular panel in the center of the machine) is the vat, which has been constructed by hand using only acrylic glass, acrylic glue, a coffee container and a nonstick material called Sylgard 184 silicone elastomer. This holds the photocurable resin used for part fabrication.

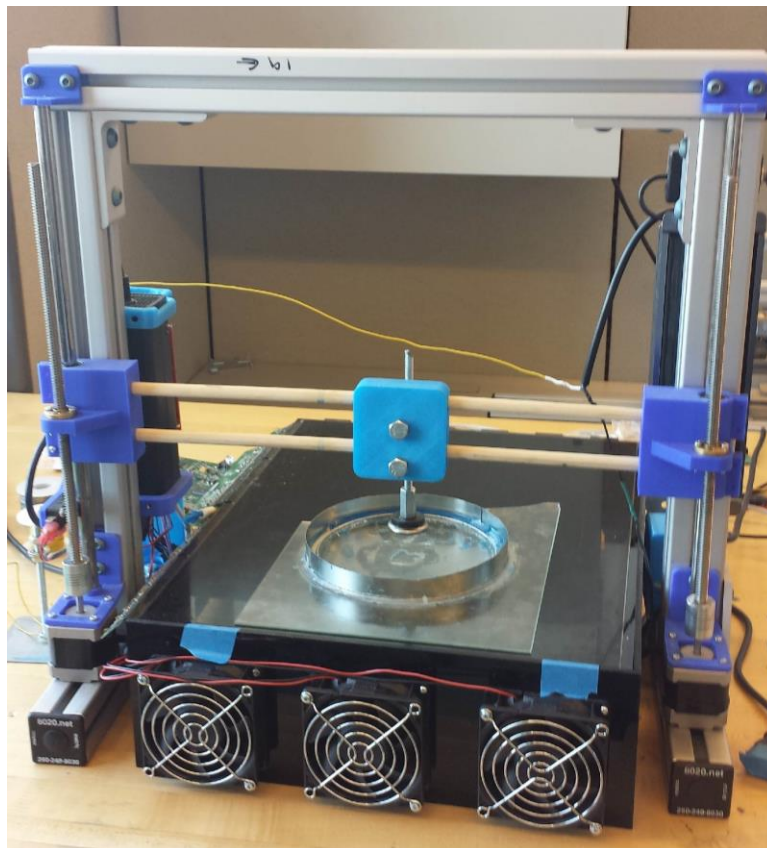


Figure 3.4: Full-scale View of SLA Machine.

The frame structure of the machine is made of 8020 Aluminum, which is light and simple to work with. The dark blue components, consisting of mostly supports, hangers and guide pieces, are made of blue ABS (Acrylonitrile Butadiene Styrene) plastic. The light-blue center piece holding the build plate is made of PLA (Polylactic Acid) plastic. Both of these parts were fabricated using a BFB 3D Touch FDM 3D printer. The many fasteners used throughout the machine are made of steel, the heat sinks are made of aluminum, and the LCD screen holder (large black rectangle) is made from acrylic sheets.

The electronics used in the machine are considerably delicate and potentially dangerous. Precautions must be taken during and after installation of the components, such as knowing the limits of the electrical equipment and the safety measures required during handling. The first component to discuss is the most major aspect of the process, which is the light source. It is a Printed Circuit Board (PCB) containing 80 soldered near-UV LEDs rated at 405 nm and each with 3 Watts of power at full strength. It was necessary to select the lights based on the technical documentation of the Sub G+ resin. A graph of resin absorbancy as a function of light wavelength is seen in Figure 3.5, obtained from the MakerJuice website:

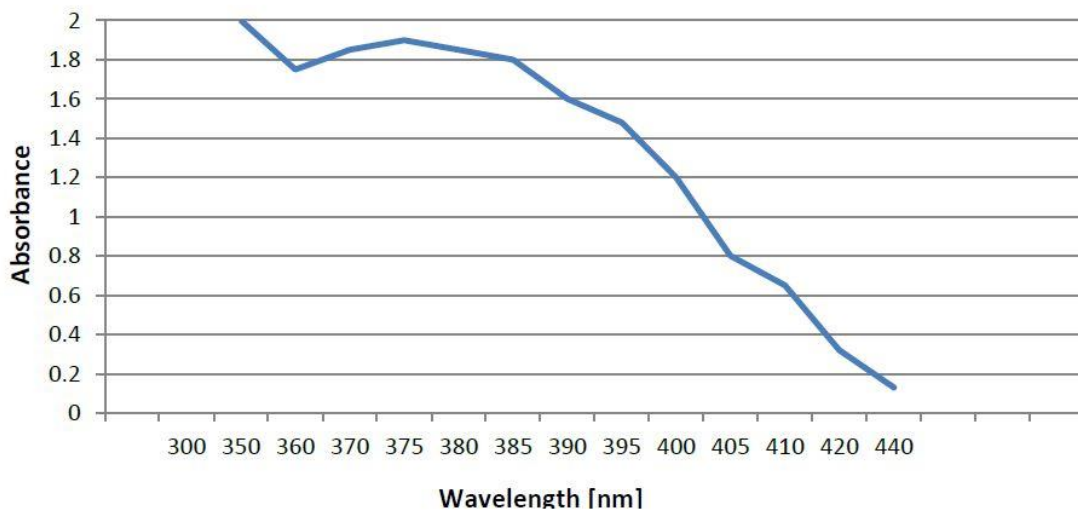


Figure 3.5: G+ Absorbance Ratio as a Function of Exposed Light Wavelength.

The technical data sheet is provided in Appendix B. Absorbance is the ratio of incident to transmitted power of light and is measured in Absorbance Units (AU). An additional factor that affected the selection of the light source was the LCD screen, which would only permit light with a wavelength of 400 nm or greater. Past research has indicated that a recommended value of AU was in between 0.8 and 1.0, in which the selected light of 405 nm gives 0.8 AU.

The PCB was shipped from a supplier (Nick Martin) on the Build Your Own SLA forum. The lights are arranged in an offset pattern to optimize the exposure of the lights. The plate itself is made of aluminum and is connected in series-parallel; every light in a row is connected in series and each row of lights is connected in parallel. The LEDs are covered with 120 degree lenses so there is proper dispersion of the light source. The positive terminal on the bottom-left and the negative terminal on the bottom-right are connected to a power supply, regulated down to an acceptable voltage and current that will not damage the board. The values are 32-36 Volts and 6.6 Amps respectively. To exercise caution and avoid inaccurate readings, the amperage is set to be slightly less than its maximum capacity. The PCB is placed on top of the aluminum heat sinks for better heat dissipation and the lights are designed to have 2 inches of spacing under the LCD panel. This was the optimal separation distance as determined by experiments conducted by the circuit board supplier.

The power supply is the next electrical component to discuss, which provides 12 Volts of Direct Current (DC), and is rated for 130 Watts of power and 19 Amps of current. It is used in conjunction with several electronics, including an LED driver. The driver uses a potentiometer to regulate the voltage and current down to an acceptable level for the PCB as mentioned before, and the Arduino Mega 2560 microcontroller / RAMPS v1.4 board assembly, which is necessary to control the machine with the software and the firmware

The Arduino microcontroller is essentially the brain of the machine, and must communicate with all of the major electrical components. It does this digitally through the use of firmware, which is a language of code that is programmed into its memory. The components are electrically connected to the RAMPS board using conductors, most importantly the z-axis control of the two NEMA 17 stepper motors and the fans required for cooling of the LED PCB and the LCD screen. The lights are controlled by a relay.

The LCD screen, used as the mask for the image of the AM fabricated shape, is a Barco monochrome MFGD 3420 model. Initially an iPad3 full color LCD screen was used but it was removed and replaced. The monochrome screen is preferred because it has a higher pixel density (more accurate builds) and it allows a greater quantity of light penetration through it than the iPad3, approximately 5 times as much power is permitted. The image is transferred onto the monochrome screen from a laptop through an LCD Adapter via an HDMI slot in the laptop. Three 40 mm fans are screwed into the front of the acrylic LCD screen holder in order to keep the screen cool from prolonged exposure of the lights. The holder is measured 340 mm wide by 450 mm long by 115 mm high and it is open at the back for improved cooling. The holder contains the two heat sinks and the UV LED PCB and is open on top with a thin trim to allow the LCD panel to sit and for UV light to pass freely through the screen.

### **3.4 MACHINE CALIBRATION**

Before printing, it was necessary to ensure the machine settings were optimal for the process. These settings were applied using the controlled software. Machine calibration was done with reference to a Vernier caliper and Coordinate-Measuring Machine (CMM) for measurements,

using the software, manual adjustment of machine components, and through several experiments. The experiments were conducted in order to understand what machine settings are optimal when manufacturing parts. Enclosed rings are printed by varying the internal diameter and external diameter to see how the resin expansion affects the dimensional accuracy of parts during the curing process. After this experiment, a more comprehensive shape is analyzed during the curing process, in which the exposure parameters exposure time, delay time and light intensity are varied. The optimal exposure parameters are selected from the sample that gives the highest dimensional accuracy. Finally, the last experiment validates the selected exposure parameters by printing larger 3D parts. A Rook is constructed at three different sizes and an AngleCube is also constructed.

### **3.4.1 Controlling Software**

To do proper 3D builds, software with manual settings is needed to run on a machine. The software is a very efficient, user-friendly, open-source type of software that is used to build 3D shapes using an SLA machine. There are four main features in this program, which can be switched between: 3D View, Slice View, Control, and Configure. The menu at the top of the interface shows eight different icons, which are seen in every feature. From left to right, these are Open File, Save File, Connect Machine, Disconnect Machine, Slice Model, Start/Resume Process, Pause Process, and Stop Process. Files consisting of stl, obj, 3ds, or amf extensions can be opened. The software also allows opening scene format files (cws extension), which is what all files will save as. A scene file contains all options saved in the program for printing. The graphic portion of the first screen, 3D View, shows the full model that is going to be fabricated.

The gear that is visible on the screen at the top-right corner brings up options for the object, involving translating and transforming the object. “Scene” is used for showing the active scene

file in the software. Scene files can be added and deleted from the list. “Object Info” will show properties of the model once the model has been sliced, including volume, cost and size. “Move” will move the build location of the cross-section on the LCD screen. The model has to be re-sliced each time this is done, or it will not save the changes. “Mirror” will reflect the model about a plane, and is very useful for building several models at once. “Scale” will make the part larger or smaller, either as a whole or about the individual axes. The scaling is done on a percent-size basis. “Rotate” will rotate the object about any of the X, Y or Z axes, specified in degrees. “View Options” change the way the model looks on the graphical interface. Just under the gear mentioned before there are two icons, one looking like a house and another like a square grid. These are “Home View” buttons, in which the upper one will take the model back to the default front view and the bottom one will take the model back to the default top view. The plus sign near the top-left corner of the graphic interface represents the addition of support material, during the fabrication of more complicated shapes.

The next screen, “Slice View”, contains the cross-section shown in white through all layers of printing on the SLA machine. There are two options to switch between, which are “Slice View” and “G-Code View”. The G-Code view simply shows the G-Code being run during the build process. Manual G-Code can also be inserted here, which will be used later in the synchronization algorithm. By switching between these two options, it can be observed what exactly is happening during the build process and when it is happening. Figure 3.6 shows a view of the mask, which is a cross-section of the 3D shape to be displayed on the monochrome monitor in the fabrication process. The cross-section is displayed in white light and the surrounding background is black, since black colors will absorb light rather than permit it through.

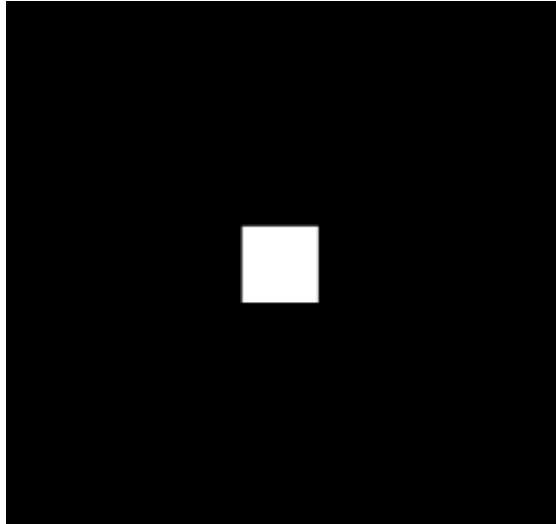


Figure 3.6: Software View of Mask.

The next main feature, “Control” contains the manual manipulation options of the machine. The “Z Axis” control contains several clickable buttons that affect the vertical movement of the build plate by accessing the stepper motors. The top button signifies the home position, in which the build plate will move to its lowest height, in which a limit switch will prevent the plate from going any lower. This is a safety mechanism used to prevent any damage to the vat, screen or machine. All other buttons will move the platform a specified distance up or down, for values of 0.1, 1, 10 or 50 millimetres. Just below the Z Axis control is the “Manual G-Code” control switch, which when turned on will bring up the “Manual G-Code Commands” on the top-right of the interface. The only commands used to operate the machine are M106 S255 or M107, which turns the UV lights on or off respectively and M42 P10 S255 or M42 P10 S0, which turns the fans on or off respectively for required cooling of the electrical components.

The last main feature in the software, “Configure” also comes in two different options. The machine and the slicing profile can both be configured. The “Build Size” (in millimetres)

represents the size of the build plate being used during the printing process. This will tell the user whether the model is within the allowable size or not. The “Machine Connection” specifies the port that the machine controller is connected to. This can be found a number of different ways. The baud rate (speed) and number of bits also need to be specified. The LCD screen parameters can be configured as well. The available display is the laptop running the controlling software and the configured display is the monochrome LCD screen used as the mask, in which the vat sits on top of. The display needs to be configured since the resolution is not the same and the size of the model must be consistent when the image is transferred from the laptop to the LCD screen. The “Projector Control” contains port information for the display mechanism, similar to what was specified before in the machine connection. The port numbers will always be different from one another. The setup being used has one serial connection for the LCD adapter, which has to be specified, but the mask connection is done through the adapter, and therefore does not need to be specified. Under “Machine Controls”, there are several options that can be checked on and off. The only options that need to be selected are “Z Axis” and “Manual G-Code” for the experiments. These options show up under the Control feature as mentioned before.

The other configuration option, “Configure Slicing Profile” has two tabs, “Options” and “G-Code”. Each configuration made can be saved and used later to save time. Instead of looking at each and every parameter to tell which profile is the one desired, “Notes” can be added to let the user know all about the settings in a few words. The “Exposure Settings” contain the most important parameters in the experiments, slice thickness, which is the same as layer thickness in conventional FDM processes, exposure time, which tells the machine how long to cure the resin with the UV lights for in milliseconds, bottom exposure, which can be a different value of exposure time in milliseconds that is used to cure the first few layers. This is sometimes done to promote

adhesion, but it is not always required. For consistency in experimentation, this parameter is kept at the same value of the exposure time and no bottom layers are used. The “Lift and Sequence” parameters contain the lift distance, which is how much the build platform is lifted between layer curing, lift speed, how fast the build platform is raised, and retract speed, how fast the platform returns to the next layer to be cured. The only precaution to take in setting these values is that they cannot be too large, because this could harm the machine and/or the quality of the model being fabricated.

Finally, the “G-Code” interface allows the user to input their own G-Code at the start, before the slice phase, during the lift phase, or at the end of the program. These codes can also be saved and loaded for future use. Examples of operations that are used are turning the motors on at the start, turning the lights on before a slice (during a cure), turning the lights off during the lifting phase, or turning everything off once the print has been completed.

### **3.4.2 Manual Calibration**

Minimizing all possible errors before testing on an AM fabrication process is required. There are some calibration procedures that involve careful inspection and manual procedures, such as setting a level build plate, centering the build plate with the image, adjusting the home position of the build plate and finally re-sizing the build platform. Following these steps will result in a more consistent build every time the machine is operated.

Leveling the build plate is a potentially challenging task and is done by maneuvering the bolt (attached to the build plate) and tightening the nuts when the optimal orientation has been determined. A counter-weight is placed on the center piece to get the rest of the needed movement

of the build plate. Centering the build plate with the cross-section on the screen is a simple process because the center piece, which holds the build plate, is free to translate along the rails (Y-axis). The perpendicular component is moved by using the software to reposition the image along the X-axis. Adjusting the home position of the build plate is also a simple task, but a specific order of steps must be followed. First the bolt is taken out of the center piece and the home button is selected on the controlling software. The bolt removal is a precautionary step to ensure that nothing on the machine, mainly the screen, is damaged in case the platform moves too low and applies a heavy pressure on it. Once the home position is located, the bolt is placed back into its appropriate slot on the center piece and it is re-tightened using the nuts on either side of the center piece. In case the image on the LCD screen measures differently than the model dimensions, the software can be used to re-size the shape indirectly by re-sizing the build platform. The measurements of the cross-section on the screen as well as the model dimensions need to be known in order to modify this properly. Prints are always started with the build plate lightly touching the non-stick elastomer surface of the resin container and may not ever be placed above the metal inner rim. Finally, the resin is added (enough to cover the base of the build plate) and a build can be executed.

### **3.4.3 Expansion of Enclosed and External Dimensions**

Now that the machine is manually calibrated, the next step involves running several tests to select and validate the exposure parameters of the machine. One experiment includes the printing of enclosed parts (rings) and developing relationships between external dimensions, enclosed dimensions and dimensional accuracy. This is shown using a graphical method. The purpose of the experiment is to see how the resin expands externally and internally during curing

and how much this expansion affects dimensional accuracy of the manufactured parts. Each value recorded is an average of five measurements done using a Vernier caliper and a CMM to verify.

For the first test, rings are printed that vary between a 4 mm to 12 mm nominal internal diameter (based on a CAD file) with a constant outer diameter of 15 mm. Similarly, another set of rings are fabricated that vary between a 16 mm to 20 mm outer diameter with a constant inner diameter of 10 mm. The results of the prints are shown in Figure 3.7. All of the samples are exposed to the light for 10 seconds.

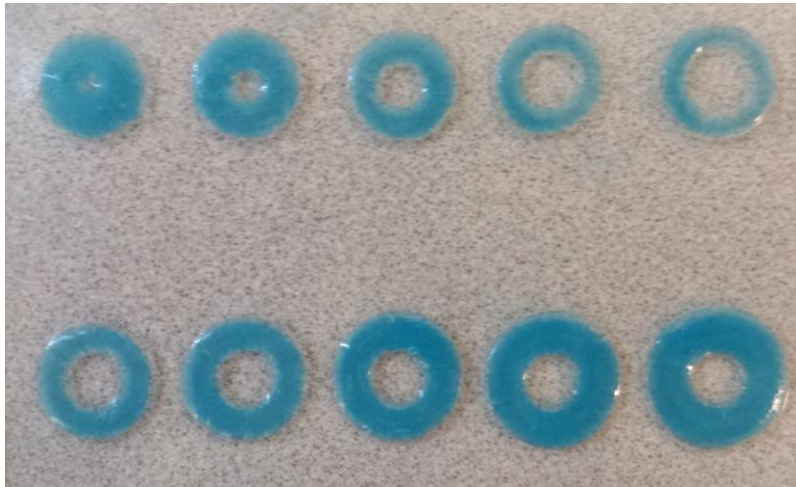


Figure 3.7: Ring Experiments (Internal and External Variation).

The top row of rings in Figure 3.7 show internal diameter variation with a constant external diameter, whereas the bottom row of rings show outer diameter variation with a constant internal diameter. The measurements of the outer parameter variation experiments are shown in Table 3.1. The percentages of accuracy of the variable dimensions are shown in the last column of the table.

Table 3.1: External Ring Experiment Measurements.

<b>Dimensions</b>	<b>D outer nominal (mm)</b>	<b>D outer (mm)</b>	<b>D outer % error</b>	<b>D inner (mm)</b>	<b>D inner % error</b>
<b>10 mm in, 16 mm out</b>	16	16.54	3.4	7.61	-23.9
<b>10 mm in, 17 mm out</b>	17	17.62	3.6	7.84	-21.6
<b>10 mm in, 18 mm out</b>	18	18.45	2.5	7.76	-22.4
<b>10 mm in, 19 mm out</b>	19	19.61	3.2	7.93	-20.7
<b>10 mm in, 20 mm out</b>	20	20.5	2.5	8.02	-19.8

The measurements of the inner parameter variation experiments are shown in Table 3.2.

Table 3.2: Internal Ring Experiment Measurements.

<b>Dimensions</b>	<b>D inner nominal (mm)</b>	<b>D inner (mm)</b>	<b>D inner % error</b>	<b>D outer (mm)</b>	<b>D outer % error</b>
<b>4 mm in, 15 mm out</b>	4	1.14	-71.5	16.26	8.4
<b>6 mm in, 15 mm out</b>	6	2.45	-59.2	15.77	5.1
<b>8 mm in, 15 mm out</b>	8	5.09	-36.4	16.12	7.5
<b>10 mm in, 15 mm out</b>	10	7.27	-27.3	15.94	6.3
<b>12 mm in, 15 mm out</b>	12	10	-16.7	15.78	5.2

There are three observations that can be made from these measurements. Firstly, the outer diameter is always more accurate than the inner diameter. Second, the outer diameter expands outwards while the inner diameter shrinks in size. Finally, the inner diameter gets more accurate

the larger its size. The reason the outer diameter is more accurate than the inner diameter is because the inner diameter is measured in an enclosed space, where the heat from the light cannot dissipate. For the external diameter, the heat can dissipate outwards in a variety of directions, resulting in a cooler temperature and less resin expansion. This can also explain the reason behind the expansion of the outer diameter and the shrinking of the internal diameter. Larger inner diameters have a larger enclosed space, resulting in more space for the heat to be dissipated and a cooler surrounding edge, which will cause less excess curing. A graphical representation of the outer and inner diameter variation experiments can be seen in Figure 3.8 and Figure 3.9 respectively.

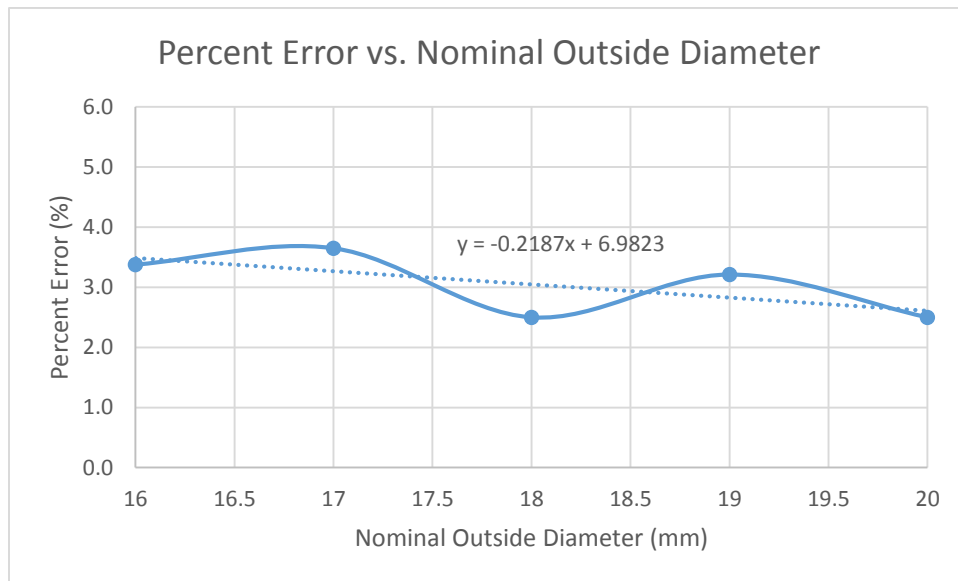


Figure 3.8: External Ring Dimensional Error vs. Nominal Size.

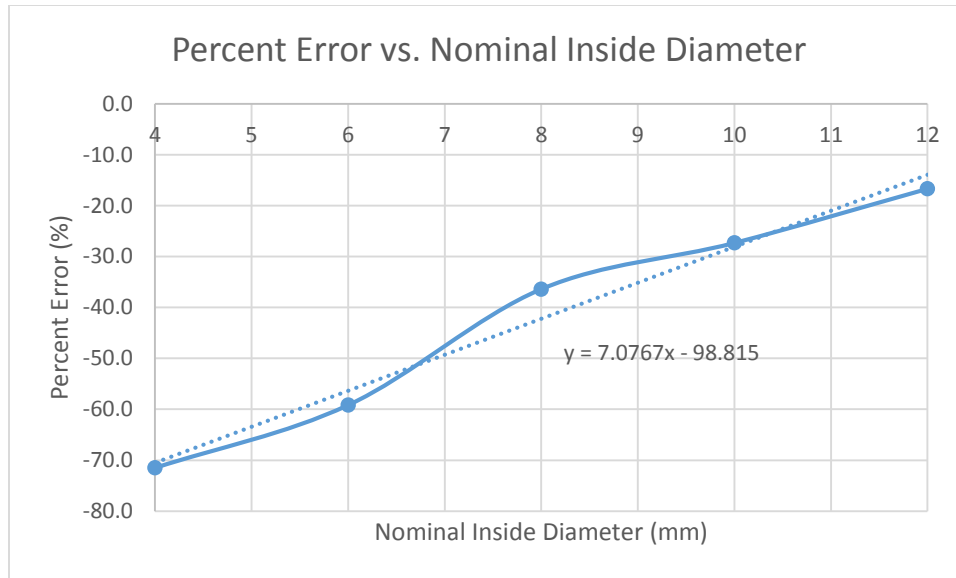


Figure 3.9: Internal Ring Dimensional Error vs. Nominal Size.

From the look of the graph in Figure 3.9, there exists a minimum interior diameter that will theoretically result in near-perfect accuracy. This theory implies that the expansion of the resin is linear. The size of the minimum inner diameter that gives this theoretical result can be calculated from the trend line as 14 mm. Consequently, the conclusion drawn from the experiment is that larger parts will generally be more dimensionally accurate than the same part printed at a smaller scale. Also, enclosed features are more sensitive to dimensional changes than external features. This will be validated in a visual experiment later.

### 3.4.4 Optimal Exposure Parameter Selection

The optimal exposure parameters consist of the exposure time, the delay time and the light intensity. The delay time is a layered manufacturing term only, as it involves the total time after curing a layer that spans disabling the light source, lifting the build plate and retracting back down

to a height that is one layer up from the previous layer that was cured. It is important to give the machine enough cooling time between the curing of each layer so the part quality will not be jeopardized. To find the optimal parameters for the machine, several samples of the same shape were printed with different specifications. The exposure times used were 4,5,6,7 and 10 seconds. Based on experience with the machine, 4 seconds is the minimum time required for a cross-section to cure completely, and 7 seconds is the maximum time allowed for the dimensional accuracy of a part to be preserved. The 10-second samples were provided to demonstrate significance of each test criteria. Measurements are taken using a digital Vernier caliper, with an average of 5 measurements being recorded as the result for each dimensional feature. The default delay time was 13.6 seconds, samples were printed for each of the 5 different exposure times for the default delay and double delay, a total of 10 parts. The D parameter widths recorded for the most consistent samples at 7 seconds were still unacceptable. Based on these results, two additional parts were printed for a quadruple delay time, one at 10 seconds and one at 6 seconds, to determine which sample gave more consistent and accurate results. If the 10-second sample gave more accurate results, more samples would be required between 7 second and 10 second exposure time. However, the 6 second sample gave better accuracy than both of the previously selected samples. The measurements were still slightly larger, but within an acceptable error. Since it is known that a part expands more the longer it is cured, this sample was selected as optimal. Three different samples were printed including the maximum, middle and minimum exposure times for half of the light intensity with normal delay time to see its significance on a part's dimensional accuracy and quality. The comprehensive part tested in all of the above cases is demonstrated in Figure 3.10 below.

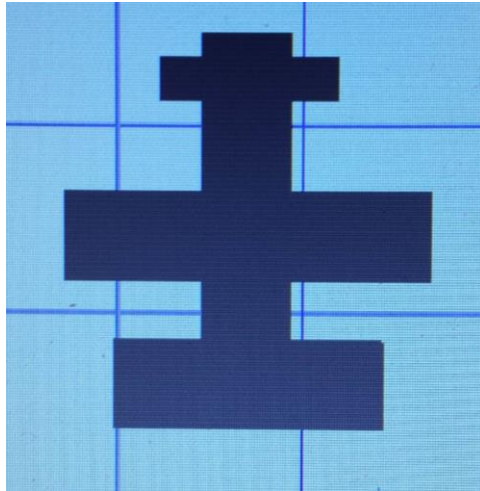


Figure 3.10: Comprehensive Part.

The results of the printed samples are shown in Figure 3.11. The measurements based on all of the printed samples are shown in Table 3.3.

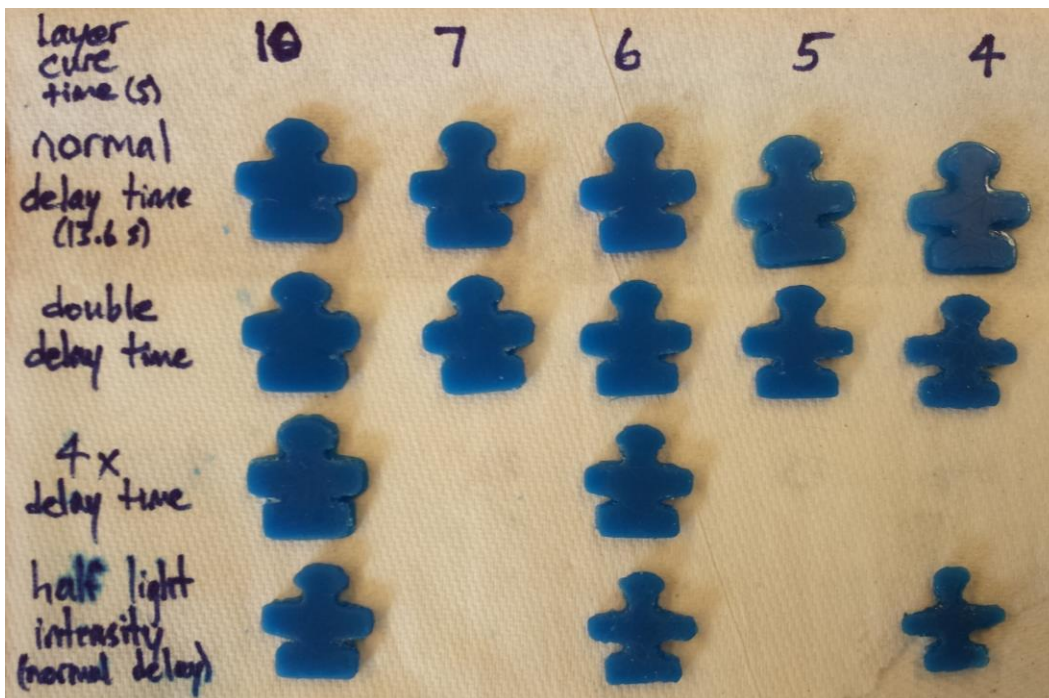


Figure 3.11: Comprehensive Part Experimental Samples.

Table 3.3: Measurements of Comprehensive Samples.

Layer Cure Time (s)	Part Dimensions of Varying Delay Time and Light Intensity (mm) (shown in width x height x thickness format)					Comprehensive Shape Dimension Legend
	10	7	6	5	4	
Normal Delay (13 s)	A = 10.68 x 3.92 x 2.68	A = 10.06 x 3.39 x 2.75	A = 10.30 x 3.55 x 2.90	A = 8.92 x 3.23 x 2.86	A = 8.60 x 2.79 x 2.07	A = Top Horizontal (10 x 2.5 mm x 2.5)
	B = 21.01 x 6.11 x 2.68	B = 20.41 x 5.90 x 2.75	B = 20.33 x 5.70 x 2.90	B = 18.96 x 4.56 x 2.86	B = 18.75 x 4.50 x 2.07	
	C = 15.78 x 6.49 x 2.68	C = 15.28 x 5.71 x 2.75	C = 15.18 x 5.99 x 2.90	C = 13.87 x 5.16 x 2.86	C = 13.30 x 4.74 x 2.07	
	D = 8.35 x 21.65 x 2.68	D = 7.01 x 21.91 x 2.75	D = 7.21 x 22.14 x 2.90	D = 5.12 x 21.21 x 2.86	D = 4.86 x 20.93 x 2.07	
Double Delay	A = 10.28 x 2.86 x 2.99	A = 9.73 x 2.50 x 3.10	A = 9.06 x 2.49 x 2.75	A = 8.42 x 2.65 x 2.99	A = 8.02 x 2.25 x 2.68	B = Mid Horizontal (20 x 5 x 2.5 mm)
	B = 20.45 x 6.10 x 2.99	B = 19.88 x 5.63 x 3.10	B = 19.59 x 5.40 x 2.75	B = 18.91 x 5.02 x 2.99	B = 18.67 x 4.67 x 2.68	
	C = 15.60 x 6.23 x 2.99	C = 14.62 x 5.67 x 3.10	C = 14.46 x 5.14 x 2.75	C = 13.81 x 5.04 x 2.99	C = 13.28 x 4.60 x 2.68	
	D = 7.30 x 21.03 x 2.99	D = 7.33 x 20.50 x 3.10	D = 6.56 x 20.28 x 2.75	D = 5.85 x 19.80 x 2.99	D = 5.46 x 19.84 x 2.68	
Quadruple Delay	A = 10.00 x 2.56 x 2.99		A = 8.72 x 2.53 x 3.00			C = Bot Horizontal (15 x 5 x 2.5 mm)
	B = 20.28 x 6.00 x 2.99		B = 19.35 x 5.17 x 3.00			
	C = 15.27 x 5.48 x 2.99		C = 14.82 x 5.42 x 3.00			
	D = 6.50 x 21.03 x 2.99		D = 5.41 x 20.31 x 3.00			
Half Light Intensity	A = 9.31 x 3.06 x 2.95		A = 8.24 x 2.11 x 2.92		A = 6.25 x 1.99 x 2.70	D = Vertical (5 x 20 x 2.5 mm)
	B = 19.60 x 5.35 x 2.95		B = 19.24 x 4.14 x 2.92		B = 17.90 x 3.76 x 2.70	
	C = 14.68 x 5.65 x 2.95		C = 13.51 x 4.55 x 2.92		C = 11.70 x 3.96 x 2.70	
	D = 6.70 x 20.34 x 2.95		D = 5.33 x 19.83 x 2.92		D = 4.44 x 18.38 x 2.70	

From Table 3.3, the best result for each category was picked and all of the choices were placed in order of dimensional consistency. To summarize, the most consistent result was the sample printed for an exposure time of 6 seconds, with quadruple delay time and full power light intensity. These are the optimal curing parameters used for the rest of the remaining experiments. At half of the light intensity, the variance of dimensions is much larger than any of the other samples, and therefore the light intensity is a more significant exposure parameter than the delay time. Parts cured at a more powerful light intensity will take less time to complete with all other factors being equal, however the delay time must be multiplied by a factor of four times the original value in order to be more consistent than the sample with a halved light intensity. The sample at 10 seconds gave the best result, however all three results were out of acceptable error. Since the objective of the research is dimensional accuracy, the total time of the manufacturing process does not play a significant role and therefore the sample requiring a quadruple delay time is selected for all future experiments using a layered manufacturing process.

To validate the previous theory that parts are more accurate when built at a larger scale, one more sample is printed. Shown in Figure 3.12, the part is scaled to be three times its original size. Features that could not be seen on the smaller-scaled samples now show up on the larger sample and thus is visible proof.



Figure 3.12: Comprehensive Sample, Scaled 3:1.

### 3.4.5 Complex 3D Parts (Rook and AngleCube)

As found in the previous experiment, the optimal parameter setup of a 6-second layer cure time, a quadruple delay time (~55 seconds) and full light intensity is used to print the following parts. These parts contain more detailed features than any shape experimented with thus far, and present a final two parameters that require experimentation to find. These parameters are the lift speed (or the feed rate) and the lift height (between layers). Initially both of the parameters were set too high. They are more significant characteristics for longer build processes, where endurance of the machine becomes an important factor to consider. The rook to be printed is shown in Figure 3.13 (a) as an STL file. The result of a full-scale SLA layered build is shown in Figure 3.13 (b).

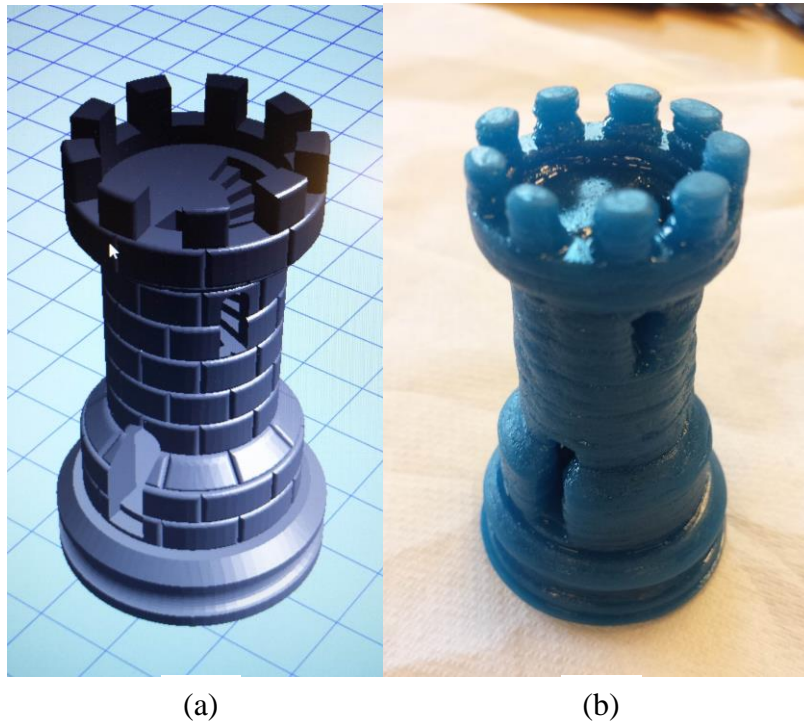


Figure 3.13: (a) Rook STL file, and (b) Rook SLA print.

An example of a rook part attempted to be printed with a feed rate that is too high is shown in Figure 3.14 (a). The other sample in Figure 3.14 (b) shows a rook attempted to be printed with a feed rate that is too low. Once the part is constructed enough such that it becomes heavy, a high feed rate will have enough force to pull it apart from any further cured layers, and a low feed rate will not have the strength to pull the part away from the bed at all while curing, which is why excess resin is apparent.

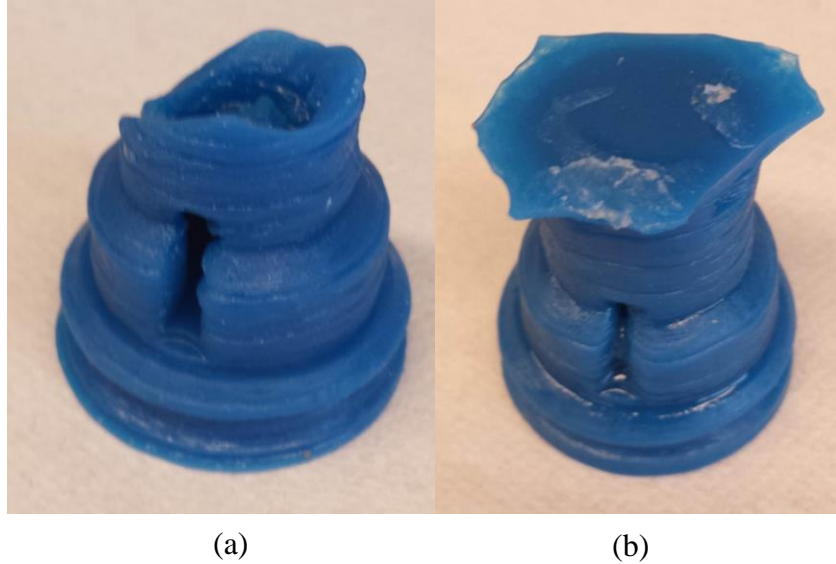


Figure 3.14: Rook Build Attempts with Feed Rates: (a) Too High, and (b) Too Low.

A feed rate is selected to be slow enough to retain its shape throughout the build and the lift height is selected such that the part never leaves the resin during its lift sequence. Ensuring the part is coated in resin until the process is completed encourages layer bonding to be much easier.

The other part that is fabricated in order to conduct further analysis is an AngleCube, which is shown in Figure 3.15 (a). The result of the full-scale SLA build shown in Figure 3.15 (b). The layers on the angled surfaces are apparent and the desire is to eliminate these layers completely. This will result in better surface quality and most likely higher dimensional accuracy. It can be seen that all of the sharp edges on the SLA build of the AngleCube are rounded off. This is one limitation of the machine that cannot be avoided.

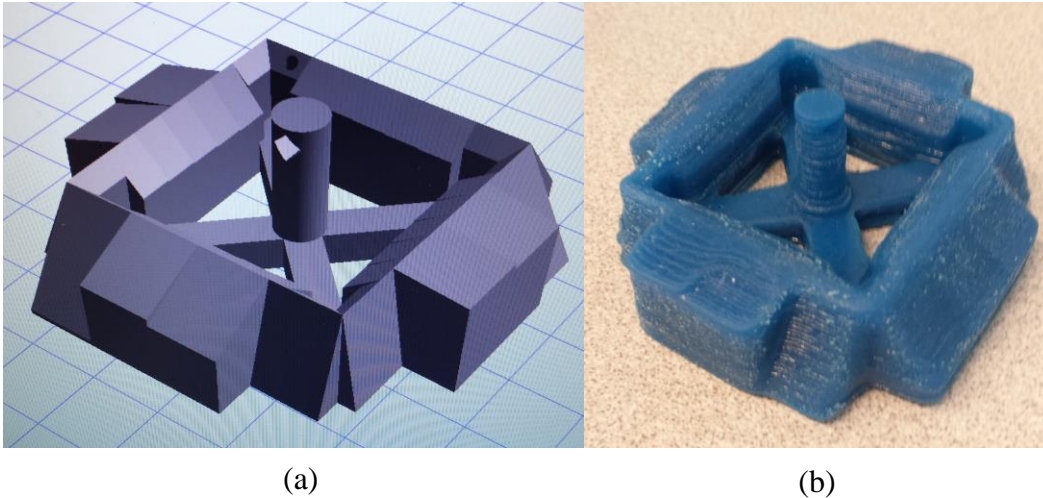


Figure 3.15: AngleCube: (a) STL file, and (b) SLA print.

### 3.5 LAYERLESS FABRICATION PROCESS

The developed layerless manufacturing SLA machine is conducted by completing two processes:

*Slicing Process* - a software algorithm that produces information of the cross-sections of a 3D model from a Stereolithography file (STL), and

*Dynamic Curing Process* – developing a G-code instructional program for the machine to synchronize transfer of the slicing data with the elevation of the machine platform considering the optimum curing parameters.

The layerless AM process is achieved by synchronizing a video from the STL slicing program with manually generated G-Code used to control the curing process. The video is a dynamic representation of the cross-sectional views of the desired 3D model created by the CAD system.

The rate of displaying the cross-sectional views is controlled by uses a very important variable called the frame rate, which determines the video's length. The units are frames per second, where

one frame means one cross-sectional view. The length of the video must be equal to the duration of the curing process, however certain specific parameters are necessary to obtain this relationship such as the minimum allowable machine feed rate, the optimal machine feed rate and the desired video frame rate.

### **3.5.1 STL Video Generation**

The video is the baseline of the methodology for layerless manufacturing. The code used to generate the cross-section of the part and display each one in a windowed video file is provided in Appendix C. There are two main scripts used. The first main file is an STL reader and slicer, which locates all of the faces and vertices of an STL file, and determines which vertices are connected using a line to construct the edge belonging to its respective triangle (face). The format of an STL file contains separate blocks associated with each triangle in the 3D model. These blocks consist of a normal vector indicating the triangle orientation and point coordinates associated with the vertices of the triangles. There are two types of STL files, which are text and binary. Text STL files begin with one line stating the name of the solid to be sliced. This is a loop that must be terminated at the end of the file. Inside the loop is a number of blocks equal to the number of faces (triangles). The format of a text STL file is explained through pseudo-code. The file ends after the information of the last triangle is read:

```

solid name
  facet1 normal ni nj nk
    outer loop
      vertex1 v1x v1y v1z
      vertex2 v2x v2y v2z
      vertex3 v3x v3y v3z
    endloop
  endfacet1

  facet2 normal ni nj nk
    outer loop
      vertex1 v1x v1y v1z
      vertex2 v2x v2y v2z
      vertex3 v3x v3y v3z
    endloop
  endfacet2
  .
  .
  .
endsolid name

```

each  $n$  or  $v$  contains a floating-point number in sign-exponent format and each  $v$  must be non-negative. Binary STL files have a similar format to text STL files, but are smaller in size and are generally preferred to text files for this reason. A typical binary file starts with an 80-character header. After the header is a 4-byte unsigned integer declaring the number of triangles in the STL file. Then, all of the blocks containing the normal vector and vertex information of each triangle, which are described by twelve 32-bit floating-point numbers. Three are assigned to the normal vectors and three are assigned to each vertex. At the end of each block, a 2-byte short unsigned integer describing the attribute byte count. The file terminates in the same way a text file does. The format of a binary STL file is explained through pseudo-code:

*UINT8[80] – header / title of STL file*  
*UINT32 – number of triangles in STL file*

*for each triangle*  
    *REAL32[3] – Normal vector 1*  
    *REAL32[3] – Vertex 1*  
    *REAL32[3] – Vertex 2*  
    *REAL32[3] – Vertex 3*  
    *UINT16 – Attribute byte count (usually 0)*  
    .  
    .  
    .  
*end*

The second main file is the video generation algorithm, which fills the corresponding triangles using a polygon filling method in order to construct the full STL model. Each layer of the model is displayed on a single figure and the number of figures required in the video file is calculated from the parameter layer thickness. The frame rate is specified, which determines the length of the video as a function of time. This is the most significant parameter in synchronizing the video with the build process.

An example of the AngleCube CAD 3D model is shown in Figure 3.16 with its STL representation. The part file from the CAD software is colored in blue and the STL representation is shown using brown lines across the CAD file's surface. Notice that each of the part's features is split up into triangles. The procedure of the STL reader and slicer algorithm is discussed here. Initially, the faces and vertices are obtained by accessing the STL file through the triangle block information and the slice height is specified. A loop searches through elevation from minimum to maximum value and separates the height of the part into layers identified by the slice height. For each of the slice height intervals, the triangles are associated to intersection points based on 3 different cases: points above, points below and points on the same plane as the current elevation

in the loop. All triangle edges are affiliated with exactly two different triangles. The purpose of this search is to check the orientation of the triangles and perform a check whether the triangle goes into the object or not. Triangles crossing into the shape are eliminated since all of the triangles must be oriented along the surface of the STL model. After this step is completed, all of the intersection points are sorted from minimum to maximum elevation. A check is performed on existing duplicate intersection points, which are deleted. A loop searches from the first to the last slice, locates all connected pairs and connects them using a line segment for each. The line information is stored in an array. The loop completes and the code is terminated.

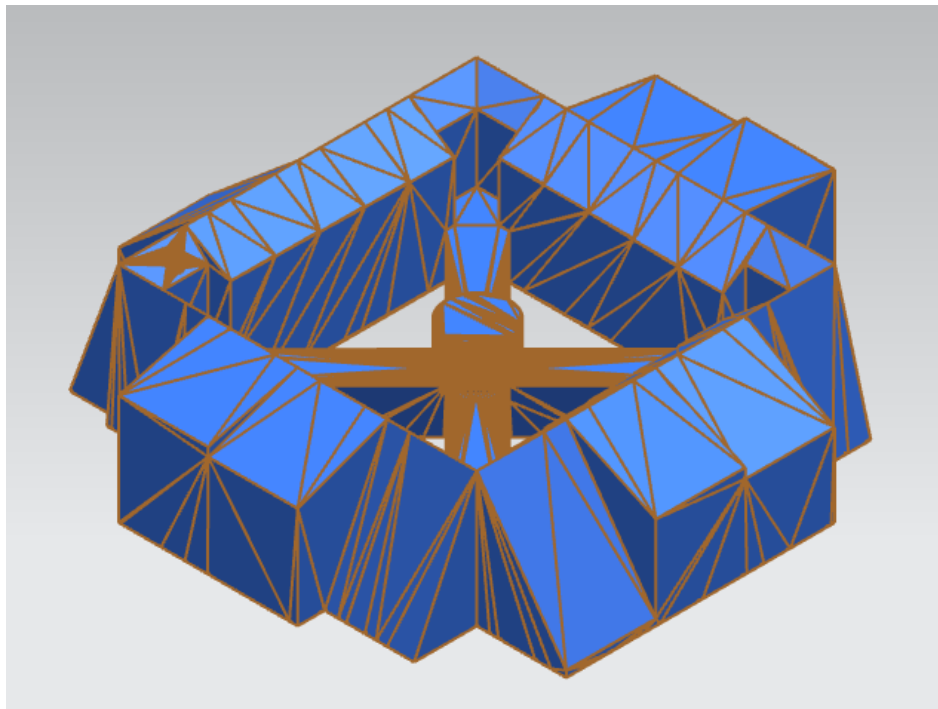


Figure 3.16: STL Representation of AngleCube CAD file.

### 3.5.2 Determination of Minimum Machine Feed Rate

The minimum machine feed rate can be determined by assigning a very small feed rate to the machine and operating for a specified lift height. The machine will be unable to work with the set feed rate, and therefore will regulate the setting to the minimum permitted speed of the motors. Once the elapsed time is obtained by the controlling software, the minimum feed rate allowed by the machine can be found using the following equation:

$$f_{min} = \frac{h_{lift}}{t_{print}} \quad (3.1)$$

where  $h_{lift}$  is the height lifted using the machine and  $t_{print}$  is the total amount of time required to complete the lift. The manual G-Code must be saved as a text file before it can be sent to the machine.

### 3.5.3 Determination of Optimal Machine Feed Rate

The optimal machine feed rate is found by knowing the optimal exposure time, as determined from previous experiments in 3.2.4. Apply the layer height in a similar equation to obtain the optimal feed rate of the machine.

$$f_{opt} = \frac{h_L}{t_{exp}} \quad (3.2)$$

where  $h_L$  is the layer height and  $t_{exp}$  is the optimal exposure time for each layer. The optimal feed rate calculated is then applied in the manual G-Code to the machine as was discussed in 3.3.1. The total time of the machine's operation is observed and the time is recorded as  $t_{print}$ . It is possible to obtain an optimal feed rate, which is lower than the minimum feed rate that was determined. If this situation occurs, the minimum feed rate is equal to the optimal feed rate.

### 3.5.4 Determination of Adjusted Video Frame Rate

Execute the STL reader code with the same part and observe the time of the output video. This time is recorded as  $t_{video}$  and since the time of the video needs to be equal to the time of the print to successfully implement a layerless process, the adjusted video frame rate can be calculated by using the following equation:

$$v_{F adj} = \frac{t_{video}}{t_{print}} v_{F curr} \quad (3.3)$$

where variable  $v_{F curr}$  is the current frame rate found in the SLA video code,  $t_{video}$  is the total length of the current video (in seconds) and  $t_{print}$  is the total build time desired as determined by the controlling software using the manual G-Code. Understanding that the product of the time of the video and the current video frame rate is equal to the number of frames required in the video, equation 3.3 can be simplified even further to the following:

$$v_{F adj} = \frac{n_F}{t_{print}} \quad (3.4)$$

where  $n_F$  is the number of frames. This equation is much more efficient to work with since the number of frames is a constant parameter, provided the part size and layer height remain constant.

The number of frames required in a video can be calculated using the following equation:

$$n_F = \frac{h_{part}}{h_L} \quad (3.5)$$

where  $h_{part}$  is the height of the part manufactured using the layerless system.

### **3.5.5 Synchronizing of Video and Curing Processes**

Changing the frame rate in the STL reader code to the frame rate calculated in the previous step should synchronize the video and machine. To implement the process properly, the video as an output from the program is required to be on the secondary monitor (the monochrome LCD screen) and the image must be positioned underneath and centered with the build plate.

## **4 Implementation**

### **4.1 INTRODUCTION**

The implementation process of the research has two major components. First, the implementation of a functioning STL reader and slicer code is presented. The methodologies involved were retrieval of relevant triangle information such as facets and vertices, triangle relationships, building the STL model and display of its cross-sections from the bottom to top in each step through a video. The second implementation process involves the synchronization of this code with the SLA machine by using an analytical method, where the parameters minimum feed rate of the machine, optimal feed rate of the machine and adjusted video frame rate all need to be determined. The machine is then synchronized with the video by using these parameters and performing some necessary manual calibration steps, as defined in 3.4. All of the implemented code is provided in Appendix C.

## 4.2 IMPLEMENTATION OF THE STL READER AND SLICER

The code involved for the STL reader has one main script. The implementation process to read and obtain the necessary information is explained through pseudo-code as follows:

*Obtain faces and vertices from STL file*

*Specify slice height*

*From minimum to maximum elevation:*

*Between the slice height intervals*

*Associate faces to intersection points based on 3 cases:*

*Points above, points below and points on the same plane as the current elevation*

*End loop*

*End loop*

*Sort all points from minimum height to maximum height*

*Check for duplicate points, if any. Delete all duplicate points*

*From first to last slice:*

*From start to end of the line list of current slice:*

*Find all lines that are connected to one another*

*Connect each of the lines together*

*Store the lines in a variable*

*End loop*

*End loop*

### 4.3 IMPLEMENTATION OF MACHINE SYNCHRONIZATION

Synchronization involves the implementation of one script and the use of manual G-Code in the controlling software. The process of the script is presented in pseudo-code as follows:

*Write video file*

*Assign a frame rate based on the equations in 3.5*

*Open the video file*

*From the first to last slice:*

*Search through all intersection points:*

*Check if points lie inside of the polygon or on its edge*

*Find all interior points and points on the opposite side of the edge*

*End Loop*

*Set the figure handle with the required axis properties and figure properties*

*Store the point data as an array of two columns*

*For the length of the array*

*Color interior points white and all points on opposite side of edge black*

*End Loop*

*Get the frame from the current figure*

*Re-write the video initialized with a new one containing the frame*

*Close the figure*

*End Loop*

*Close the video file*

This code is executed simultaneously with the manual G-code for machine synchronization.

## **5 Implementation Case Studies and Discussion**

### **5.1 INTRODUCTION**

In order to validate the methodology and present case studies, several specimens are designed and fabricated using the classic layered approach and also using the developed layerless approach. The specimens are selected in a way that they demonstrate the capability of the process in creating complex features and also simple but varying features. The resulting surfaces are measured using accurate surface topography. Comparison and discussion on the results of the case studies are presented in this chapter.

One of the manufactured parts is the Rook that was shown in 3.3.5. The modelled Rook has a complex shape with many detailed features. . The other group of parts are simple cubes with chamfered surfaces, called SlantedCubes. The chamfered surfaces have various angles from 5 degrees to 45 degrees with intervals of 5 degrees.

The purpose of the Rook is to demonstrate accuracy, whereas the SlantedCube's purpose is to demonstrate a minimization of the staircase effect through a reduction in surface roughness. Both of the parts will be discussed with respect to their performance by showing qualitative and graphical data, as well as the use of mathematical analysis.

## **5.2 MANUFACTURED ROOK**

The half-sized Rook is printed using manual G-Code, which starts with turning the lights on and a 15 second stationary cure time, before the video is started. This ensures a proper base (similar to a raft layer in FDM manufacturing) such that the cured resin will stick to the build plate. The video is started and for each frame displayed in the video, the build plate moves up a distance equal to the slice height specified in the code. The process repeats until the top of the part has been reached. The result of the print is shown in Figure 5.1. The size of the part is 17.05 mm x 17.05 mm x 28.55 mm.

Notice in particular the details with the door, the windows, the base and the opening at the top. It is difficult to see in the images, but the brick siding can also be observed on the part. From 3.3.4 it was demonstrated how part accuracy varies with size. Achieving such precision on a small part using the proposed layerless method is a significant improvement over the conventional layered part, which will be discussed.

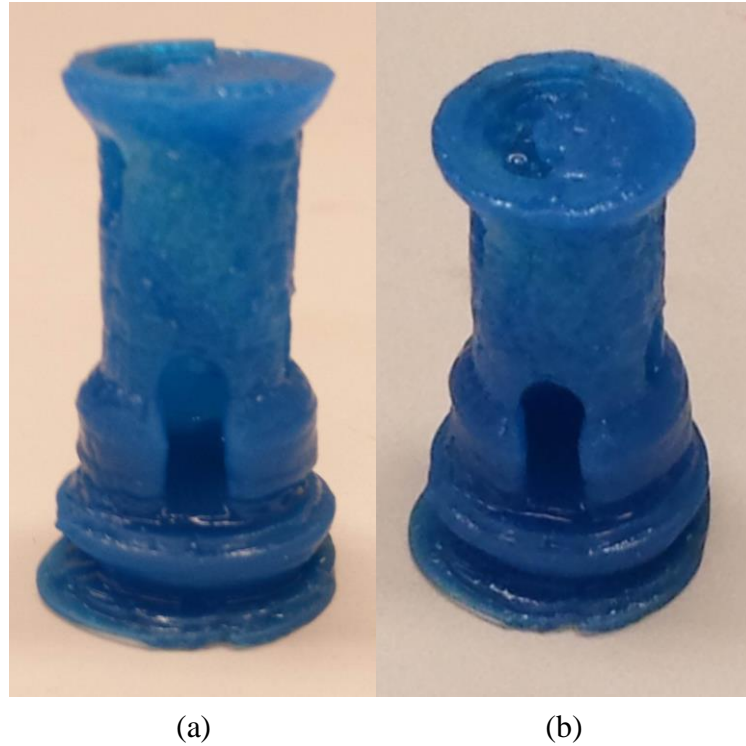


Figure 5.1: Initial Attempt for Rook Layerless Fabrication:  
 (a) View 1, and (b) View 2.

The frame rate used in the video was calculated using equations 3.4 and 3.5 from 3.4.4. The time to complete the print using the G-Code was 28 minutes and 43 seconds, or a total of 1723 seconds.

The number of frames were calculated as follows:

$$n_F = \frac{h_{part}}{h_L}$$

$$n_F = \frac{28.55 \text{ mm}}{0.1 \text{ mm}}$$

$$n_F = 285.5 \sim 286 \text{ frames}$$

therefore 286 images of the part's cross-section are displayed throughout the video. The required frame rate for synchronization of the machine and the video to create the part was calculated as:

$$v_{Fadj} = \frac{n_F}{t_{print}}$$

$$v_{Fadj} = \frac{286 \text{ frames}}{1723 \text{ seconds}}$$

$$v_{Fadj} = 0.166 \frac{\text{frames}}{\text{second}} = 0.166 \text{ FPS}$$

Figure 5.2 shows a profile view of three different sizes of the Rook part fabricated using conventional layered AM practices. The three sizes shown are half size, three-quarter size and full size. The main observation with the three products is the variance in accuracy between the smallest to the largest part. The half-sized Rook appears cluttered and many complex features cannot be seen, such as the brick siding, the windows, the door, and the top opening staircase exit. These features can all be seen on the full-scaled Rook, again confirming that the larger the part being manufactured, the more dimensionally accurate it likely will be. The top view of the same parts is shown in Figure 5.3. The layerless produced Rook is the same size as the far-left part. Notice the difference in dimensional accuracy of its complex features.



Figure 5.2: Profile View of Three Different-Sized Rook Parts Using Layered Manufacturing.



Figure 5.3: Top View of Three Different-Sized Rook Parts Using Layered Manufacturing.

### 5.3 MANUFACTURED SLANTEDCUBE

The SlantedCube part is printed using the same approach as the Rook, with the same raft cure time, feed rates and slice height. The size of the SlantedCube part is 15 mm x 15 mm x 12 mm. The STL file is shown in Figure 5.4 and a view of the layerless-fabricated part is shown in Figure 5.5 (a). Figure 5.5 (b) shows the smooth edge of the same part without the staircase effect.

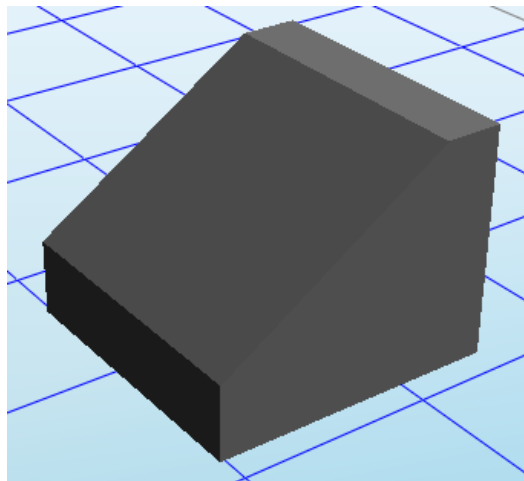


Figure 5.4: SlantedCube STL File.

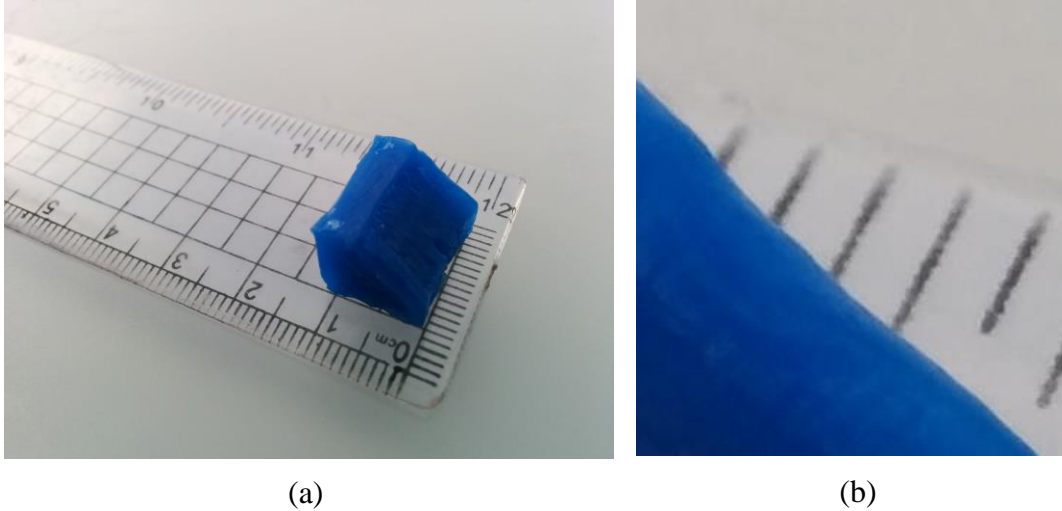


Figure 5.5: (a) SlantedCube Layerless Part, and (b) Part Edge without the Staircase Effect.

Using the manual G-Code, the total time required to print the SlantedCube part was 12 minutes and 7 seconds, or a total of 727 seconds. Using equation 3.5 to calculate the required number of frames:

$$n_F = \frac{h_{part}}{h_L}$$

$$n_F = \frac{12 \text{ mm}}{0.1 \text{ mm}}$$

$$n_F = 120 \text{ frames}$$

and applying the number of frames to equation 3.4, the required frame rate for synchronization was calculated as:

$$v_{Fadj} = \frac{n_F}{t_{print}}$$

$$v_{Fadj} = \frac{120 \text{ frames}}{727 \text{ seconds}}$$

$$v_{Fadj} = 0.165 \frac{\text{frames}}{\text{second}} = 0.165 \text{ FPS}$$

which is very close to the Rook's required frame rate. Taking the reciprocal of both of these values, the units are interchanged and the value is approximately 6 seconds per frame, or a translation of 6 seconds of curing per layer. This was a requirement as a result from past experiments in the methodology for the layered process.

The most significant feature on the 3D printed SlantedCube part is the smooth chamfered surface as a result of the layerless process. Comparing this surface to the same part fabricated using layered manufacturing, the layers are no longer visible and as a result, the surface quality has improved using the new AM process. The surface is analyzed using a microscope with a lens giving 5 times magnification. A Surface Topography device was required to obtain the necessary surface roughness geometry and roughness parameters.

The 3D roughness shape of the angled surface obtained from layered manufacturing is shown in Figure 5.6. The color bar on the right side of the roughness topography indicates the value of deviation at various locations on the surface, from lowest (dark blue) to highest (dark red). The same color bar applies to all of the samples analyzed, however the values change. The goal is to reduce the cusp height between the nominal geometry and part geometry as much as possible, which gives a smoother surface and lower surface roughness. This becomes a larger problem for parts built with a large layer thickness. Eliminating the need for layers in the build process eliminates this problem as the part is built continuously instead of sequentially.

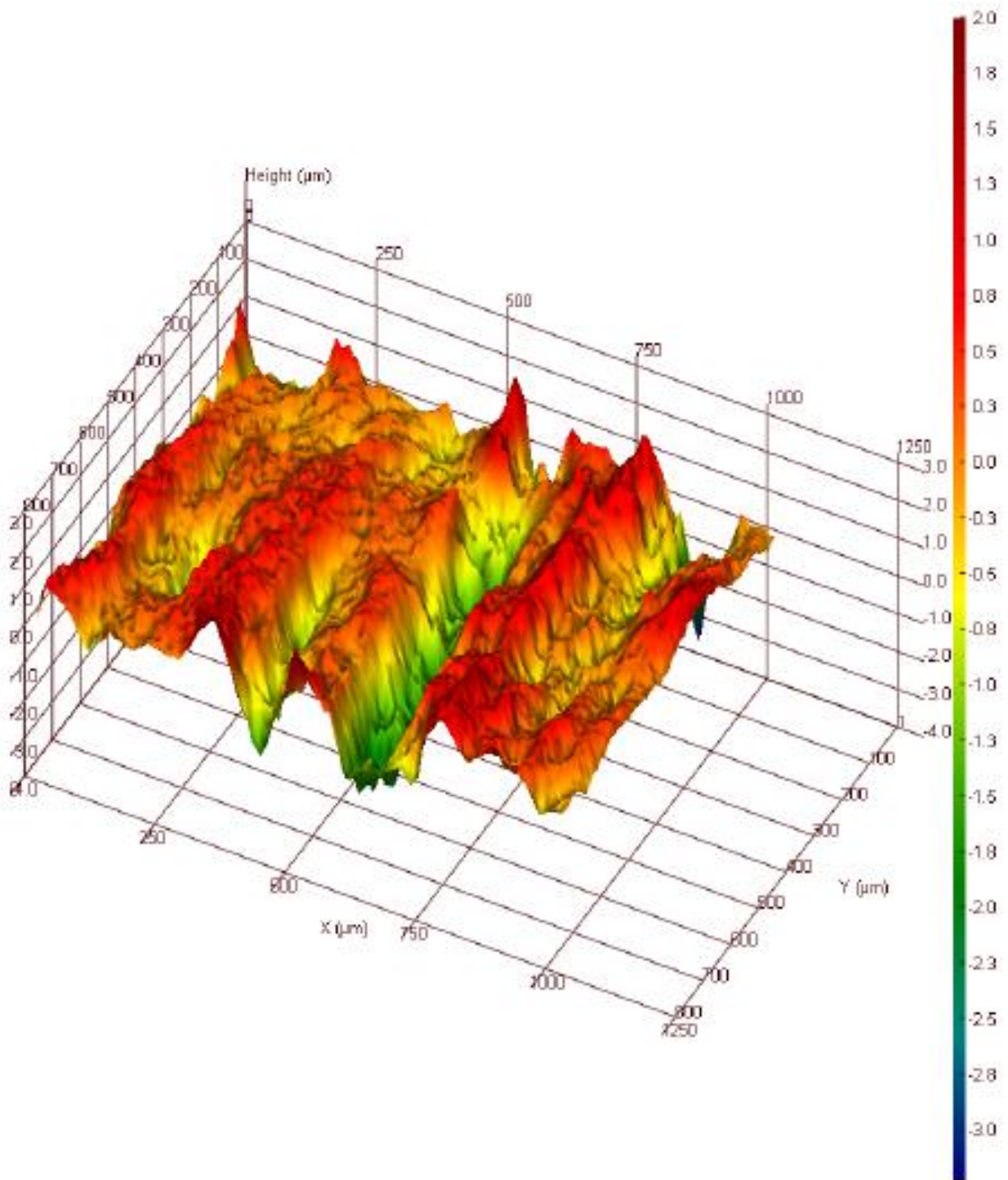


Figure 5.6: SLA 3D Roughness Shape of Layered Angled Surface ( $S_a = 0.653 \mu\text{m}$ ).

Figure 5.7 shows the 3D surface topography data best representing the 3D roughness shape of the SlantedCube chamfered surface. A total of 12 different locations on the surface are measured and averaged in order to get a realistic estimation of the surface roughness and quality.

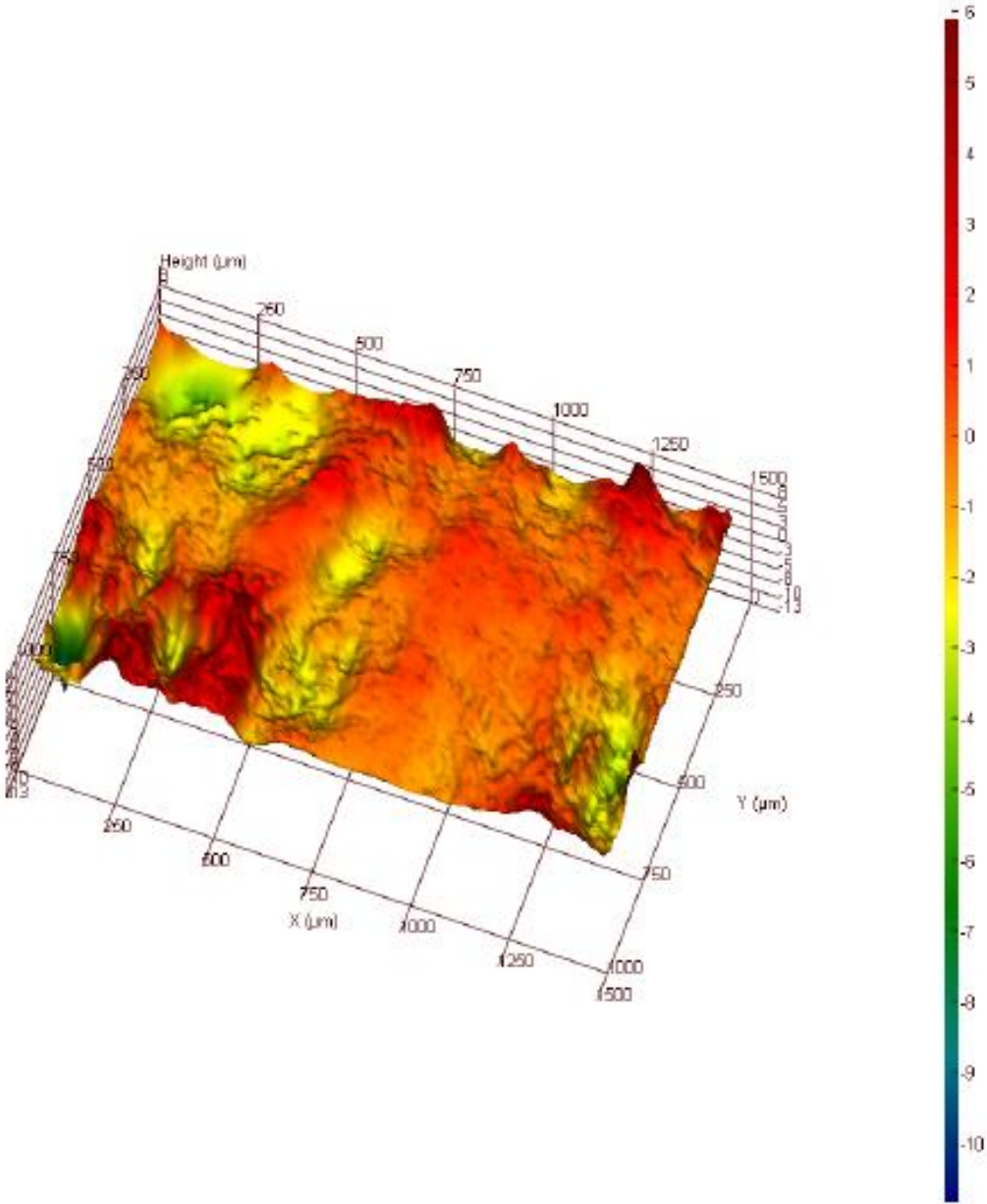


Figure 5.7: SLA 3D Roughness Shape of Layerless Angled Surface ( $S_a = 0.126 \mu\text{m}$ ).

On initial inspection, the surface profile is much smoother for the layerless surface than the layered surface. Looking at the roughness profile in each case, it can be observed how the staircase effect has been affected. In the layered case, the peaks and valleys on the surface are much more visible. In the layerless case, most of the profile appears flat and there are no significant peaks or valleys to indicate a stepping effect. In order to validate this discovery, a few important case studies are performed. These case studies involve fabrication of several SlantedCube parts using both the layered and layerless methods. Nine samples are manufactured with a surface angle from 5 degrees to 45 degrees for each case. The results are analyzed through inspection of microscopic data and the surface roughness from the layered and layerless cases are compared.

The surface roughness parameter that is analyzed in all parts is  $S_a$ , a 3D parameter concerning the arithmetic mean height of the entire surface. The percent decrease in surface roughness comparing the layerless and layered systems can be calculated using the percent difference formula as follows:

$$\% \text{ diff} = \frac{SR_O - SR_{LL}}{SR_O} * 100\% \quad (5.1)$$

where  $SR_{LL}$  is the experimental surface roughness obtained from the layerless part and  $SR_O$  is the original surface roughness obtained from the conventional layer manufactured part.

### 5.3.1 Layer-Manufactured Angled Surfaces

Figure 5.8 shows the CAD models of the 9 SlantedCubes to be fabricated between 5 degrees and 45 degrees with 5 degree increments. Figure 5.9 to Figure 5.17 show the 3D roughness topology of the angled surface for each sample constructed using the conventional layered process.

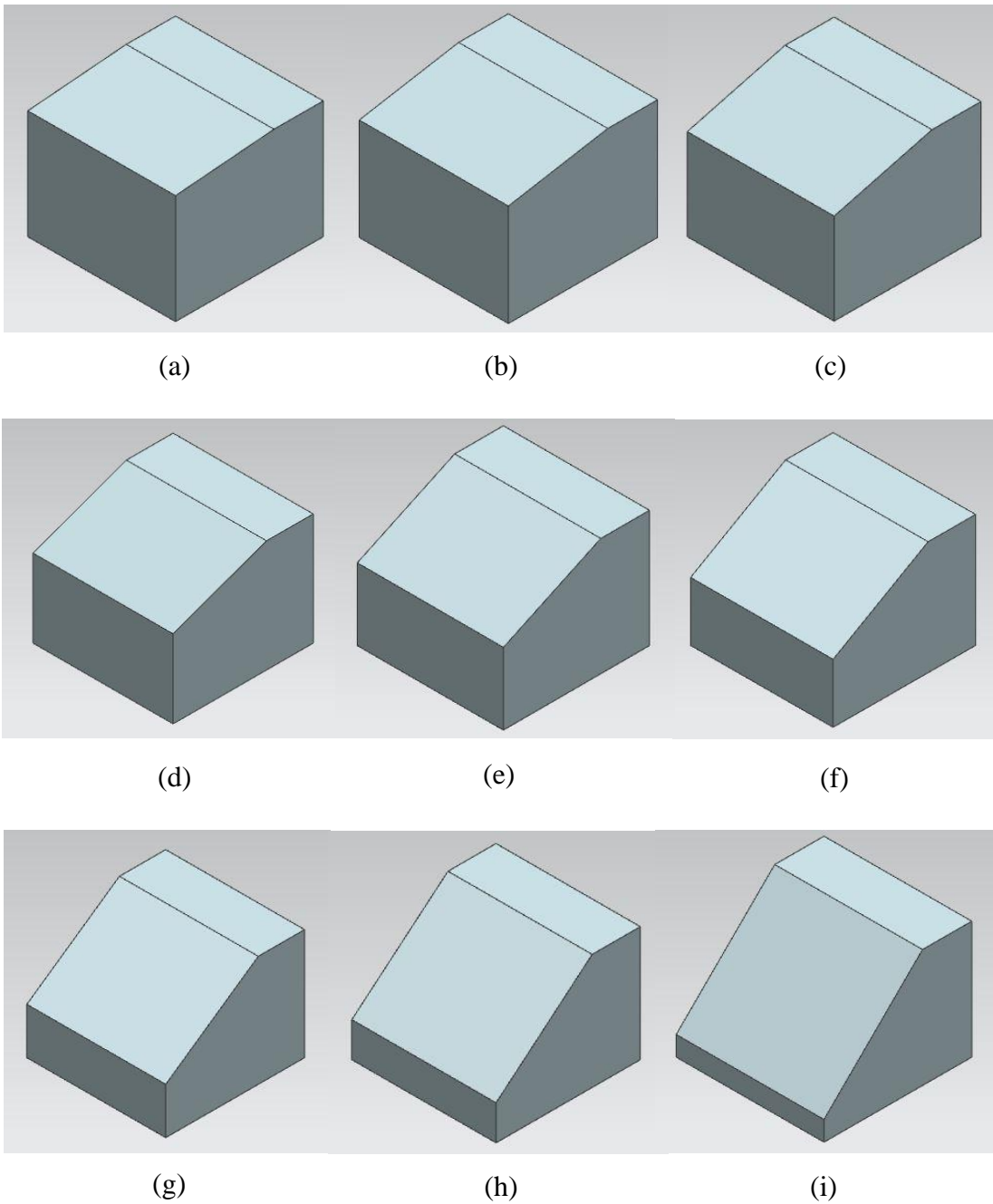


Figure 5.8: CAD models of SlantedCubes with surfaces angled at: (a) 5 degrees (b) 10 degrees (c) 15 degrees (d) 20 degrees (e) 25 degrees (f) 30 degrees (g) 35 degrees (h) 40 degrees and (i) 45 degrees.

The models are angled with respect to the x-axis and they are displayed in increasing order from left to right and top to bottom.

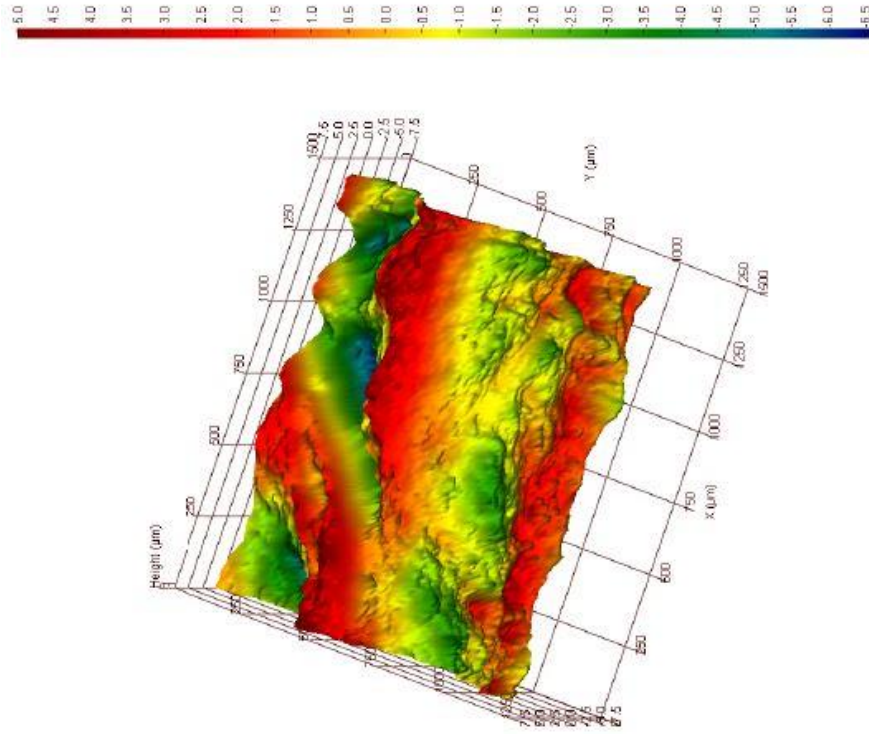


Figure 5.9: SLA Roughness of Layered 5-Degree Surface ( $S_a = 0.854 \mu\text{m}$ ).

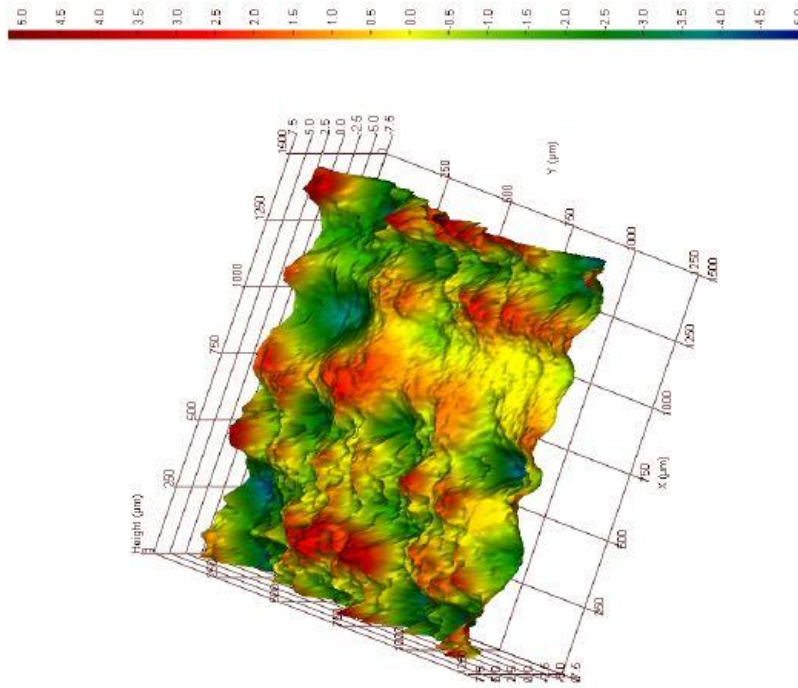


Figure 5.10: SLA Roughness of Layered 10-Degree Surface ( $S_a = 0.876 \mu\text{m}$ ).

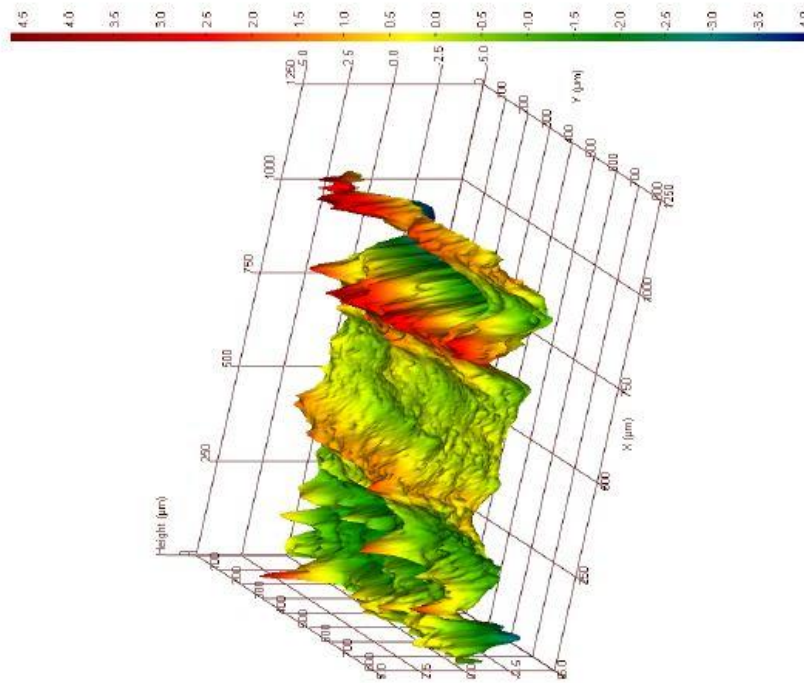


Figure 5.11: SLA Roughness of Layered 15-Degree Surface ( $S_a = 0.669 \mu\text{m}$ ).

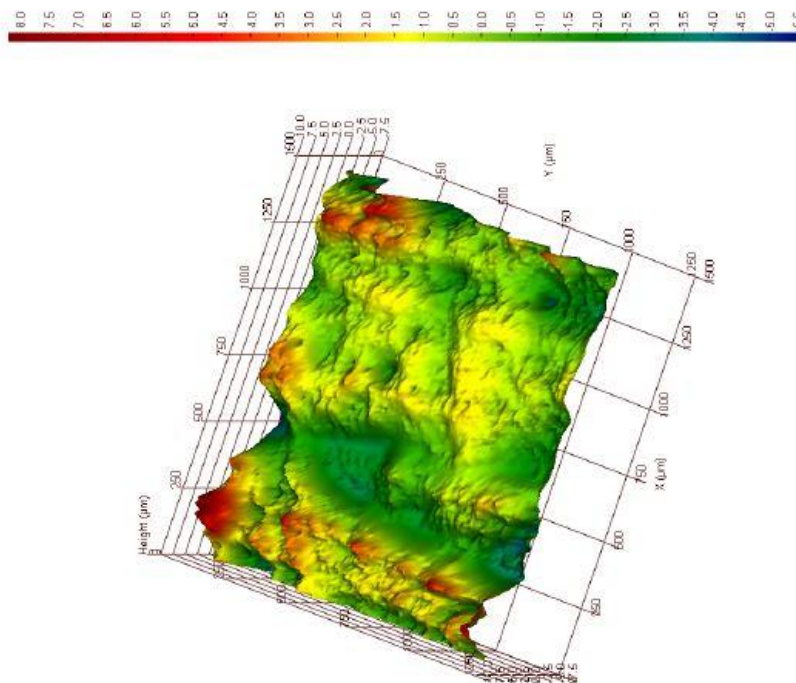


Figure 5.12: SLA Roughness of Layered 20-Degree Surface ( $S_a = 0.752 \mu\text{m}$ ).

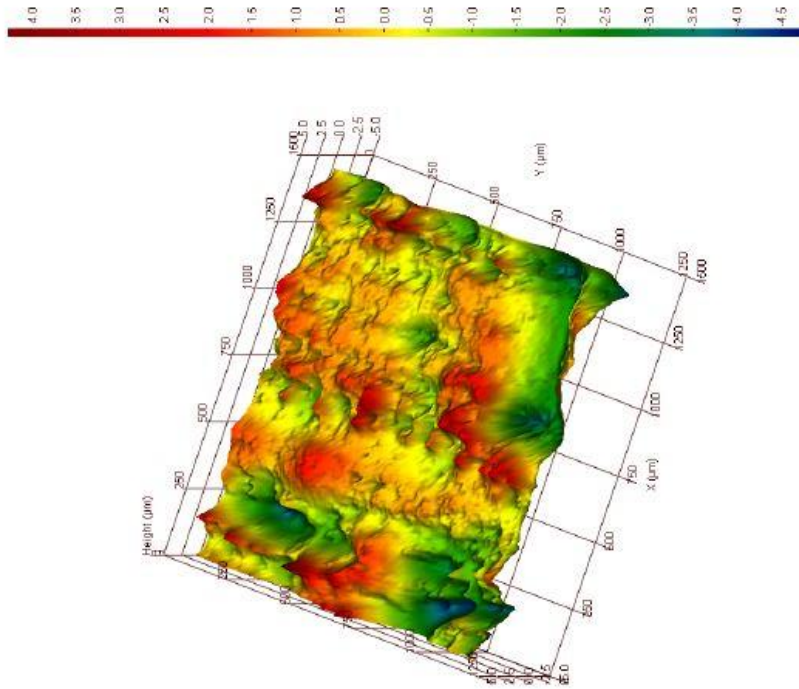


Figure 5.13: SLA Roughness of Layered 25-Degree Surface ( $S_a = 0.601 \mu\text{m}$ ).

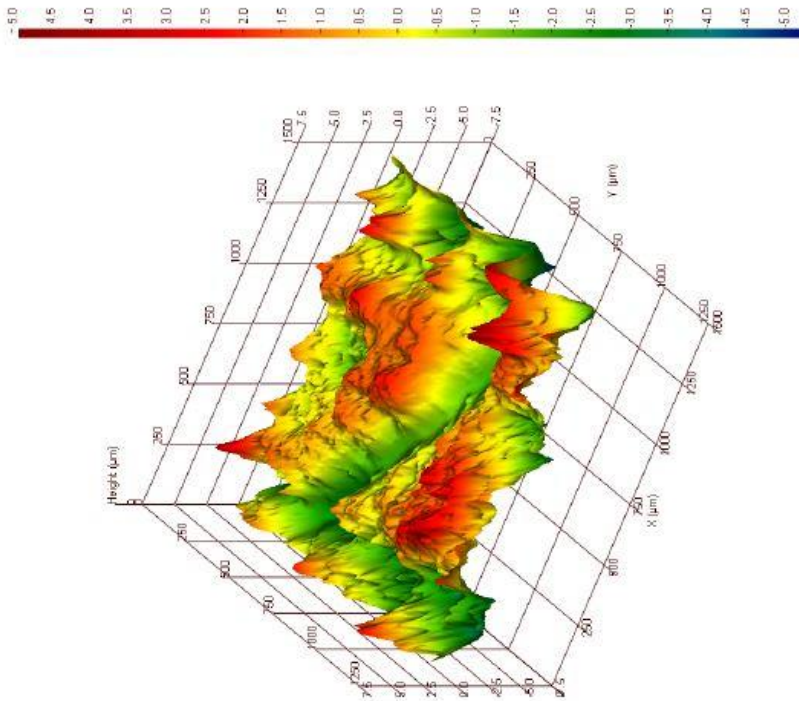


Figure 5.14: SLA Roughness of Layered 30-Degree Surface ( $S_a = 0.702 \mu\text{m}$ ).

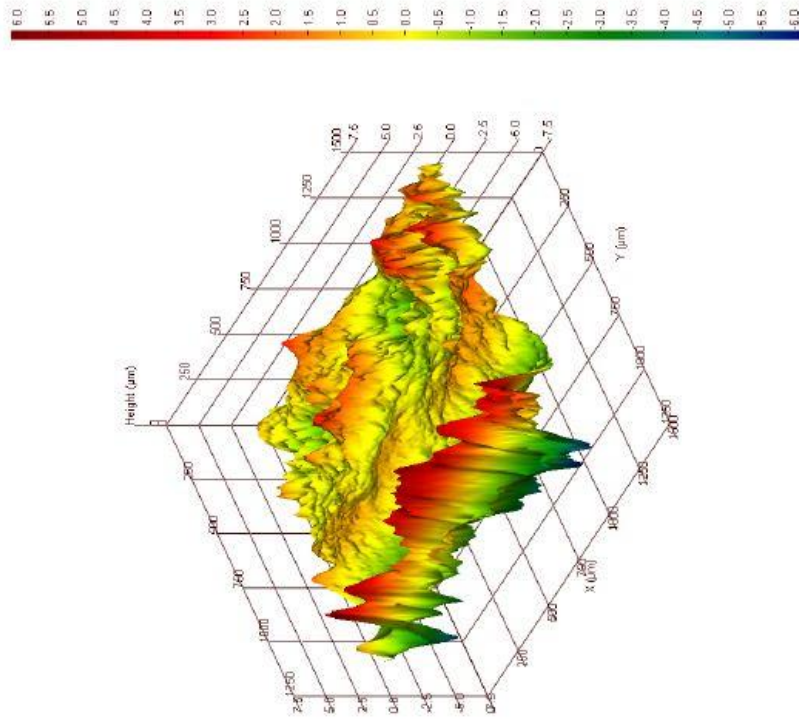


Figure 5.15: SLA Roughness of Layered 35-Degree Surface ( $S_a = 0.752 \mu\text{m}$ ).

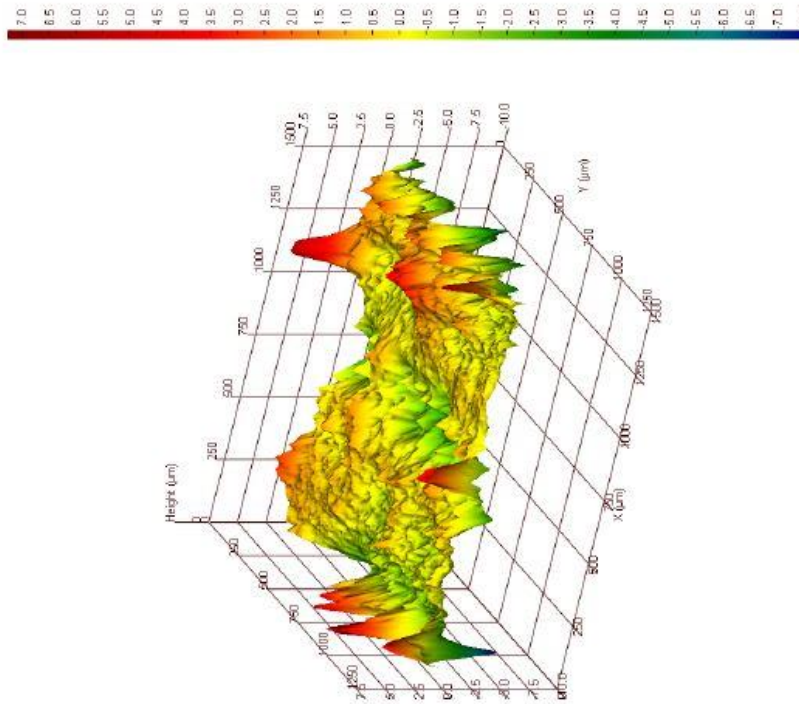


Figure 5.16: SLA Roughness of Layered 40-Degree Surface ( $S_a = 0.595 \mu\text{m}$ ).

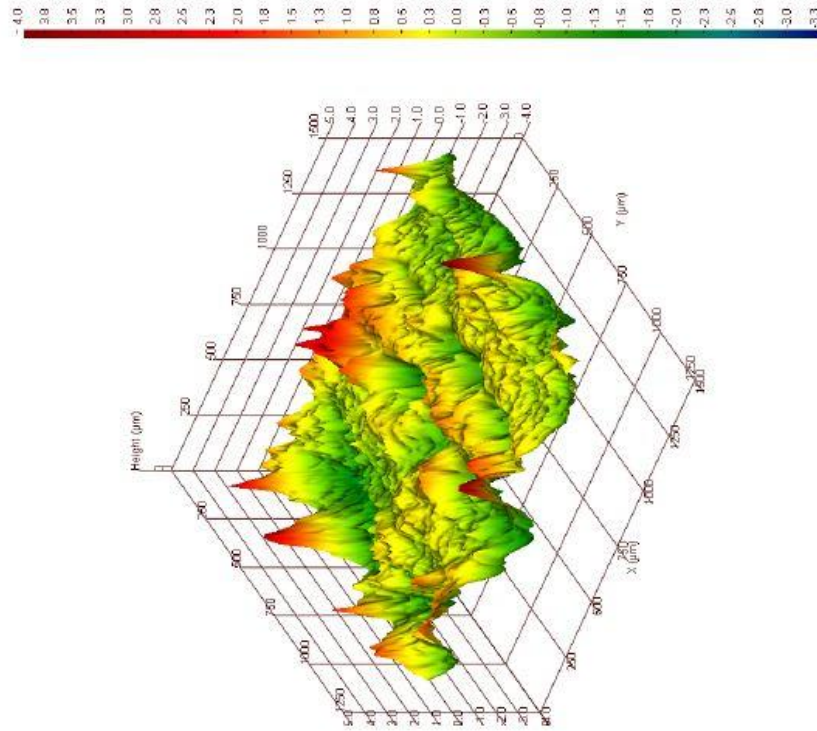


Figure 5.17: SLA Roughness of Layered 45-Degree Surface ( $S_a = 0.454 \mu\text{m}$ ).

### 5.3.2 Layerless-Manufactured Angled Surfaces

Figure 5.18 to Figure 5.26 show the 3D topology of the surface roughness for SlantedCube surfaces angled between 5 degrees and 45 degrees using layerless fabrication.

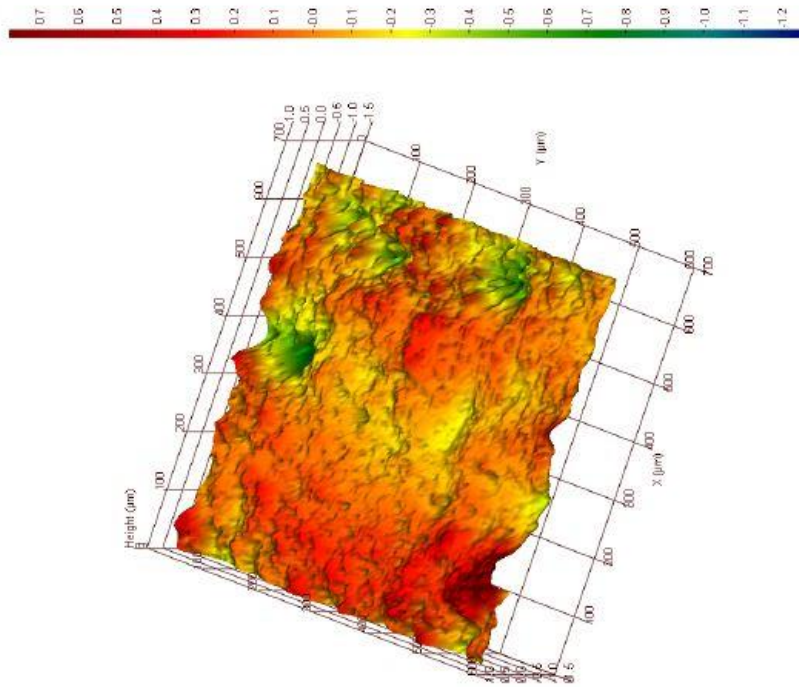


Figure 5.18: SLA Roughness of Layerless 5-Degree Surface ( $S_a = 0.0934 \mu\text{m}$ ).

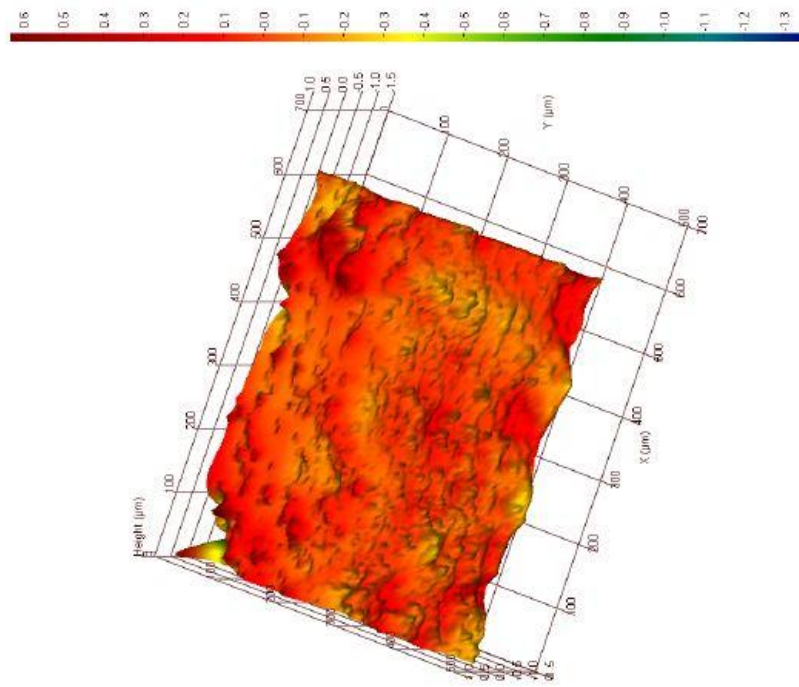


Figure 5.19: SLA Roughness of Layerless 10-Degree Surface ( $S_a = 0.0714 \mu\text{m}$ ).

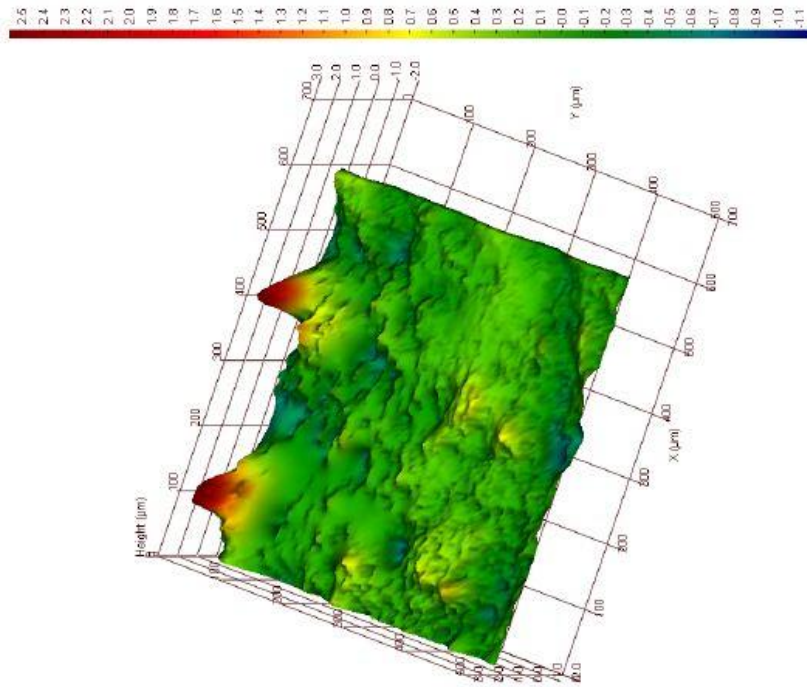


Figure 5.20: SLA Roughness of Layerless 15-Degree Surface ( $S_a = 0.187 \mu\text{m}$ ).

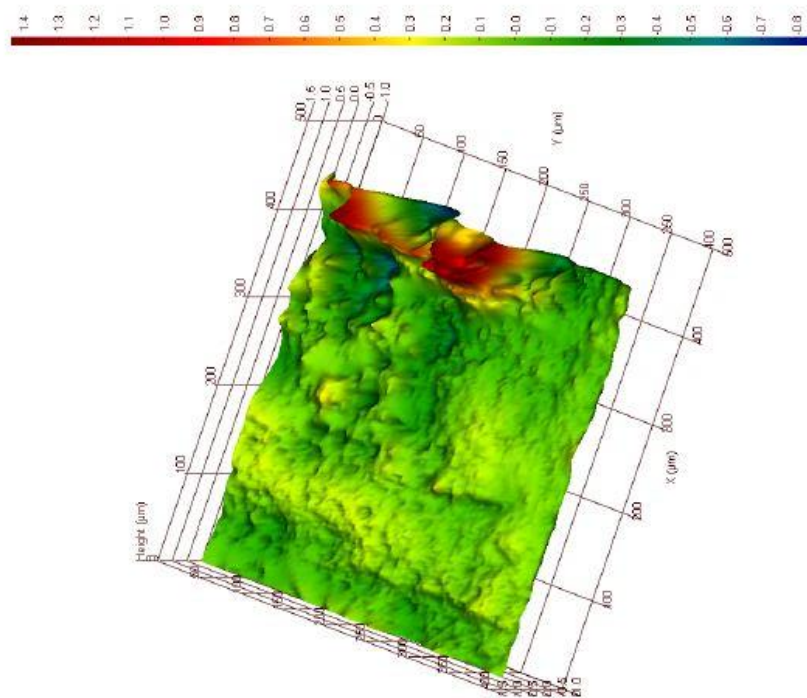


Figure 5.21: SLA Roughness of Layerless 20-Degree Surface ( $S_a = 0.129 \mu\text{m}$ ).

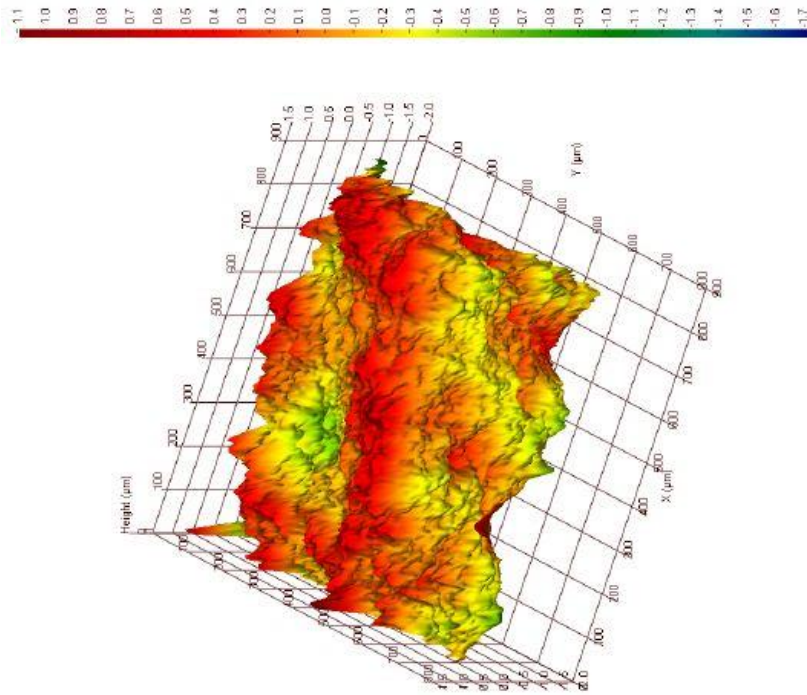


Figure 5.22: SLA Roughness of Layerless 25-Degree Surface ( $S_a = 0.179 \mu\text{m}$ ).

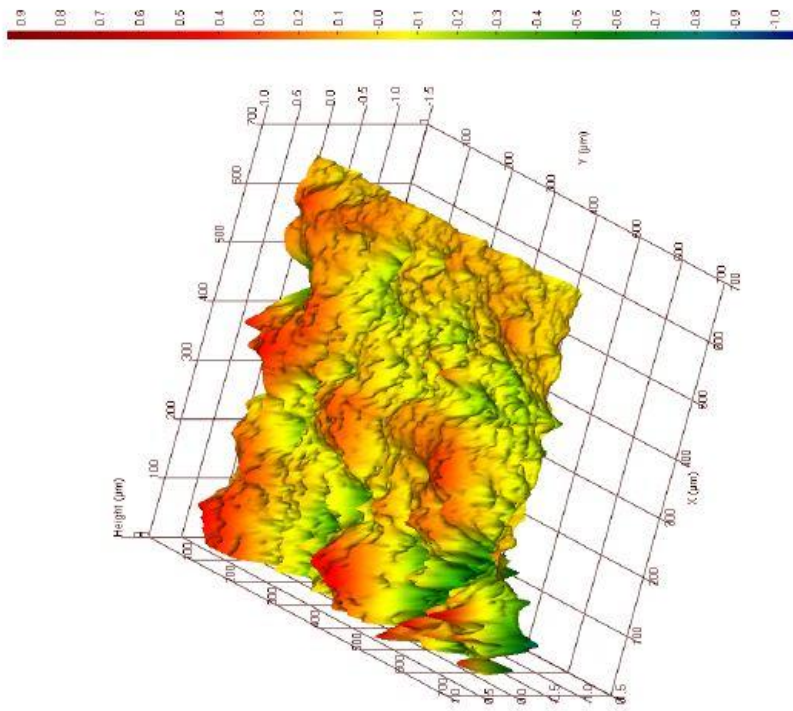


Figure 5.23: SLA Roughness of Layerless 30-Degree Surface ( $S_a = 0.117 \mu\text{m}$ ).

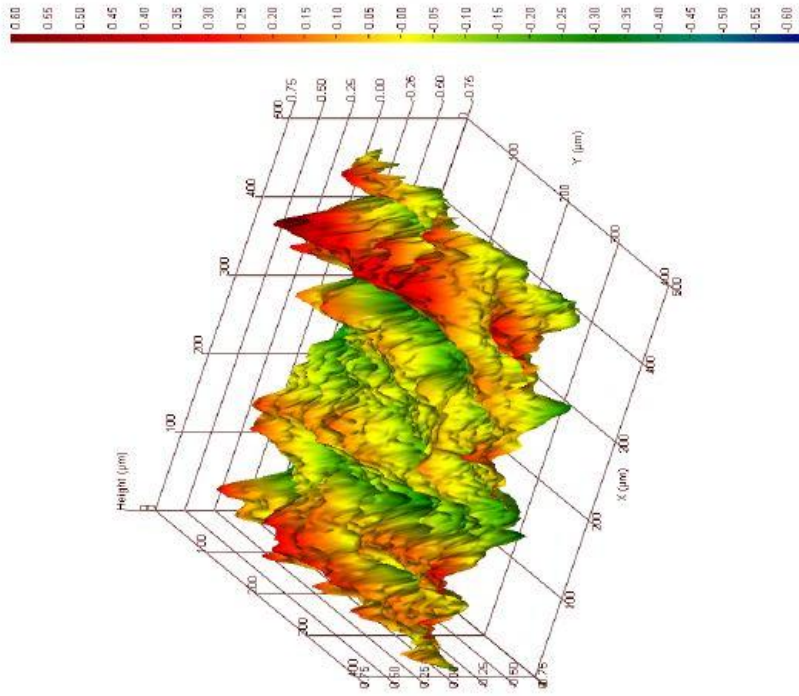


Figure 5.24: SLA Roughness of Layerless 35-Degree Surface ( $S_a = 0.107 \mu\text{m}$ ).

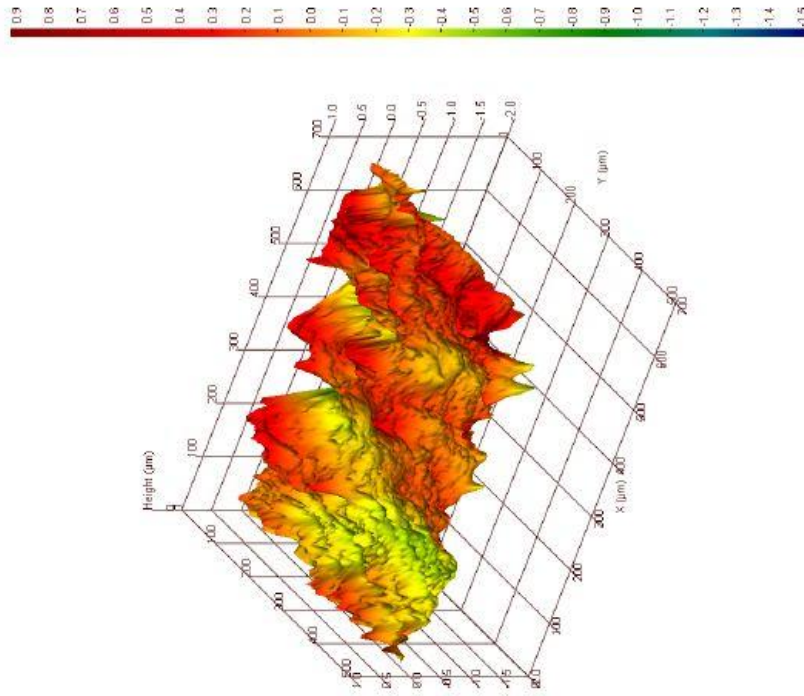


Figure 5.25: SLA Roughness of Layerless 40-Degree Surface ( $S_a = 0.137 \mu\text{m}$ ).

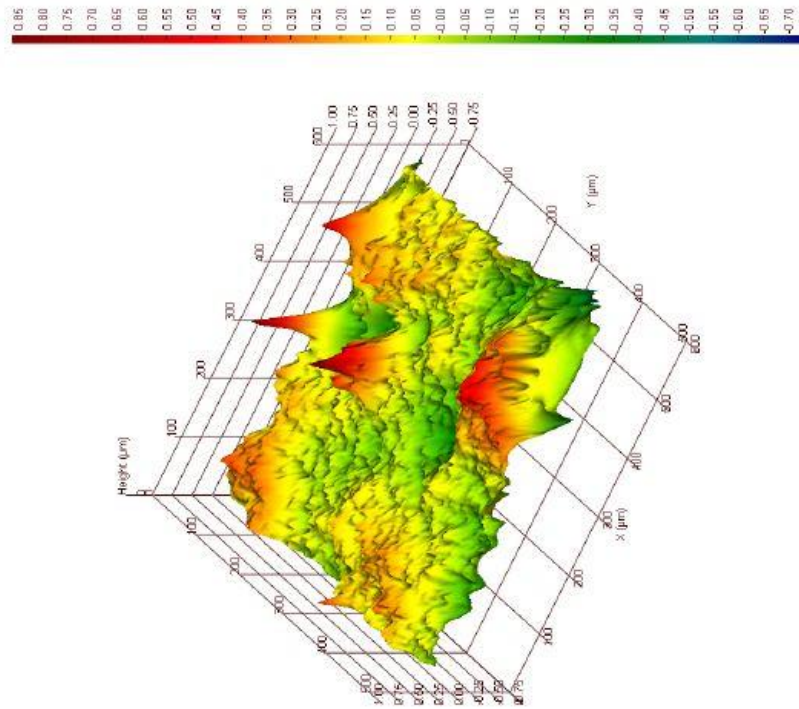


Figure 5.26: SLA Roughness of Layerless 45-Degree Surface ( $S_a = 0.114 \mu\text{m}$ ).

### 5.3.3 Comparison of SLA Layered and Layerless Manufactured Angled Surfaces

Table 5.1 shows the comparison of the microscopic data for the layered and layerless part surfaces with respect to surface roughness. Using equation 5.1, the percent reduction in surface roughness is calculated with respect to the layerless process to express validity. All of the layered samples were constructed using a layer thickness of 0.1 mm. All of the layerless samples used this value as the slice height.

Table 5.1: Comparison of Layered and Layerless Angled Surface Roughness.

Material	SLA Layered	SLA Layerless	% Reduction
Surface Angle (degrees)	Surface Roughness Sa ( $\mu\text{m}$ )		
5	0.854	0.0934	89.1
10	0.876	0.0714	91.8
15	0.669	0.187	72.0
20	0.752	0.129	82.8
25	0.601	0.179	70.2
30	0.702	0.117	83.3
35	0.752	0.107	85.8
40	0.595	0.137	77.0
45	0.454	0.114	74.9

Observing Table 5.1, the percent reduction in surface roughness when comparing the layered and layerless processes is significant. A graphical representation of this data is shown in Figure 5.27.

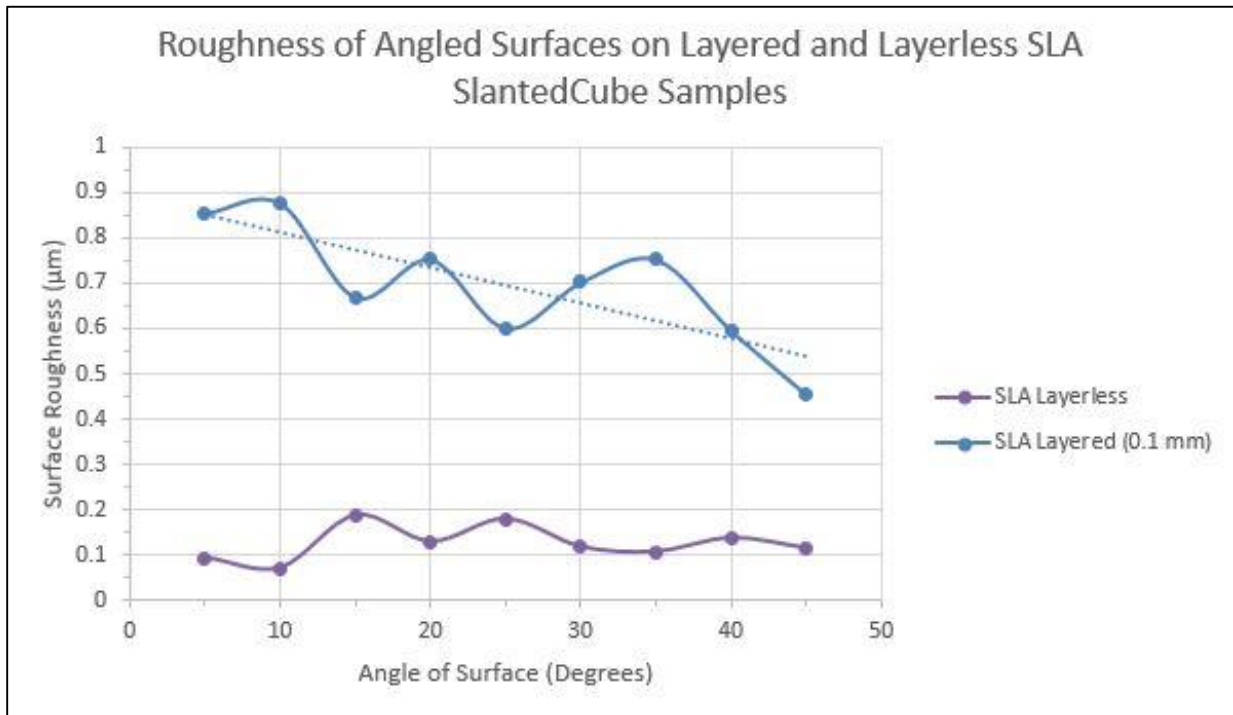


Figure 5.27: Roughness of Angled Surfaces for Layered and Layerless Processes.

The average observed reduction was 80% with standard deviation of 8%, proving a substantial improvement in surface quality by implementing the layerless approach. The graph shows not only that the layerless parts have a lower surface roughness overall, but also that the roughness value is more consistent and is independent from the slope of the surfaces. Notice also the relationship of the layered parts with the surface angle. There is a decreasing trend, indicating larger angles generally resulting in lower measured surface roughness. This confirms with past theory in AM processes. The behavior of the roughness pattern using the layered approach is much less predictable and the surface quality is lower. This is better observed in the microscopic images of the 3D roughness shape for each of the angled surfaces. In general, the roughness profile is much more flat on the layerless parts and there are also fewer irregularities and defects throughout the surface when compared to the layered part surfaces.

## **6 Conclusions and Future Work**

### **6.1 CONCLUSIONS**

A layerless manufacturing method is presented in this thesis by using synchronization between an STL reader code and an SLA 3D printing machine. The synchronization process involves writing a functional code and integrating the output video with the operation of the machine. By implementing this layerless approach, the layered manufacturing problem staircase effect is minimized and the surface quality of the part is improved with minimum dimensional error. The processes involved in the methodology were to understand the limitations and capabilities of the software used, explaining the design and functionality of the SLA machine, performing any necessary manual calibration of the machine to reduce part construction error and finally the approach behind the layerless AM process by implementing synchronization. Dimensional accuracy of the layer printing was improved by experimental study of the required

compensation and scaling parameters which are used for calibration of the machine. In order to study the capability of the layerless process, several parts were printed, of which the focus was improving the surface quality, dimensional accuracy and reducing the staircase effect separately.

The Rook specimens have very detailed geometric features. Its purpose was to demonstrate the improvement of dimensional accuracy using the newly proposed layerless method, and this was done by comparison to the same part printed using the conventional layered manufacturing process with 0.1 mm layer thickness. Results showed that small complex features were clearly visible on the layerless Rook, whereas the same features on the layered Rook were cluttered and deformed. The methodology involved determining the optimal parameters for the layerless printing process. These parameters consisted of the exposure or curing time, the total build time for the machine according to the manual input G-Code, the number of frames and the frame rate for the video. The process is dynamic because the machine synchronizes with the video displaying the images of the cross-sections while the system is lifting.

In order to study the effect of the layerless approach on the surface quality of the final product, a family of the parts called SlantedCubes were fabricated using the layered and also the layerless processes. The SlantedCubes were fabricated using the same curing parameters as the Rook. Its purpose was to demonstrate the minimizing of the staircase effect on the part's angled surface, thereby increasing its surface quality. Layerless parts were compared to layered parts (also with 0.1 mm layer thickness). Measurements were done by using a 3D microscope. The results showed that the surface roughness was reduced by an average of 80%, thereby reducing the staircase effect substantially through the layerless method. Another interesting result was that the value of surface roughness of the layerless samples were independent of the fabricated angle. The

images obtained from the microscopic data showed that the layerless-constructed parts had a more consistent profile as well as fewer surface defects than layered parts.

All of the experiments conducted yielded robust results and are applicable to any machine setup. However, the optimal parameters will vary depending on the equipment used on the machine, such as the motors, the light source and the monitor. The SLA layerless setup that is implemented in this research is not optimal. In order for the process to be improved, a more powerful light source should be used or a motor capable of rotating at a slower speed, thus allowing a lower feed rate should be considered. The cheaper alternative would be the latter, but with respect to which alternative would give the best result overall will be left to further research.

The proposed implementation is only limited to SLA AM processes. Different methodologies are required for different AM processes. Discovering ways to eliminate the requirement of layers in additive manufacturing will result in more efficient performance combined with better part quality overall. With technology and research rapidly expanding in additive manufacturing today, there are many areas that require constant improvement. SLA is a relatively new application in AM, and there are still many topics of research to be investigated.

Generation of a functional STL reader code and synchronizing of a video and the machine are the two main implementation tasks in a layerless SLA manufacturing system that are covered in this work. It is shown that the products created from these two tasks are feasible and robust and provide improvement in dimensional accuracy and surface quality. The staircase effect is effectively reduced and this sets a good base for the expansion of this important topic in research with additive manufacturing. The next step would be to investigate the results after making the necessary modifications to the system as mentioned before. Switching the setup from UV-LED to a Digital Light Processing (DLP) projector would most likely provide improvement in the results.

## 6.2 FUTURE WORK

Layerless SLA is a relatively new topic in AM research. There are many topics of this field to be investigated. It is possible to make the SLA machine more efficient by switching to a DLP projector system, thus not only speeding up the process but also improving on the quality of the results. Another option is to swap the current NEMA-17 motors with motors permitting slower machine operation (lower feed rate and better precision). A more thorough analysis of the effect of light intensity on dimensional accuracy and surface quality can be researched, covering more comprehensive shapes. Changing the chemical structure of the photopolymer resin is another way to affect its sensitivity to light, speed of curing, and absorbance of light. This is a recommended undertaking for a chemical engineer who understands organic chemistry. One of the characteristics of resin that is significantly affected by a light source is its color. A study can be done on the amount of exposure time required for several different colors of resin, as well as a light absorbancy graph depending on the wavelength of the light source. Finally, with respect to reducing the staircase effect, this should be studied for as many AM processes as possible. Doing so will improve the quality of parts fabricated and in some cases, will reduce the total time required to fabricate parts, becoming more efficient and saving companies time and money.

## References

- [Gibson et al. 2010] Gibson, L., Rosen, D. W., Stucker, B., 2010, “Additive Manufacturing Technologies: Rapid Prototyping to Direct Digital Manufacturing”, Springer Science+Business, LLC, Springer New York Heidelberg Dordrecht London.
- [Karsten et al. 2009] Karsten, R., Larston, B., Miller, K., 2009, “Characterizing the Efficiency of LED Curing”, Phoseon Technology, RadTech Europe.
- [Pandey et al. 2003] Pandey, P. M., Reddy, N. V., Dhande, S. G., 2003, “Improvement of surface finish by staircase machining in fused deposition modeling”, Journal of Materials Processing Technology, Vol. 132, pp. 323-331.
- [Thrimurthulu et al. 2003] Thrimurthulu, K., Pandey, P. M., Reddy, N. V., 2003, “Optimum part deposition orientation in fused deposition modeling”, International Journal of Machine Tools & Manufacturing, Vol. 44, pp. 585-594. DOI: 10.1016/j.ijmachtools.2003.12.004.
- [Barari et al. 2007] Barari, A., ElMaraghy, H. A., Knopf, G. K., 2007, “Search-Guided Sampling to Reduce Uncertainty of Minimum Deviation Zone Estimation”, ASME Journal of Computing Information Science and Engineering, Vol. 7, pp. 360-371, DOI: 10.1115/1.2798114.
- [Ahn et al. 2009] Ahn, D., Kweon, J.-H., Kwon, S., Song, J., Lee, S., 2009, “Representation of surface roughness in fused deposition modeling”, Journal of Materials Processing Technology, Vol. 209, pp. 5593-5600, DOI: 10.1016/j.jmatprotec.2009.05.016.
- [Galantucci et al. 2009] Galantucci, L.M., Lavecchia, F., Percoco, G., 2009, “Experimental study aiming to enhance the surface finish of fused deposition modeled parts”, CIRP Annals – Manufacturing Technology, Vol. 58, pp. 189-192, DOI: 10.1016/j.cirp.2009.03.071.
- [Jamiolahmadi and Barari 2014] Jamiolahmadi, S., Barari, A., 2014, “Surface Topography of Additive Manufacturing Parts Using a Finite Difference Approach”, Journal of Manufacturing Science and Engineering, Vol. 136, pp. 1-8, DOI: 10.1115/1.4028585.
- [Sikder et al. 2015] Sikder, S., Barari, A., Kishawy, H.A., 2015, "Global adaptive slicing of NURBS based sculptured surface for minimum texture error in rapid prototyping", Rapid Prototyping Journal, Vol. 21 Iss 6 pp. 649 – 661, DOI: <http://dx.doi.org/10.1108/RPJ-09-2013-0090>.
- [Boschetto and Bottini 2015] Boschetto, A., Bottini, A., 2015, "Surface improvement of fused deposition modeling parts by barrel finishing", Rapid Prototyping Journal, Vol. 21 Iss 6 pp. 686 – 696, DOI: <http://dx.doi.org/10.1108/RPJ-10-2013-0105>.
- [Jamiolahmadi and Barari 2015] Jamiolahmadi, S., Barari, A., 2015, “A Genetic Programming Approach to Model Detailed Surface Integrity of Additive Manufacturing Parts, International

Federation of Automatic Control, Vol. 48, No. 3, pp. 2339-2344, DOI: 10.1016/j.ifacol.2015.06.437.

[Kaji and Barari 2015] Kaji, F., Barari, A., 2015, "Evaluation of the Surface Roughness of Additive Manufacturing Parts Based on the Modelling of Cusp Geometry", International Federation of Automatic Control, Vol. 48, No. 3, pp. 658-663, DOI: 10.1016/j.ifacol.2015.06.157.

[Giordano et al. 1996] Giordano, R.A., Wu, B.M., Borland, S.W., Cima, L.G., Sachs, E.M., Cima, M.J., 1996, "Mechanical properties of dense polylactic acid structures fabricated by three dimensional printing". Journal of Biomaterial Science Polymer Edition, Vol. 8, No. 1, pp. 63-75

[Pfister et al. 2005] Pfister, A., Walz, U., Laib, A., Mulhaupt, R., 2005, "Polymer Ionomers for Rapid Prototyping and Rapid Manufacturing by Means of 3D Printing". Journal of Macromolecular Materials and Engineering, 290, pp. 99-113. DOI: 10.1002/mame.200400282.

[Shivpuri et al. 2005] Shivpuri, R., Cheng, X., Agarwal, K., Babu, S., 2005, "Evaluation of 3D printing for dies in low volume forging of 7075 aluminum helicopter parts", Rapid Prototyping Journal, Vol. 11 Iss 5 pp. 272 – 277

[Kim et al. 2008] Kim, I., Song, Y.A., Jung, H.C., Joung, J.W., Ryu, S., Kim, J., 2008, "Effect of Microstructural Development on Mechanical and Electrical Properties of Inkjet-Printed Ag Films". Journal of Electronic Materials, Vol. 37, No. 12, DOI: 10.1007/s11664-008-0552-y

[Kou and Tan 2009] Kou, X.Y., Tan, S.T., 2009, "Robust and efficient algorithms for rapid prototyping of heterogeneous objects", Rapid Prototyping Journal, Vol. 15 Iss 1 pp. 5 – 18

[Sood et al. 2009] Sood, A.K., Ohdar, R.K., Mahapatra, S.S., 2009, "Parametric appraisal of mechanical property of fused deposition modelling processed parts". Journal of Materials and Design, V. 31, pp. 287-295

[Zañartu-Apara and Ramos-Grez 2010] Zañartu-Apara, G., Ramos-Grez, J., 2010, "Characterization of the mechanical properties of samples fabricated by an experimental SGM device", Rapid Prototyping Journal, Vol. 16 Iss 5 pp. 356 – 364

[Chimento et al. 2011] Chimento, J., Highsmith, M.J., Crane, N., 2011, "3D printed tooling for thermoforming of medical devices", Rapid Prototyping Journal, Vol. 17 Iss 5 pp. 387 – 392

[Marchelli et al. 2011] Marchelli, G., Prabhakar, R., Storti, D., Ganter, M., 2011, "The guide to glass 3D printing: developments, methods, diagnostics and results", Rapid Prototyping Journal, Vol. 17 Iss 3 pp. 187 – 194

[Li et al. 2012] Li, X., Zhang, L., Yin, X., 2012, "Microstructure and mechanical properties of three porous Si<sub>3</sub>N<sub>4</sub> ceramics fabricated by different techniques". Journal of Materials Science and Engineering, A 549, pp. 43-49

[Zeng et al. 2012] Zeng, W., Guo, Y., Jiang, K., Yu, Z., Liu, Y., Shen, Y., Deng, J., Wang, P., 2012, "Laser intensity effect on mechanical properties of wood-plastic composite parts fabricated by selective laser sintering". *Journal of Thermoplastic Composite Materials*. Vol. 26, pp. 125-136. DOI: 10.1177/0892705712461529

[Baechler et al. 2013] Baechler, C., DeVuono, M., Pearce, J.M., 2013, "Distributed recycling of waste polymer into RepRap feedstock", *Rapid Prototyping Journal*, Vol. 19 Iss 2 pp. 118 – 125

[Ivanova et al. 2013] Ivanova, O., Williams, C., Campbell, T., 2013, "Additive manufacturing (AM) and nanotechnology: promises and challenges", *Rapid Prototyping Journal*, Vol. 19 Iss 5 pp. 353 – 364

[Polzin et al. 2013] Polzin, C., Spath, S., Seitz, H., 2013, "Characterization and evaluation of a PMMA-based 3D printing process", *Rapid Prototyping Journal*, Vol. 19 Iss 1 pp. 37 – 43

[Zhu et al. 2014] Zhu, Y., Li, J., Tian, X., Wang, H., Liu, D., 2014, "Microstructure and mechanical properties of hybrid fabricated Ti-6.5Al-3.5Mo-1.5Zr-0.3Si titanium alloy by laser additive manufacturing". *Journal of Materials Science and Engineering*. Vol. 607, pp. 427-434

[Olivier et al. 2014] Olivier, D., Borros, S., Reyes, G., 2014, "Application-driven methodology for new additive manufacturing materials development", *Rapid Prototyping Journal*, Vol. 20 Iss 1 pp. 50 – 58

[Patricio et al. 2014] Patrício, T., Domingos, M., Gloria, A., D'Amora, U., Coelho, J.F., Bártolo, P.J., 2014, "Fabrication and characterisation of PCL and PCL/PLA scaffolds for tissue engineering", *Rapid Prototyping Journal*, Vol. 20 Iss 2 pp. 145 – 156

[Pires et al. 2014] Pires, I., Gouveia, B., Rodrigues, J., Fonte, R., 2014, "Characterization of sintered hydroxyapatite samples produced by 3D printing", *Rapid Prototyping Journal*, Vol. 20 Iss 5 pp. 413 – 421

[Tymrak et al. 2014] Tymrak, B.M., Kreiger, M., Pearce, J.M., 2014, "Mechanical properties of components fabricated with open-source 3-D printers under realistic environmental conditions". *Journal of Materials and Design*. Vol. 58, pp. 242-246

[Wheeler et al. 1999] Wheeler, B. C., Corey, J. M., Brewer, G. J., Branch, D. W., 1999, "Microcontact Printing for Precise Control of Nerve Cell Growth in Culture", *ASME Journal of Biomechanical Engineering*, Vol. 121 pp. 73 – 76

[Yan et al. 2003] Yan, Y., Wu, R., Zhang, R., Xiong, Z., Lin, F., 2003, "Biomaterial forming research using RP technology", *Rapid Prototyping Journal*, Vol. 9 Iss 3 pp. 142 – 149

[Roth et al. 2004] Roth, E.A., Xu, T., Das, M., Gregory, C., Hickman, J.J., Boland, T., 2004, "Inkjet Printing for High-throughput Cell Patterning", *Elsevier Biomaterials Journal*, Vol. 25, pp. 3707-3715

[Fang et al. 2005] Fang, Z., Starly, B., Sun, W., 2005, "Computer-aided characterization for effective mechanical properties of porous tissue scaffolds", Elsevier Computer-Aided Design Journal, Vol. 37, pp. 65-72

[Boland et al. 2007] Boland, T., Cui, X., Chaubey, A., Burg, T.C., Groff, R.E., Burg, K.J.L., 2007, "Precision Printing of Cells and Biomaterials onto 3D Matrices", Proceedings of the 2007 International Manufacturing Science And Engineering Conference, MSEC2007, October 15-17, 2007, Atlanta, Georgia, USA

[Yasar et al. 2008] Yasar, O., Dinh, M., Lan, S., Starly, B., 2008, "Fabrication of Micropatterned Hydrogels using Maskless Photopolymerization for Tissue Engineering Applications", Proceedings of the ASME 2008 Summer Bioengineering Conference (SBC2008), June 25-29, Marriott Resort, Marco Island, Florida, USA

[Xu et al. 2009] Xu, F., Moon, S., Emre, A.E., Lien, C., Turali, E.S., Demirci, U., 2009, "Cell Bioprinting as a Potential High-Throughput Method for Fabricating Cell-Based Biosensors (CBBs)", IEEE Sensors 2009 Conference

[Pepper et al. 2010] Pepper, M.E., Cass, C.A.P., Mattimore, J.P., Burg, T., Booth, B.W., Burg, K.J.L., Groff, R.E., 2010, "Post-Bioprinting Processing Methods to Improve Cell Viability and Pattern Fidelity in Heterogeneous Tissue Test Systems", 32nd Annual International Conference of the IEEE EMBS, Buenos Aires, Argentina, August 31 - September 4, 2010

[Savalani et al. 2012] Savalani, M.M., Hao, L., Dickens, P.M., Zhang, Y., Tanner, K.E., Harris, R.A., 2012, "The effects and interactions of fabrication parameters on the properties of selective laser sintered hydroxyapatite polyamide composite biomaterials", Rapid Prototyping Journal, Vol. 18 Iss 1 pp. 16 – 27

[Wang et al. 2013] Wang, Y., Qinghua, W., Pan, F., Mingming, Y., Shengmin, W., 2013, "Molecular dynamics simulations for the examination of mechanical properties of hydroxyapatite/poly a-n-butyl cyanoacrylate under additive manufacturing". Journal of Bio-Medical Materials and Engineering. Vol. 23, S857-S865

[Ozbolat and Yu 2013] Ozbolat, I.T., Yu, Y., 2013, "Bioprinting Toward Organ Fabrication: Challenges and Future Trends", IEEE Transactions on Biomedical Engineering, Vol. 60, No. 3, March 2013

[Zhang et al. 2013] Zhang, Y., Yu, Y., Chen, H., Ozbolat, I.T., 2013, "Characterization of Printable Cellular Micro-fluidic Channels for Tissue Engineering", Biofabrication Journal, Vol. 5, Iss. 025004, pp. 1-11

[Zhang et al. 2013] Zhang, Y., Yu, Y., Ozbolat, I.T., 2013, "Direct Bioprinting of Vessel-Like Tubular Microfluidic Channels", ASME Journal of Nanotechnology in Engineering and Medicine, Vol. 4, Iss 020902 pp. 1 - 7

[Lei et al. 2014] Lei, S., Frank, M.C., Anderson, D.D., Brown, T.D., 2014, "A method to represent heterogeneous materials for rapid prototyping: the Matryoshka approach", *Rapid Prototyping Journal*, Vol. 20 Iss 5 pp. 390 – 402

[Patricio et al. 2014] Patrício, T., Domingos, M., Gloria, A., D'Amora, U., Coelho, J.F., Bártolo, P.J., 2014, "Fabrication and characterisation of PCL and PCL/PLA scaffolds for tissue engineering", *Rapid Prototyping Journal*, Vol. 20 Iss 2 pp. 145 – 156

[Otsubo et al. 1984] Otsubo, Y., Amari, T., Watanabe, K., 1984, "Rheological Behavior of Epoxy Acrylate prepolymer during UV Curing", Department of Image Science and Technology, Faculty of Engineering, Chiba University, 1-33, Yayoi-cho, Chiba-shi, 260 Japan.

[Otsubo et al. 1986] Otsubo, Y., Amari, T., Watanabe, K., 1986, "Rheological Studies of Ultraviolet Curing with an Oscillating Plate Rheometer", Department of Image Science and Technology, Faculty of Engineering, Chiba University, 1-33, Yayoi-cho, Chiba-shi, 260 Japan.

[Cunningham 1996] Cunningham, W., 1996, "UV curing of acrylate resins versus cationic epoxies", *Adhesives Age*, Dymax Corp., Torrington, Connecticut.

[Decker 1997] Decker, C., 1997, "Special Review: The Use of UV Irradiation in Polymerization", *Polymer International Journal*, Vol. 45, 133-141, Laboratoire de Photochimie Generale, Ecole Nationale Supérieure de Chimie de Mulhouse, Université de Haute Alsace, France.

[Crivello 1999] Crivello, J. V., 1999, "UV and electron beam-induced cationic polymerization", *Journal of Nuclear Instruments and Methods in Physics Research*, Department of Chemistry, Rensselaer Polytechnic Institute, Troy, NY 12180 USA.

[Lee et al. 2001] Lee, J.H., Prud'homme, R.K., Aksay, I.A., 2001, "Cure depth in photopolymerization: Experiments and theory", *J. Mater. Res.*, Vol. 16, No. 12, December, Department of Chemical Engineering and Princeton Materials Institute, Princeton University, Princeton, New Jersey.

[Stowe 2001] Stowe, R.W., 2001, "UV Curing", *Products Finishing*, 65(10), 5-4s, Retrieved from <http://search.proquest.com.uproxy.library.dc-uoit.ca/docview/214193513?accountid=14694>.

[Umezaki and Abe 2007] Umezaki, E., Abe, M., 2007, "Effect of UV Illumination Wavelengths on Stress and Temperature in Curing Process of UV Curing Resin", *Journal of Photoelasticity and its Applications*, Nippon Institute of Technology, Saitama, Japan.

[Lin et al. 2014] Lin, J.-T., Liu, H.-W., Cheng, D.-C., 2014, "Modeling the Kinetics of Enhanced Photo-Polymerization under a Collimated and a Reflecting Focused UV Laser", *Journal of Polymers* 2014, 6, 1489-1501, DOI: 10.3390/polym6051489.

[Nam et al. 2014] Nam, K., Shimatsu, Y., Matsushima, R., Kimura, T., Kishida, A., 2014, "In-situ polymerization of PMMA inside decellularized dermis using UV photopolymerization", *European*

Polymer Journal 60, 163-171, Elsevier Ltd., DOI:  
<http://dx.doi.org/10.1016/j.eurpolymj.2014.09.006>.

[Ebrahimi and Bastani 2014] Ebrahimi, M., Bastani, S., 2014, "UV curable urethane acrylate coatings formulation: experimental design approach", Journal of Pigment and Resin Technology, Emerald Group Publishing Limited, DOI: 10.1108/PRT-10-2012-0072.

[Maurya and Amin 2014] Maurya, R.S., Amin, S.A., 2014, "To study the effects on modified urea formaldehyde resins", International Journal of Futuristic Trends in Engineering and Technology, Vol. 4 (01), Akshar Publication.

[Sokol 2010] Sokol, A. A., 2010, "application methods: Ultraviolet (UV) Cured Coatings", UV Coatings Ltd., Cleveland, USA. pp 196-204.

[Bajpai et al. 2002] Bajpai, M., Shukla, V., Kumar, A., 2002, "Film Performance and UV Curing of Epoxy Acrylate Resins", Journal of Progress in Organic Coatings, Vol. 44, 271-278, Elsevier Science.

[Decker and Bianchi 2005] Decker, C., Bianchi, C., 2005, "Ultrafast hardening of a modelling paste by UV-curing of a polyamide filled acrylic resin", Journal of Materials Science 40, 5491-5497, Ecole Nationale Supérieure de Chimie de Mulhouse, Université de Haute-Alsace, France.

[Satake et al. 2010] Satake, S.-I., Sorimachi, G., Kanai, T., Taniguchi, J., Unno, N., 2010, "Three-Dimensional Measurements of Photo-curing Process With Photo-curable Resin for UV-Nanoimprint by Micro-digital-Holographic-PTV", Journal of Electronic Packaging, Vol. 132, 031003-1, IEEE.

[Decker 2001] Decker, C., 2001, "UV-radiation curing chemistry", Journal of Pigment & Resin Technology, Vol. 30 Iss 5 pp. 278-286, DOI: <http://dx.doi.org/10.1108/03699420110404593>.

[Tufts 1980] Tufts, T.A., 1980, "Photoinitiated Cationic Polymerization", Ph.D. dissertation, University Microfilms International, Ann Arbor, MI.

[Joshi and Rodriguez 1984] Joshi, M.G., Rodriguez, F., 1984, "Photoinitiated Polymerization of 1-Vinylimidazole", Journal of Applied Polymer Science, Vol. 29, 1345-1354, John Wiley & Sons, Inc.

[Hult et al. 1985] Hult, A., MacDonald, S.A., Wilson, C.G., 1985, "Photoinitiated Interfacial Cationic Polymerization", Journal of Macromolecules, Vol. 18, No. 10, American Chemical Society.

[Davidenko et al. 1998] Davidenko, N., Peniche, C., Sastre, R., Roman, J.S., 1998, "Photoinitiated copolymerization of furfuryl methacrylate and N,N-dimethyl acrylamide", Polymer Journal, Vol. 39, No. 4, pp. 917-921, Elsevier Science Ltd.

[Burdick et al. 2001] Burdick, J.A., Peterson, A.J., Anseth, K.S., 2001, "Conversion and temperature profiles during the photoinitiated polymerization of thick orthopaedic biomaterials", *Journal of Biomaterials* 22, 1779-1786, Elsevier Science Ltd.

[Fisher et al. 2001] Fisher, J.P., Dean, D., Engel, P.S., Mikos, A.G., 2001, "Photoinitiated Polymerization of Biomaterials", *Annu. Rev. Mater. Res.* 31: 171-181, Annual Reviews, ProQuest Science Journals.

[Anseth and Burdick 2002] Anseth, K.S., Burdick, J.A., 2002, "New Directions in Photopolymerizable Biomaterials", *Materials Research Society, MRS Bulletin*, Department of Chemical Engineering, University of Colorado at Boulder, Colorado.

[Fisher 2002] Fisher, J.P., 2002, "The Development of a Photocrosslinked Biomaterial for Bone Tissue Engineering Applications", Ph.D. dissertation, Rice University, Houston, Texas.

[Halvorson et al. 2002] Halvorson, R.H., Erickson, R.L., Davidson, C.L., 2002, "Energy dependent polymerization of resin-based composite", *Journal of Dental Materials* 18, 463-469, Elsevier Science Ltd.

[Burdick et al. 2003] Burdick, J.A., Lovestead, T.M., Anseth, K.S., 2003, "Kinetic Chain Lengths in Highly Cross-Linked Networks Formed by the Photoinitiated Polymerization of Divinyl Monomers: A Gel Permeation Chromatography Investigation", *Journal of Biomacromolecules* Vol 4, pp. 149-156, American Chemical Society.

[Choe 2003] Choe, Y., 2003, "Estimating Diffusion-Controlled Reaction Parameters in Photoinitiated Polymerization of Dimethacrylate Macromonomers", *Journal of Macromolecular Research*, Vol. 11, No. 5, pp. 311-316, Polymer Society of Korea.

[Davis et al. 2003] Davis, K.A., Burdick, J.A., Anseth, K.S., 2003, "Photoinitiated crosslinked degradable copolymer networks for tissue engineering applications", *Journal of Biomaterials* 24, pp. 2485-2495, Elsevier Science Ltd, Science Direct.

[Fairbanks 2004] Fairbanks, B.D., 2004, "Photochemical reactions for functional biomaterials development: Thiol-ene and Thiol-yne photopolymerizations", Ph.D. dissertation, Department of Chemical and Biological Engineering, University of Colorado, Boulder, Colorado.

[Joshi 2004] Joshi, A.L., 2004, "Synthesis of New Photocurable Polymers as Biomaterials for Artificial Bones", Ph.D. dissertation, University of Florida, Gainesville, Florida.

[Franca et al. 2005] Franca, F.M.G., Hori, F.S., Santos, A.J.dS., Lovadino, J.R., 2005, "The effect of insertion and photopolymerization techniques on microleakage of Class V cavities – a quantitative evaluation", *Braz Oral Res*, Vol. 19, Iss. 1, pp. 30-35.

[Murphy et al. 2005] Murphy, M.R., Faucher, K.M., Sun, X.-L., Chaikof, E.L., Dluhy, R.A., 2005, "Analysis of photoinitiated polymerization in a membrane mimetic film using spectroscopy and

near-IR Raman microscopy”, *Journal of Colloids and Surfaces: Biointerfaces*, Vol. 46, pp. 226-232, Elsevier Science Ltd, Science Direct.

[Rydholm et al. 2005] Rydholm, A.E., Bowman, C.N., Anseth, K.S., 2005, “Degradable thiol-acrylate photopolymers: polymerization and degradation behavior of an in situ forming biomaterial”, *Journal of Biomaterials*, Vol 26, pp. 4495-4506, Elsevier Science Ltd, Science Direct.

[Jakubiak et al. 2006] Jakubiak, J., Wrzyszczyński, A., Linden, L.A, Rabek, J.F., 2006, “The Role of Amines in the Camphorquinone Photoinitiated Polymerization of Multifunctional Monomer”, *Journal of Macromolecular Science, Part A: Pure and Applied Chemistry*, Vol. 44, pp. 239-242, Taylor & Francis Group, LLC, DOI: 10.1080/10601320601031440.

[Salinas 2007] Salinas, C.N., 2007, “Photoinitiated Thiol-Acrylate Polymerizations to Tailor PEG Microenvironments with Peptide Moieties to Direct Chondrogenic Differentiation of hMSCs”, Ph.D. dissertation, Department of Chemical and Biological Engineering, University of Colorado, Boulder, Colorado.

[Abu-Abdoun 2008] Abu-Abdoun, I.I., 2008, “Photoinitiated Cationic Polymerization of p-methylstyrene by Methoxy Trityl Salts”, *International Journal of Polymeric Materials*, Vol. 57, pp. 584-593, Taylor & Francis Group, LLC, DOI: 10.1080/00914030701818322.

[Fairbanks et al. 2009] Fairbanks, B.D., Schwartz, M.P., Bowman, C.N., Anseth, K.S., 2009, “Photoinitiated polymerization of PEG-diacrylate with lithium phenyl-2,4,6-trimethylbenzoylphosphinate: polymerization rate and cytocompatibility”, *Journal of Biomaterials*, Vol. 30, pp. 6702-6707, Elsevier Science Ltd.

[Wen et al. 2009] Wen, Y., Jiang, X., Liu, R., Yin, J., 2009, “Amphipathic hyperbranched polymeric thioxanthone photoinitiators (AHPTXs): Synthesis, characterization and photoinitiated polymerization”, *Polymer Journal*, Vol. 50, pp. 3917-3923, Elsevier Science Ltd.

[Albano et al. 2010] Albano, C., Gonzalez, G., Parra, C., 2010, “Sonochemical synthesis of polymethylmethacrylate to be used as biomaterial”, *Polymer Bulletin*, Vol. 65, pp. 893-903, Springer-Verlag, DOI: 10.1007/s00289-010-0300-3.

[Bianchi et al. 2010] Bianchi, E.C., Ulhoa, M.P.dM., Aguiar, P.R., Freitas, C.A.d, Goncalves, G.dM.B., 2010, “Analysis of Polymerization Time on Abrasive Wear of Dental Resins”, *Journal of Materials Research*, Vol. 13, pp. 41-44.

[Yagci et al. 2010] Yagci, Y., Jockusch, S., Turro, N.J., 2010, “Photoinitiated Polymerization: Advances, Challenges, and Opportunities”, *Journal of Macromolecules*, Vol. 43, pp. 6245-6260, DOI: 10.1021/mal1007545.

[Moraes et al. 2011] Moraes, C., Zhao, R., Likhitpanichkul, M., Simmons, C.A., Sun, Y., 2011, “Semi-confined compression of microfabricated polymerized biomaterial constructs”, *Journal of Macromechanics and Microengineering*, Vol. 21, 10pp, IOP Publishing.

[Melander et al. 2012] Melander, J.R., Weiler, R.A., Miller, B.D., Schuman, T.P., Kilway, K.V., Day, D.E., Velez, M., Eick, J.D., 2012, “Estimation of properties of a photoinitiated silorane-based composite with potential for orthopaedic applications”, *Journal of Biomedical Materials Research B: Applied Biomaterials*, Vol. 100B, Iss. 1, Society of Biomaterials, DOI: 10.1002/jbm.b.31934.

[Gu et al. 2013] Gu, X., Sun, H., Kong, X., Fu, C., Yu, H., Li, J., Wang, J., 2013, “A green protocol to prepare monodisperse poly (TMPTMA-styrene) microspheres by photoinitiated precipitation polymerization in low-toxicity solvent”, *Journal of Colloid Polymer Science*, Vol. 291, pp. 1771-1779, DOI: 10.1007/s00396-013-2912-2.

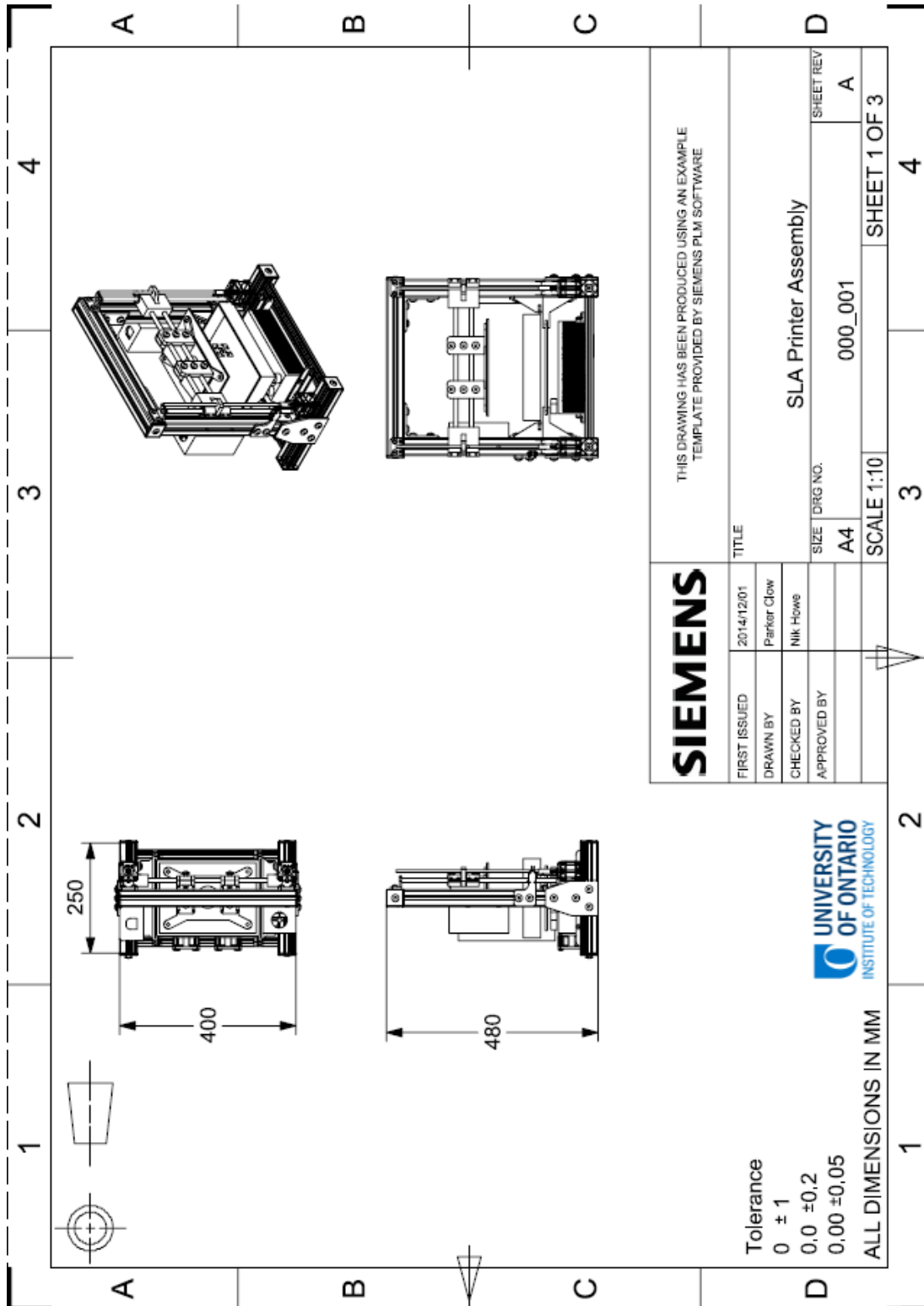
[Degirmenci and Genli 2014] Degirmenci, M., Genli, N., 2014, “Synthesis and characterization of epoxy-chain end(s) functional macromonomer of polystyrene and its use in photoinitiated cationic polymerization”, *Iran Polymer Journal*, Vol. 23, pp. 457-468, DOI: 10.1007/s13726-014-0240-0.

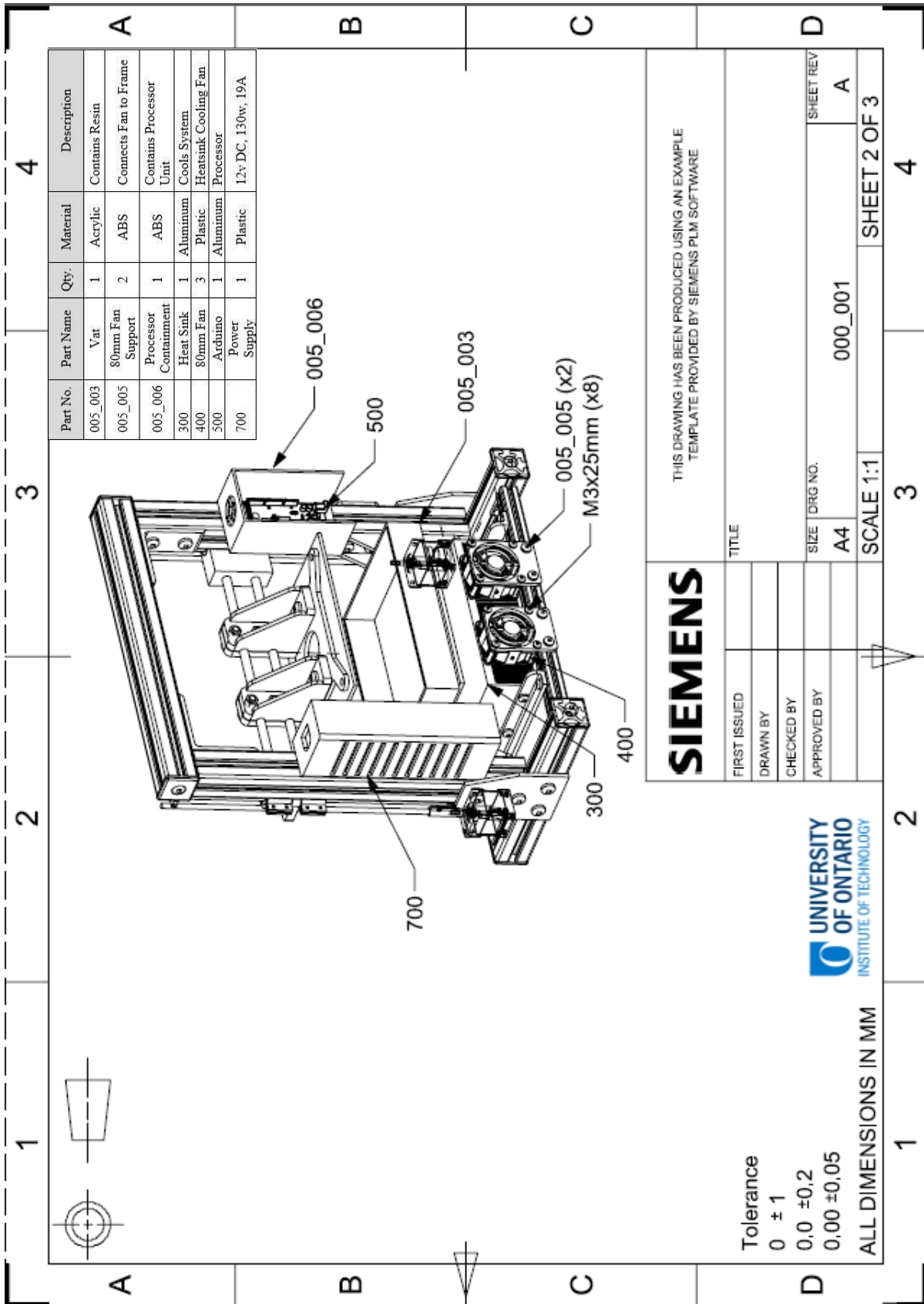
[Lin et al. 2014] Lin, J.-T., Chin, C.-C., Huang, D.-W., Liu, H.-W., 2014, “Modeling of uniform polymerization via combined mechanism of photoinitiation and photothermal initiation”, *Journal of Polymer Research*, Vol. 21, pp. 461-466, Springer Science + Business Media Dordrecht.

[Lin and Cheng 2014] Lin, J.-T., Cheng, D.-C., 2014, “Optimal Focusing and Scaling Law for Uniform Photo-Polymerization in a Thick Medium Using a Focused UV Laser”, *Journal of Polymers*, Vol. 6, pp. 552-564, DOI: 10.3390/polym6020552

# Appendices

## Appendix A: Preliminary Machine Engineering Assembly Drawings





# Appendix B: MakerJuice G+ Resin Technical Data Sheet



## Substance G+

DATASHEET

High Performance, General Purpose UV Cure Resin

**Descriptors:**

Hard, tough, fast cure speed.

**Colors Available:**

Red, Orange, Yellow, Green, Cyan, Indigo, Purple, Black

**Sizes Available:**

300mL (0.55 KG), 1 Liter (1.1 KG)

Larger sizes available upon request, for special order.

**Technical Data:**

Experimental Shrink: 3.3%

Ash Content: < 0.2%

Surface Tension: 36.3 Dynes/cm

Tensile Strength: 9100 PSI, 6% Elongation

Shore Hardness: 73 D

Glass Transition Temperature: 104°C

Uncolored Reactivity: 423 ml/cm<sup>3</sup>

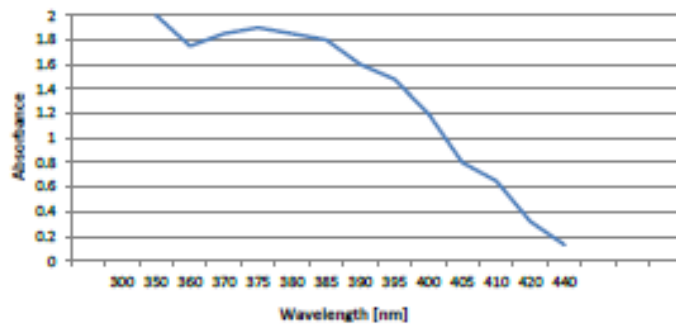
Water content: < 0.23%

Viscosity @ 20°C: 90 cP

Acidity: < 0.31 mg KOH/g

Density @ 25°C: 1.1 g/cm<sup>3</sup>

UV Absorption:



**Storage:**

Store in a tightly closed, opaque container in a properly vented storage area under dry conditions away from heat, sparks, and open flames. Shelf-life is 6 months from receipt.

**Safety:**

For additional information please see the Material Safety Data Sheet.

## Appendix C: Code

### Main File 1: “STL\_read\_slice\_Main.m”

```
FV = stread('Rook.stl');
faces = FV.faces;
vertices = FV.vertices;
sheight = 0.1; ind = 1; all = {};
vertheight=[];

for i = 1:length(faces)
    vertheight = [vertheight; max(vertices(faces(i,:)'),3)) min(vertices(faces(i,:)'),3)];
end
for z = min(vertheight(:)):sheight:max(vertheight(:))
    intersect = find((vertheight(:,1) >= z & vertheight(:,2) < z) | (vertheight(:,1) > z &
vertheight(:,2) <= z));
    finalpoints = [];
    for i = 1:length(intersect)
        fill3(vertices(faces(intersect(i,:)'),1), vertices(faces(intersect(i,:)'),2),
vertices(faces(intersect(i,:)'),3), 0.5);
        points = vertices(faces(intersect(i,:)'),:);
        above = find(points(:,3) > z);
        below = find(points(:,3) < z);
        equal = find(points(:,3) == z);
        q = max(vertheight);
        newpoints = [];
        if length(equal) > 1 && (length(above) == 1 || z == q(1) || z == q(2))
            newpoints = points(equal,:);
        elseif length(equal) == 1 && length(above) == 1 && length(below) == 1
            newpoints = points(equal,:);
            t = (z-points(below,3))/(points(above,3)-points(below,3));
            newpoints(2,:) = points(below,:)+abs(t)*(points(above,:)-points(below,:));
        elseif length(above) == 1
            for j = 1:length(below)
                t = (z-points(below(j),3))/(points(above,3)-points(below(j),3));
                newpoints(j,:) = points(below(j,:)+abs(t)*(points(above,:)-points(below(j),:)));
            end
        elseif length(below) == 1
            for j = 1:length(above)
                t = (z-points(below,3))/(points(above(j),3)-points(below,3));
                newpoints(j,:) = points(below,:)+abs(t)*(points(above(j),:)-points(below,:));
            end
        end
    end
    if ~isempty(newpoints)
```

```

        finalpoints = [finalpoints; newpoints(1,1:2) newpoints(2,1:2)];
    end
end
fincheck = sort(finalpoints,2);
[C,ia,ic] = unique(fincheck,'rows','stable');
finalpoints = finalpoints(ia,:);
loops = {}; k = 1;
while length(finalpoints) > 1
    loop = [finalpoints(1,[1 2]); finalpoints(1,[3 4])];
    finalpoints(1,:) = [];
    while (loop(end, 1) ~= loop(1,1)) || (loop(end, 2) ~= loop(1,2))
        loc = find((finalpoints(:,1) == loop(end,1) & finalpoints(:,2) == loop(end,2)) |
(finalpoints(:,3) == loop(end,1) & finalpoints(:,4) == loop(end,2)));
        if isempty(finalpoints) || isempty(loc)
            break
        elseif loop(end,:) == finalpoints(loc(1),[1 2])
            loop(end+1,:) = finalpoints(loc(1),[3 4]);
        else
            loop(end+1,:) = finalpoints(loc(1),[1 2]);
        end
        finalpoints(loc,:) = [];
    end
    loops{k} = loop;
    k = k + 1;
end
contour{ind} = loops;
ind = ind+1;
end

```

## Main File 2: “SLA\_video\_Main.m”

```

vidObj = VideoWriter('SLAvideo.avi');
vidObj.FrameRate = 0.168; % number of images displayed per second
open(vidObj)

for q = 1:length(contour)
    c = []; k = 0;
    for i = 1:length(contour{1,q})
        for j = 1:length(contour{1,q})
            [IN, ON] =
inpolygon(contour{1,q}{1,i}(:,1),contour{1,q}{1,i}(:,2),contour{1,q}{1,j}(:,1),contour{1,q}{1,j}(:,2));
            if max(IN)+max(ON) == 1

```

```

        k = k+1;
    end
end
c(i,:) = [i k];
k = 0;
end
h = figure('Color','black'); hold on; axis([-138 -62 -40 38]);
%axis equal;
axis off; set(gca,'color','black'); set(gcf,'color','black');
c = sortrows(c,2);
for i = 1:size(c,1)
    if mod(c(i,2),2)~=0
        fill(contour{1,q}{1,c(i,1)}(:,1),contour{1,q}{1,c(i,1)}(:,2),'k')
    else
        fill(contour{1,q}{1,c(i,1)}(:,1),contour{1,q}{1,c(i,1)}(:,2),'w')
    end
end
end

set(gca,'xtick',[])
set(gca,'ytick',[])
getx = get(gca,'xlim');
gety = get(gca,'ylim');
colormap(gray);
frame=getframe;
writeVideo(vidObj, frame);
close figure 1;
end
close(vidObj);

```